

The CARMENES search for exoplanets around M dwarfs

High-resolution optical and near-infrared spectroscopy of 324 survey stars

A. Reiners¹, M. Zechmeister¹, J.A. Caballero^{2,3}, I. Ribas⁴, J.C. Morales⁴, S.V. Jeffers¹, P. Schöfer¹, L. Tal-Or¹, A. Quirrenbach³, P.J. Amado⁵, A. Kaminski³, W. Seifert³, M. Abril⁵, J. Aceituno⁶, F.J. Alonso-Floriano^{8,12}, M. Ammler-von Eiff^{11,13}, R. Antona⁵, G. Anglada-Escudé^{5,14}, H. Anwand-Heerwart¹, B. Arroyo-Torres⁶, M. Azzaro⁶, D. Baroch⁴, D. Barrado², F.F. Bauer¹, S. Becerril⁵, V.J.S. Béjar⁹, D. Benítez⁶, Z.M. Berdiñas⁵, G. Bergond⁶, M. Blümcke¹¹, M. Brinkmöller³, C. del Burgo¹⁵, J. Cano⁸, M.C. Cárdenas Vázquez^{6,7}, E. Casal⁵, C. Cifuentes⁸, A. Claret⁵, J. Colomé⁴, M. Cortés-Contreras^{8,2}, S. Czesla¹⁰, E. Díez-Alonso⁸, S. Dreizler¹, C. Feiz³, M. Fernández⁵, I.M. Ferro⁵, B. Fuhrmeister¹⁰, D. Galadí-Enríquez⁶, A. García-Piquer⁴, M.L. García Vargas¹⁶, L. Gesa⁴, V. Gómez Galera⁶, J.I. González Hernández⁹, R. González-Peinado⁸, U. Grözinger⁷, S. Grohnert³, J. Guàrdia⁴, E.W. Guenther¹¹, A. Guijarro⁶, E. de Guindos⁶, J. Gutiérrez-Soto⁵, H.-J. Hagen¹⁰, A.P. Hatzes¹¹, P.H. Hauschildt¹⁰, R.P. Hedrosa⁶, J. Helmling⁶, Th. Henning⁷, I. Hermelo⁶, R. Hernández Arabí⁶, L. Hernández Castaño⁶, F. Hernández Hernando⁶, E. Herrero⁴, A. Huber⁷, P. Huke¹, E. Johnson¹, E. de Juan⁶, M. Kim^{5,17}, R. Klein⁷, J. Klüter³, A. Klutsch^{8,18}, M. Kürster⁷, M. Lafarga⁴, A. Lamert¹, M. Lampón⁵, L.M. Lara⁵, W. Laun⁷, U. Lemke¹, R. Lenzen⁷, R. Launhardt⁷, M. López del Fresno², J. López-González⁵, M. López-Puertas⁵, J.F. López Salas⁶, J. López-Santiago^{8,27}, R. Luque³, H. Magán Madinabeitia^{6,11}, U. Mall⁷, L. Mancini^{7,19,29}, H. Mandel³, E. Marfil⁸, J.A. Marín Molina⁶, D. Maroto Fernández⁶, E.L. Martín², S. Martín-Ruiz⁵, C.J. Marvin¹, R.J. Mathar⁷, E. Mirabet⁵, D. Montes⁸, M.E. Moreno-Raya⁶, A. Moya^{2,5}, R. Mundt⁷, E. Nagel¹⁰, V. Naranjo⁷, L. Nortmann⁹, G. Nowak⁹, A. Ofir²⁰, R. Oreiro⁵, E. Pallé⁹, J. Panduro⁷, J. Pascual⁵, V.M. Passegger¹, A. Pavlov⁷, S. Pedraz⁶, A. Pérez-Calpena¹⁶, D. Pérez Medialdea⁵, M. Perger⁴, M.A.C. Perryman²¹, M. Pluto¹¹, O. Rabaza^{5,24}, A. Ramón⁵, R. Rebolo⁹, P. Redondo⁹, S. Reffert³, S. Reinhart⁶, P. Rhode¹, H.-W. Rix⁷, F. Rodler^{7,22}, E. Rodríguez⁵, C. Rodríguez-López⁵, A. Rodríguez Trinidad⁵, R.-R. Rohloff⁷, A. Rosich⁴, S. Sadegi³, E. Sánchez-Blanco⁵, M.A. Sánchez Carrasco⁵, A. Sánchez-López⁵, J. Sanz-Forcada², P. Sarkis⁷, L.F. Sarmiento¹, S. Schäfer¹, J.H.M.M. Schmitt¹⁰, J. Schiller¹¹, A. Schweitzer¹⁰, E. Solano², O. Stahl³, J.B.P. Strachan¹⁴, J. Stürmer^{3,23}, J.C. Suárez^{5,24}, H.M. Tabernero^{8,28}, M. Tala³, T. Trifonov⁷, S.M. Tulloch^{25,26}, R.G. Ulbrich¹, G. Veredas³, J.I. Vico Linares⁶, F. Vilardell⁴, K. Wagner^{3,7}, J. Winkler¹¹, V. Wolthoff³, W. Xu³, F. Yan⁷, and M.R. Zapatero Osorio²

(Affiliations can be found after the references)

February 12, 2018

ABSTRACT

The CARMENES radial velocity (RV) survey is observing 324 M dwarfs to search for any orbiting planets. In this paper, we present the survey sample by publishing one CARMENES spectrum for each M dwarf. These spectra cover the wavelength range 520–1710 nm at a resolution of at least $R > 80,000$, and we measure its RV, H α emission, and projected rotation velocity. We present an atlas of high-resolution M-dwarf spectra and compare the spectra to atmospheric models. To quantify the RV precision that can be achieved in low-mass stars over the CARMENES wavelength range, we analyze our empirical information on the RV precision from more than 6500 observations. We compare our high-resolution M-dwarf spectra to atmospheric models where we determine the spectroscopic RV information content, Q , and signal-to-noise ratio. We find that for all M-type dwarfs, the highest RV precision can be reached in the wavelength range 700–900 nm. Observations at longer wavelengths are equally precise only at the very latest spectral types (M8 and M9). We demonstrate that in this spectroscopic range, the large amount of absorption features compensates for the intrinsic faintness of an M7 star. To reach an RV precision of 1 m s^{-1} in very low mass M dwarfs at longer wavelengths likely requires the use of a 10 m class telescope. For spectral types M6 and earlier, the combination of a red visual and a near-infrared spectrograph is ideal to search for low-mass planets and to distinguish between planets and stellar variability. At a 4 m class telescope, an instrument like CARMENES has the potential to push the RV precision well below the typical jitter level of $3\text{--}4 \text{ m s}^{-1}$.

Key words. Astronomical data bases – Stars: rotation – Stars: late-type – Stars: low-mass – Infrared: stars

1. Introduction

Spectroscopy of M dwarfs has become a very active research field because potentially habitable planetary companions cause Doppler variations that are more easily detectable around stars

of lower mass (Martín et al. 2005; Scalo et al. 2007; Tarter et al. 2007). These stars also constitute the vast majority of potential planet hosts in our immediate vicinity, and a detailed characterization of their planets is believed to be easier than in the

more massive, brighter, and more distant Sun-like stars (see, e.g., Anglada-Escudé et al. 2016).

The first radial velocity (RV) surveys for extrasolar planets focused on objects in orbit around Sun-like stars (see, e.g., Udry & Santos 2007). The lower end of the mass range of the discovered planets was continuously extended until measurement precision reached a level of about 1 m s^{-1} (Mayor et al. 2009b; Fischer et al. 2016). At this precision, a $10 M_{\oplus}$ planet can be discovered on a 1 yr orbit in the liquid-water habitable zone around a $1 M_{\odot}$ star. The shortcut to potentially habitable planets similar to Earth is to look around lighter stars; at the same RV precision, a $2 M_{\oplus}$ planet can be found in the habitable zone around a $0.3 M_{\odot}$ star (see, e.g., Rivera et al. 2005; Mayor et al. 2009a; Bonfils et al. 2013; Anglada-Escudé et al. 2013, 2014, 2016).

The CARMENES M-dwarf survey began operations on Jan 1, 2016. The instrument is located at Calar Alto observatory in Almeria, Southern Spain ($37^{\circ}13'25''\text{N}, 2^{\circ}32'46''\text{W}$). It provides nearly continuous wavelength coverage from 520 to 1710 nm from its two channels: the visual channel (VIS) with a spectral resolution of $R = 94,600$ covers the range $\lambda = 520\text{--}960 \text{ nm}$, and the near-infrared channel (NIR) operates at $R = 80,400$ and $\lambda = 960\text{--}1710 \text{ nm}$ (Quirrenbach et al. 2016). For the M-dwarf survey, we regularly observe about 300 M dwarfs across all M-spectral subtypes. A total amount of 750 useful nights is reserved as Guaranteed Time Observations (GTO) with the goal to collect approximately 70 spectra for each target over the course of the program (García-Piquer et al. 2017).

The main motivation for building an optical and near-infrared spectrograph with this large wavelength coverage is to measure RVs in very cool stars (e.g., Martín et al. 2006) and to understand the amount of RV information and stellar RV jitter as a function of wavelength. It is well known that Sun-like stars provide most RV information at blue optical wavelengths where astronomical spectrographs already reached the 10 m s^{-1} level in the 1980s (Campbell & Walker 1979; Merline 1985). However, cooler low-mass stars provide more flux at near-infrared wavelengths, while their spectrum is extremely rich in molecular features at optical wavelengths, which makes detailed predictions about measurable RV precisions difficult. There has not been a final answer so far to the question in which spectral range the RV method is most sensitive for low-mass stars (see Section 4).

Radial velocity jitter can be caused by corotating active regions, magnetic cycles, variations in stellar granulation, stellar oscillations, and other mechanisms (e.g., Lagrange et al. 2010; Meunier et al. 2010a,b; Cegla et al. 2014; Lanza et al. 2016). Its amplitude is expected to depend on wavelength (e.g., Desort et al. 2007; Reiners et al. 2010; Marchwinski et al. 2015). A spectrograph with large wavelength coverage can help to distinguish between Keplerian signals from an orbiting planet and RV variations caused by the star itself (e.g., Saar & Donahue 1997; Barnes et al. 2011, 2017; Jeffers et al. 2014; Korhonen et al. 2015). Furthermore, the pattern of RV variation as a function of wavelength can itself provide important information about the star, for example, about spot temperatures and Zeeman broadening (Reiners et al. 2013), or about a modal identification for pulsating stars (Amado et al. 2007; Amado 2007).

While stellar atmosphere models have improved significantly over the past decade and instruments are being designed for 10 cm s^{-1} precision (Pepe et al. 2010), there is a need for empirical calibration of the possible RV precision across optical and near-infrared wavelengths for M dwarfs. The growing amount of transiting-planet candidates discovered by photometry missions such as *Kepler*, MEarth, APACHE, and future missions like *TESS* and *PLATO*, requires a substantial infrastruc-

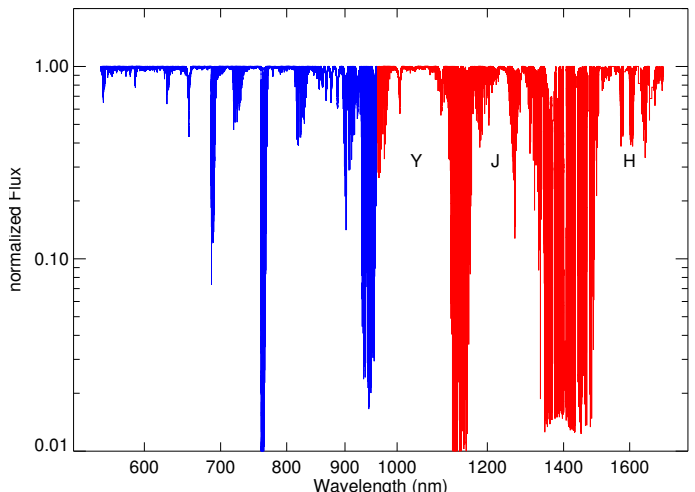


Fig. 1. Overview of the CARMENES spectral range. The spectrum covered by the VIS channel is shown in blue, and the NIR channel in red. The target shown is the A2V star 50 Cas. The stellar spectrum only exhibits a few hydrogen lines, all strong features are from Earth's atmosphere.

ture for spectroscopic follow-up. A host of red optical and near-infrared spectrographs are currently planned or under construction that will provide the required data to determine down the mass of our nearest transiting neighbors (e.g., Mahadevan et al. 2014; Artigau et al. 2014; Kotani et al. 2014; Seifahrt et al. 2016; Crepp et al. 2016; Claudi et al. 2016; Jurgenson et al. 2016; Gibson et al. 2016). For an efficient planning of RV follow-up in low-mass stars, and for new or extended RV surveys of our closest neighbors, empirical information on the RV performance across different wavelengths is important. With our data from the CARMENES program, we are in an excellent position to address this question.

In this paper, we introduce the CARMENES sample and provide detailed information about the 324 target stars that we are surveying for planets. After more than a year of observations, we have amassed several thousand spectra with both CARMENES channels, enough to draw statistically significant conclusions about the spectroscopic properties and RV precision across the entire CARMENES wavelength range. CARMENES is the first spectrograph that routinely delivers high-resolution spectra of low-mass stars at infrared wavelengths. Before CARMENES, spectroscopic information of low-mass stars could only be provided by a few instruments, most of them requiring multiple settings and/or access to 10 m class telescopes (e.g., Lebzelter et al. 2012). As a service to the community, with this paper we also publish one CARMENES spectrum for each survey star.

We introduce the CARMENES GTO sample stars and the library of CARMENES spectra in Section 2, and we derive spectroscopic information about rotation and radial velocities for each star. In Section 3 we take a detailed look into our atlas of high-resolution spectra for three example stars that represent different M subtypes. The atlas itself is published in the online version of the paper. We investigate the RV information content of M dwarfs from our observations in Section 4. Finally, our results are summarized in Section 5.

2. Library of M-type CARMENES spectra

The CARMENES spectral format covers the wavelength range 520–1710 nm. In the telescope front-end, a beam splitter sends light at wavelengths shorter than 960 nm into the VIS channel and longer wavelengths into the NIR channel. The two channels operate independently, but see light from the same object. Data are reduced with our automatic pipeline using the method of optimal extraction (Zechmeister et al. 2014). Reduced spectra are stored at the Calar Alto archive and analyzed for their RVs (Zechmeister et al. 2017); see also Caballero et al. (2016).

The NIR detector is an array of two detectors that are separated by a small gap. The spectral coverage is almost continuous, with additional small gaps that grow toward long wavelengths; gaps are between zero and 15 nm large from the very blue to the very red end. The spectral format cannot be changed. An overview of the CARMENES spectral range and telluric contamination is presented in Fig. 1. The normalized spectrum is shown logarithmically on both axes. It shows the telluric contamination of the spectrum and the three main atmospheric windows, that is, the z , J , and H bands, that are covered by the NIR channel.

As part of the GTO agreement, we provide early access to one CARMENES spectrum for each of our sample targets (Table B.1). They can be downloaded from the CARMENES GTO Data Archive (Caballero et al. 2016).¹ Each spectrum is a single exposure obtained between Jan 1, 2016, and Aug 31, 2017, and has a signal-to-noise ratio (S/N) typical for our survey (see below). Details on how the S/N is calculated are given in Zechmeister et al. (2017).

2.1. Sample

To define our sample of M dwarfs, we selected the brightest members of every spectral subtype that are visible from Calar Alto ($\delta > -23^\circ$) and that are not known to be members of multiple systems at separations closer than 5''. We carried out extensive preparatory observations and characterization to define our survey sample. For more details on target preselection and characterization, we refer to Alonso-Floriano et al. (2015), Cortés-Contreras et al. (2017), and Jeffers et al. (2017). In contrast to other M-dwarf planet surveys, we explicitly did not bias our sample with regard to age or chromospheric activity. One of the expected advantages of the long-wavelength coverage of CARMENES is that RV variations caused by stellar activity can to some extent be distinguished from orbital motion. Learning about the RV signature from starspots and stellar activity as a function of wavelength is one of the science goals of the CARMENES M-dwarf survey. We also did not exclude stars with planets that were already known. Our sample therefore has some overlap with other RV programs. Analyses of CARMENES RVs for seven stars with known planets were presented in Trifonov et al. (2017).

After a few observations were taken for each star, we discovered several double-lined spectroscopic binaries (SB2s) that will be presented in a separate paper. After cleaning for SB2s, we ended up with a survey sample of 324 stars; all stars are presented in Table B.1. With only a few exceptions, the spectral types we used were adopted from the works of Reid et al. (1995); Hawley et al. (1996); Gizis et al. (2002); Lépine et al. (2013); Alonso-Floriano et al. (2015). For details about spectral types we refer to Alonso-Floriano et al. (2015). J -band magnitudes are taken from the Two Micron All Sky Survey (Skrutskie

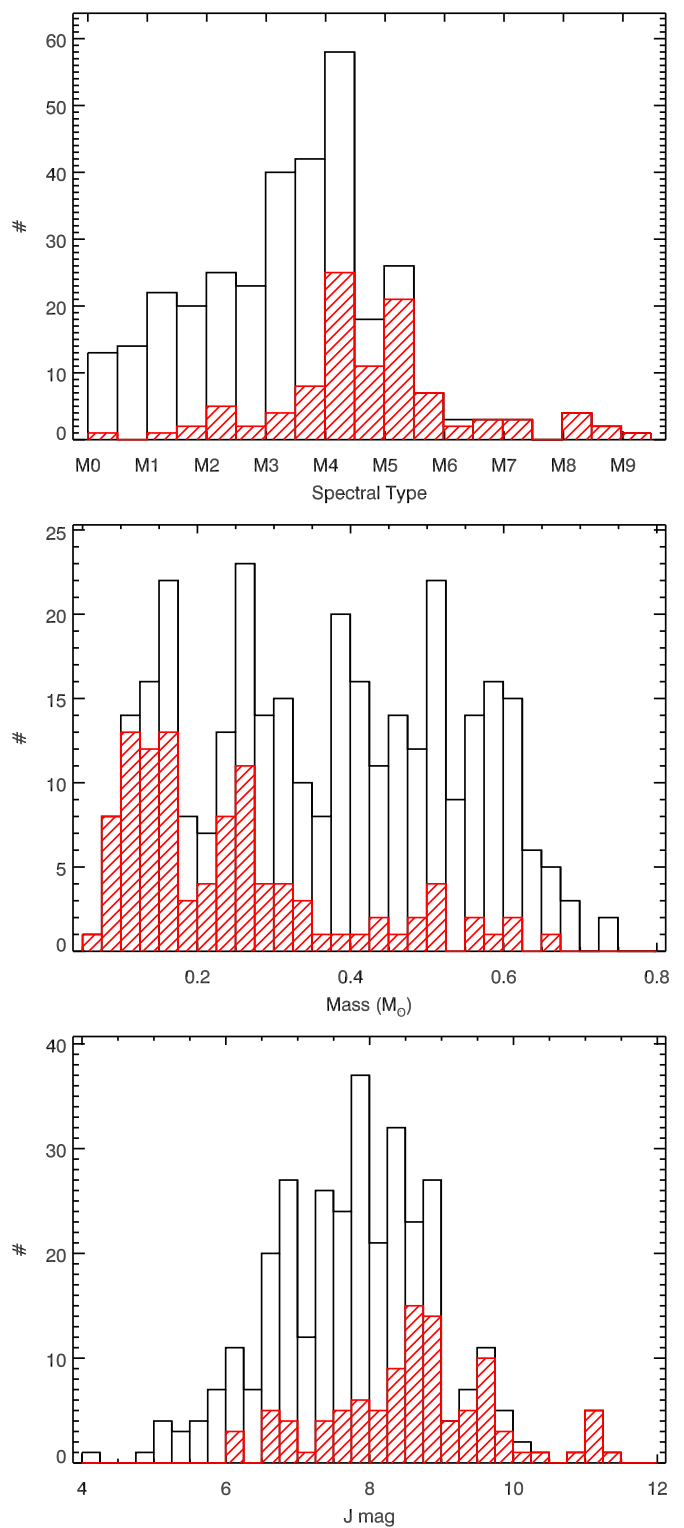


Fig. 2. From top to bottom: distribution of the CARMENES survey sample in spectral type, mass, and J -band magnitude. The subsample of stars with H α emission is shown in red.

et al. 2006). The typical limit for the J -band magnitude for our survey is $J = 10$ mag, and it is brighter for earlier spectral types. Some targets with known transiting planets were added to the sample although they are fainter than our typical survey targets. The distribution of the sample stars in spectral type, mass, and J -band magnitude is shown in Fig. 2. As a consequence of the steep

¹ <http://carmenes.cab.inta-csic.es>

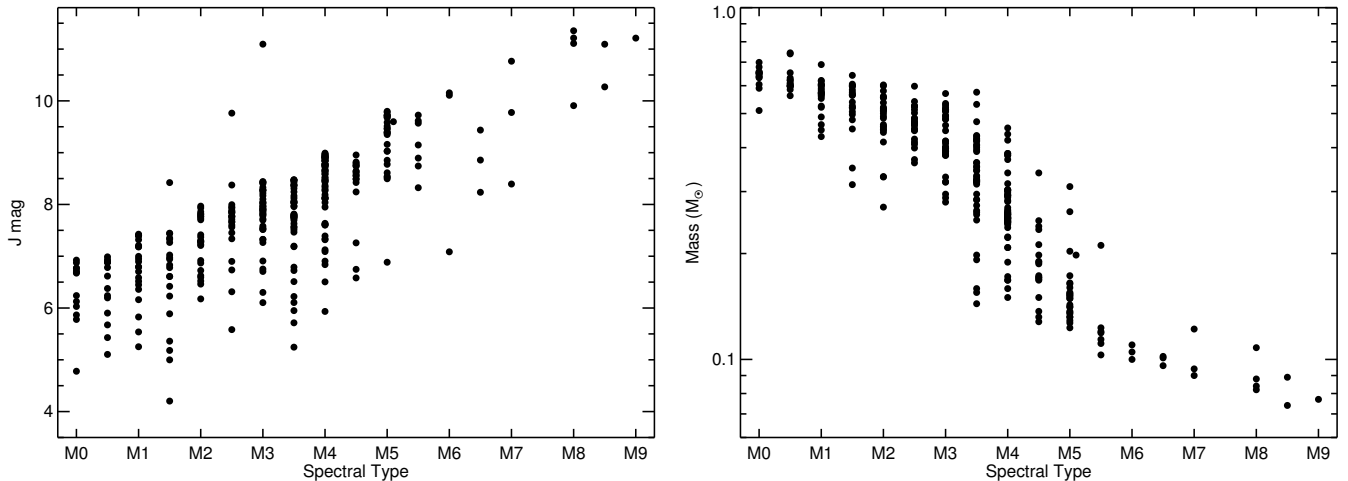


Fig. 3. J -band magnitude (left panel) and mass (right panel) for all stars of the CARMENES survey sample.

Table 1. Reference stars used for the calculation of $v \sin i$.

SpT interval	Reference star	SpT	P (d)	$v_{\text{Eq}}(P)$ (km s^{-1})
M0.0 – M0.5	GJ 548A	M0.0	111	0.3
M1.0 – M3.5	GJ 849	M3.5	39.2	0.6
M4.0 – M9.5	GJ 1256	M4.5	105.4	0.1

Notes. Radii and references for rotation periods are given in Table B.1.

decrease in luminosity toward late-type stars, only very few stars of our sample are later than M5. On the other hand, the distribution of our sample stars in mass is flatter and reaches down to the brown dwarf limit. This is mainly because there is only little difference in mass between dwarf stars in the spectral type range M6–M9. Individual values of J -band magnitude and mass are shown versus spectral types in Fig. 3. As a rule of thumb, for a mid-M $J = 9$ mag star, CARMENES reaches a S/N of 150 per pixel in the I band after 25 min exposure time.

We also report masses and activity level in terms of $\text{H}\alpha$ luminosity relative to bolometric luminosity in Table B.1. Masses are computed from K_s -band magnitudes according to the relations provided in Delfosse et al. (2000) and Benedict et al. (2016). We caution that masses below $0.1 M_\odot$ may be underestimated because these relations lose predictive utility for $M_K > 10$ mag (Benedict et al. 2016). $\text{H}\alpha$ luminosities are computed from measuring equivalent widths and converting them into luminosities (see, e.g., Reiners & Basri 2008). More details on $\text{H}\alpha$ measurements and other chromospheric lines in the CARMENES spectral range will be provided in a forthcoming paper.

2.2. Stellar rotation

We calculated the projected rotation velocities, $v \sin i$, from our spectra taken with CARMENES-VIS with the cross-correlation method. We computed the cross-correlation function (CCF) and calibrated the width of the CCF against artificially broadened spectra of a reference star (see, e.g., Reiners et al. 2012; Jeffers et al. 2017). We used coadded spectra from all observations for each star if more than five exposures were available (see Zech-

meister et al. 2017). For cross-correlation reference, we selected stars that were observed frequently (at least ten times), which guarantees a very high S/N reference (coadded) spectrum, and for which information on the rotation period from photometry is available. We used three different reference stars to minimize systematic errors caused by spectral mismatch (Table 1). All reference stars are relatively slow rotators, and their equatorial rotation velocity, v , is estimated from the rotation period, P , and radius, R , to lie well below our detection limit.

For each star, we computed a set of CCFs for individual orders of the CARMENES spectral format. The adopted $v \sin i$ is the average of values from orders that we found to provide reliable information about stellar rotation. Our criteria for the selected orders are the absence of significant telluric contamination and chromospheric emission lines, high S/N, and small influence from strong spectroscopic features, such as molecular band heads. The latter can introduce substantial systematic errors for relatively small differences in the spectral characteristics of our stars. The spectral regions that we chose cover the wavelength ranges 592–610 nm, 650.5–654 nm, and 660–685 nm in stars more massive than $M = 0.125 M_\odot$, and 741–757 nm, 774–810 nm, 840–843 nm, and 847–885 nm in less massive stars. As uncertainties, we report the standard deviations of the set of values calculated in these spectral chunks. All values of $v \sin i$ measured from the CARMENES spectra are given in Table B.1.

2.2.1. Fast and slow rotation

Many of the stars in our sample are relatively slow rotators. If Doppler broadening from stellar rotation is too small compared to the spectral resolution (and other broadening mechanisms), the effect cannot be reliably detected. In the case of M stars, turbulence and thermal broadening are on the order of 1–2 km s^{-1} in the lines of heavy ions and molecules, so that instrumental resolution determines the detection limit. For a criterion to reliably detect stellar rotation, we estimate that its Doppler effect must broaden the spectral lines by at least half a resolution element. In the case of CARMENES-VIS with $R = 94,600$, this means that $v \sin i = 2 \text{ km s}^{-1}$ is a conservative lower detection limit. For stars where we could not determine rotational broadening in excess of 2 km s^{-1} , we report this value as an upper limit for $v \sin i$ in Table B.1.

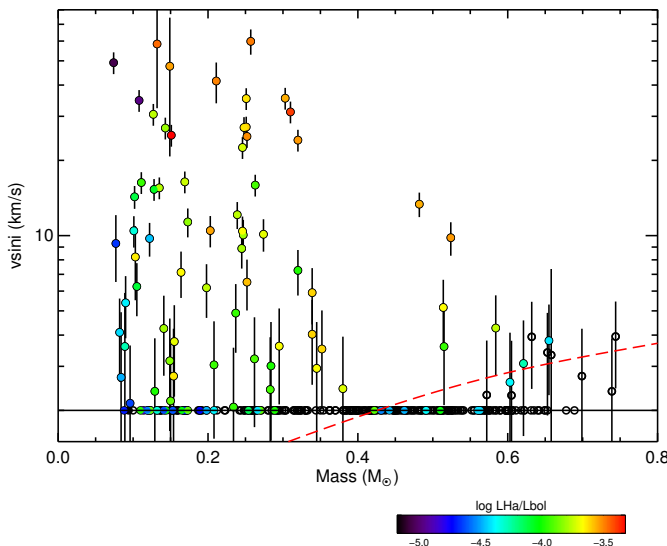


Fig. 4. Projected rotation velocity $v \sin i$ as a function of stellar mass. Stars with detected $\text{H}\alpha$ emission are shown as filled circles, and stars with no $\text{H}\alpha$ emission are shown as open circles. Colors indicate the level of $\text{H}\alpha$ emission as shown in the legend. Slow rotators are plotted at our detection limit of $v \sin i = 2 \text{ km s}^{-1}$. The red dashed line indicates values of v_{Eq} for stars with rotation periods $P = 10 \text{ d}$. Above this line, $\text{H}\alpha$ is always expected in emission (see text).

We find that 75 of our 324 sample stars (23 %) show significant rotational broadening. A detailed investigation of the fraction of active stars in our sample and a comparison to volume-limited M-dwarf samples is carried out in Jeffers et al. (2017). In that paper, a larger sample of stars was observed in preparation of the CARMENES survey. In the final CARMENES sample, we included 40 stars for which no information on $v \sin i$ was available before. We also compiled a list of rotation periods, P , measured from photometry. These values are reported together with the expected equatorial rotation velocity v_{Eq} . To calculate v_{Eq} from P , we determined the radius of each star according to the mass-radius relation for 4 Gyr old stars of solar metallicity from Baraffe et al. (1998).

The CARMENES results for $v \sin i$ are shown as a function of mass in Fig. 4. In this figure, we plot all stars with $\text{H}\alpha$ emission as filled circles and those without $\text{H}\alpha$ emission as open circles. All stars with significant rotational broadening and masses below $M = 0.55 \text{ M}_\odot$ are also $\text{H}\alpha$ -emitters; there is no inactive fast rotator below that mass limit. The fraction of active stars is higher at lower mass, a result that was found previously by other investigations (cf. Jeffers et al. 2017).

A handful of inactive stars with high masses ($M > 0.55 \text{ M}_\odot$) also show significant line broadening. The absence of $\text{H}\alpha$ emission in these stars deserves some deeper discussion. One possible explanation is that the spectra of these stars, in particular the wings of their atomic lines, are intrinsically different from “normal” M0 star spectra. The masses of these targets are relatively high for spectral type M0, which may point to peculiarities in the composition or age of these stars. This could lead to systematic differences between the spectra of our template M0 star and these apparently massive M0 stars, which cause a systematic offset in our determination of $v \sin i$. A second plausible explanation is that these stars are in fact rotating significantly faster than the inactive stars that are less massive, but here rotation is still not fast enough to produce $\text{H}\alpha$ emission. The left panel of Figure 8 in Jeffers et al. (2017) shows that normalized $\text{H}\alpha$ emis-

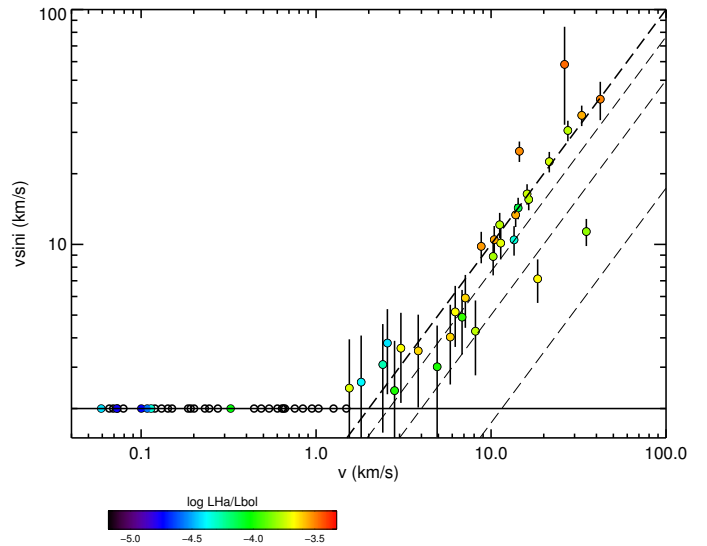


Fig. 5. Comparison between $v \sin i$ and equatorial velocity v estimated from photometric period and radius. Active stars are indicated as filled circles as in Fig. 4. Dashed lines show expected relations between $v \sin i$ and v for inclination angles $i = 90^\circ, 50^\circ, 30^\circ$, and 10° .

sion is proportional to rotation period in all M stars of spectral type M0–M4.5. $\text{H}\alpha$ emission, however, becomes undetectable at a level of $\log L_{\text{H}\alpha}/L_{\text{bol}} = -4.5$ in these stars. While all stars rotating faster than $P = 10 \text{ d}$ show $\text{H}\alpha$ in emission, activity in a growing fraction of the slower rotators falls below that threshold and cannot be detected anymore. In other words, at rotation periods of $P = 10 \text{ d}$ and slower, not all stars exhibit $\text{H}\alpha$ in emission. For our measurements, this means that the critical value of $v \sin i$ above which we always expect to find $\text{H}\alpha$ emission is a function of radius (or mass). We plot the critical value of $v \sin i$ that corresponds to $P = 10 \text{ d}$ as a red dashed line in Fig. 4. The critical value is below $v \sin i = 2 \text{ km s}^{-1}$ in stars less massive than $M = 0.45 \text{ M}_\odot$ but rises above our detection limit towards higher masses. The five stars with detected surface rotation but no $\text{H}\alpha$ emission are rotating at rates around the critical rate of $P = 10 \text{ d}$ or slower. We therefore conclude that our measurements of $v \sin i > 2 \text{ km s}^{-1}$ are consistent with the lack of $\text{H}\alpha$ emission in these stars.

2.2.2. Comparing photometric period to surface rotation

For many of our target stars we have information on rotational periods that we can combine with our measurements of projected surface rotation, $v \sin i$ (see Reiners et al. 2012). We plot $v \sin i$ against the expected equatorial rotation velocity according to photometric period and stellar radius in Fig. 5. We also show lines indicating $v \sin i$ as expected for a given v_{Eq} observed under inclination angles of $i = 90^\circ, 50^\circ, 30^\circ$, and 10° . We include our estimate on the inclination values from this comparison in Table B.1.

The majority of the stars with available P and $v \sin i$ follow the relation for $i = 90^\circ$ or a little below. Useful estimates of the inclination angle i can be given in cases where a photometric period and a measurement of surface rotation above the detection limit are available. Of these stars, about one half (15) have values of $v \sin i$ higher than v_{Eq} . Most of them are consistent with inclination angles $i = 90^\circ$ within the measurement uncertainties. We find only one star with a very small uncertainty in $v \sin i$,

but with a photometric period indicating much slower rotation (RX J0506.2); its rotation period of 0.89 d is inconsistent with the line broadening seen in our spectra. Nevertheless, we do not expect such high a fraction of stars observed nearly equator-on in a sample of stars in which inclination angles should be randomly distributed (uniform distribution in $\cos i$). Possible reasons for a bias toward large inclination angles include *i*) underestimated stellar radii, perhaps caused by a systematic bias in metallicity; *ii*) overestimated rotational periods, perhaps caused by misidentifying harmonics of P as the true rotational period or by differential rotation; *iii*) a systematically higher detection efficiency for photometric periods in stars observed under high inclination angles; and *iv*) overestimated values of $v \sin i$. For the latter, spectral mismatch between the targets and their reference stars is one obvious candidate. This may be particularly important for the three stars with $v \sin i > v_{\text{Eq}}$ that have surface rotation velocities between 2 and 4 km s $^{-1}$ and belong to the group of relatively massive stars discussed above (see Section 2.2.1).

One way to adjust the distribution of inclination angles is to select a different set of reference stars. We have experimented with other reference stars, and as expected, found other choices that can produce systematically lower values for $v \sin i$. Our principal requirement for the set of reference stars, however, was that spectral line broadening should be negligible and that external information from photometric measurements should be available. We conclude that the absolute values of $v \sin i$ need to be interpreted with great care, in particular when they are compared to photometric periods.

2.3. Absolute radial velocities

For our sample stars, we computed absolute radial velocities from the same data as were used for the calculation of $v \sin i$. From the CCFs that were calculated for a set of spectral orders, we derived RV offsets between each star and the reference. Because we here use coadded spectra, our results represent the mean radial velocities averaged over all observations for each star. An analysis of the RV variability of each target will be performed in detail for our planet search, but this is beyond the scope of this paper.

From our cross-correlation analysis, we obtained RVs for each star relative to its reference according to spectral type (see Table 1). Before coadding, all observed spectra were corrected for barycentric motion. Thus, the radial velocities are the true differences between the motion of the stars with respect to the solar system. The absolute values of the radial velocities, however, are unknown. We shifted our RVs to the absolute scale of the *Gaia* pre-launch catalog of RV standard stars provided by Soubiran et al. (2013). Our samples have three targets in common: Gl 450, Gl 514, and Gl 526. We computed the relative radial velocity shift between Gl 514 and our three reference stars, and shifted all our RVs such that the RVs of Gl 514 match the value from Soubiran et al. (2013, $v_{\text{rad}} = 14.386$ km s $^{-1}$). After calibration, the RVs of the two other stars, Gl 450 and Gl 526, also agree with the literature values within approximately 100 m s $^{-1}$ ($v_{\text{rad}} = 0.221$ km s $^{-1}$ and 15.570 km s $^{-1}$, respectively; Soubiran et al. 2013).

Absolute RVs for all our stars are provided in Table B.1. The typical relative uncertainties for our measurements are on the order of 10 m s $^{-1}$; they are dominated by spectral differences between the stars (note that we compute the radial velocity from the CCF relative to observed spectra of our reference stars). Faster

rotators typically have larger uncertainties for the same reasons as discussed in Section 2.2.

3. Spectral atlas

We present a spectral atlas of three representative M dwarfs of spectral types M1 (GX And), M3.5 (Luyten's star), and M7 (Tee-garden's star). The three objects are among the brightest targets of their spectral type and provide high-quality M-dwarf data at very different effective temperatures. One spectrum of each star is shown in the spectral atlas in Figs. A.1–A.40. We show the entire wavelength range from H α up to the red end of our spectral format (645–1710 nm). Information on the individual observations is summarized in Table 2. Each figure of the atlas covers an increase of approximately 2.3 % in wavelength, that is, ~ 2100 resolution elements. The top panels show a spectrum of the telluric standard star 50 Cas as in Fig. 1. In the other three panels, we present the three M-dwarf spectra in black, together with a PHOENIX model spectrum from Husser et al. (2013) in red, calculated for approximately the atmospheric parameters we expect for the stars' spectral types, that is, 3700 K (M1), 3400 K (M3.5), and 2600 K (M7). We chose $\log g = 5.0$ and solar metallicity for this comparison. Model spectra are artificially broadened to match the spectral resolution of our observations. In the top panel of the atlas figures, the spectrum of the telluric standard is shown with annotations of the most prominent absorption features. The hydrogen H α lines are stellar features, positions are taken from The Atomic Line List v2.04.² In the second panel, we show the spectrum of GX And together with annotations of the most prominent atomic and molecular absorption features seen in M dwarfs. Line positions of atomic lines are taken from VALD (Ryabchikova et al. 2015), information on molecular bands was compiled from Cushing et al. (2005). We chose to show our observed spectra without applying any Doppler shift so that telluric lines appear at the same position in all panels of our atlas. Because of barycentric motion and the stars' radial velocities, the spectral features are therefore slightly shifted. In order to match the features of the model spectra to our observations, we Doppler-shifted the model spectra accordingly. The values that we applied are given in Table 2.

Our wavelength range covers parts of the range shown in the atlas from Tinney & Reid (1998), which contains the spectral range up to 920 nm. In the following, we discuss the spectroscopic features observed at wavelengths redward of 920 nm only. For a discussion of M-dwarf spectra at shorter wavelengths, we refer to Tinney & Reid (1998), for instance.

3.1. Y band

The spectral range around 970 nm contains a number of strong Ti lines that are very useful for the study of M-dwarf magnetic fields (e.g., Kochukhov & Lavail 2017; Shulyak et al. 2017). These lines are embedded in telluric water absorption, which needs to be corrected for. The strong water absorption ends at around 980 nm, just before the well-known Wing-Ford band of molecular FeH sets in (see, e.g., Reiners & Basri 2006). The wavelength range 985–1100 nm is virtually free of telluric absorption. It contains mostly FeH lines, several strong atomic Ti lines, a prominent Ca line, and a handful of weaker lines from other atoms. Absorption from the FeH band has intensively been used to measure rotation and magnetic fields in M dwarfs. The great advantage of the Wing-Ford band is that it contains a large

² <http://www.pa.uky.edu/~peter/atomic/>

Table 2. Basic information about spectra shown in the spectral atlas.

Target	SpT	Date (UT)	Exp.Time (s)	S/N 874 nm / 1120 nm	Air mass	Doppler shift ^a (km s ⁻¹)
GX And	M1	2016, Nov 10 20:57	300 s	290 / 420	1.01	22
Luyten's star	M3.5	2016, Dec 31 00:58	230 s	150 / 230	1.18	10
Teegarden's star	M7	2016, Nov 16 22:32	1500 s	72 / 130	1.08	73

Notes. ^a Doppler shift is applied to the model spectra.

number of relatively isolated absorption lines that are not as densely packed as the TiO or VO lines in the visual wavelength range, which allows a line profile analysis of individual lines at least in early- and mid-M stars (e.g., Reiners 2007). FeH lines have very different Landé g-factors that are useful for differential investigation of Zeeman broadening or stellar metallicity (Shulyak et al. 2011).

Some visual spectrographs based on CCDs can reach out to this wavelength range, such as UVES/VLT, HIRES/Keck, or ESPADONS/CFHT. They have been used to provide spectral quality that so far was superior to most of the spectra taken with infrared detectors. CARMENES NIR also covers this range with an infrared detector, but here the efficiency was optimized to reach high throughput at these wavelengths. Therefore, CARMENES has become one of the most efficient instruments specifically in this wavelength range.

Our comparison between observations and model spectra at all three spectral types shows that many molecular and atomic lines are well reproduced by the models. However, the intensity of the FeH molecular lines is often overestimated, and a set of strong absorption features appears in the M7 model at wavelengths around 1050 nm that are not detected in the observed spectrum. We did not make an attempt to find the models that are most similar to our observed spectra, but the physical setup of these particular models is clearly either lacking adequate input data (e.g., better molecular line data) or the models inappropriately simulate the physical situation at very low effective temperatures (at least for this wavelength region), or both.³

Heavy water absorption between 1100 nm and 1200 nm separates the *Y* band from the *J* band. At high spectral resolution, we can identify stellar absorption lines from Na, K, Fe, Cr, and Mg embedded in the forest of water lines. Some of them are strong and isolated enough, so that they might be useful for a line profile analysis.

3.2. *J* band

The *J* band starts around 1200 nm, where the water absorption band becomes much weaker. The transparent atmospheric window extends until water is again detected redward of 1300 nm. The region in between is not as free of telluric lines as the *Y* band because there is an additional molecular band from O₂ around 1270 nm. The M-dwarf spectra in the *J* band are very poor in absorption lines compared to the other spectral regions in the visual and near-infrared range. There are no substantial molecular bands similar to the TiO, VO, or FeH bands at shorter wavelengths. The two K₁ lines near 1250 nm stand out promi-

nently, and there are a few lines from Ca, Ti, Fe, and Mn around 1286 nm. A Na₁ line is buried in telluric O₂ absorption, and two Al₁ lines appear at the red end of the *J* band, where water absorption is relevant again (the two Al₁ lines are unfortunately lost in a gap of the CARMENES spectral format). Another line of Mn₁ is visible around 1330 nm before very strong water absorption separates the *J* from the *H* band. We do not show the wavelength range between 13,850 and 1480 nm because almost no starlight passes through the dense water features.

The spectral models show good agreement with the observed spectra. In the *J* band, no prominent features seem to be missing in the models, and none of the features predicted by the models are missing in the spectra. The long exposure of the M7 star shows a number of sky emission lines from OH airglow (Oliva et al. 2015).

3.3. *H* band

At the blue end of the *H* band, water absorption is significantly reduced at around 1500 nm until the end of our spectral format at 1710 nm. Additional telluric absorption bands from CO₂ are visible at 1540 nm, 1570 nm, 1600 nm, and 1640 nm (Herzberg 1950).

Around 1480 nm, a series of stellar molecular OH absorption lines appears among the water lines. The set of OH lines covers the entire *H* band and adds a significant number of stellar absorption features. In terms of atomic lines, the situation is similar to the *J* band, with only a few scattered weak lines throughout the entire band. These lines are Mg₁ at 1505 nm (partially lost in spectral format gaps), very weak lines of K₁ 1517 nm, a handful of lines from Fe₁ and Ti₁ throughout the band, and a set of Ca₁ lines at 1615 nm. Overall, these lines are all relatively weak, which implies that the amount of information available for line profile analysis using a high-resolution spectrograph is limited.

Another component of stellar absorption that becomes stronger toward later spectral types appears throughout the entire *H* band. This component is significantly above the noise level and is also predicted by the models. The absorption is probably due to FeH, but the lines are too dense for an individual line analysis.

4. Radial velocity information content

The RV precision that can be achieved in a spectroscopic RV measurement depends on the number of photons that can be collected at some particular wavelength, that is, on the S/N and also on the amount of spectroscopic information that is available to measure the Doppler shift, that is, the RV information content (Connes 1985; Butler et al. 1996; Bouchy et al. 2001). At stellar photospheric temperatures, electronic transitions from atoms and molecules typically generate many spectral lines at optical wavelengths, but fewer at longer wavelengths. In low-mass stars,

³ We note that observations and models also disagree in several strong alkali lines where the models predict too wide damping wings (see, e.g., Reiners et al. 2007), and the models overpredict the strength of the lithium line at 670.8 nm because lithium depletion was not taken into account.

ro-vibrational transitions add molecular bands at red optical and near-infrared wavelengths. Thus, the RV information content is typically higher at short optical wavelengths, but toward later spectral types, the photon-dominated S/N grows dramatically from blue optical toward infrared wavelengths.

Detailed simulations of the photon-limited RV precision in M dwarfs were carried out by Reiners et al. (2010); Rodler et al. (2011); Bottom et al. (2013); Plavchan et al. (2015); Figueira et al. (2016). With only very few exceptions, these studies relied on synthetic spectra from model atmosphere simulations. These works agree with the general picture that more RV information is available at short wavelengths, but about the details of which spectral range is better than another, after taking into account also the available number of photons, there are discrepancies by a factor of two or more. One reason for the discrepancies is that different models were used; model predictions for the occurrence of molecular bands depend on input parameters about the stellar atmosphere and molecular physics. Another reason is the treatment of telluric lines, which becomes a very significant factor at near-infrared wavelengths.

The spectra from our survey provide empirical information on the RV precision that is achievable in M dwarfs across the wavelength range 520–1710 nm. A major motivation to observe M dwarfs at longer wavelengths is that the measurement uncertainty in any spectral bin, $(S/N)^{-1}$, decreases dramatically from V band to J band. Nevertheless, there are far fewer spectroscopic features, that is, spectroscopic RV information, at longer wavelengths. The ratio of the two is the RV precision that can be achieved in an observation. In the following, we provide the first empirical information on the wavelength dependence of the RV precision in M dwarfs from a significant number of observations.

We follow the definition of Bouchy et al. (2001); the RV precision that can be reached in an observation of a star in a given wavelength range can be written as

$$\delta v_{\text{rms}} = \frac{c}{Q \cdot S/N}, \quad (1)$$

where c is the speed of light and Q is the quality factor. The latter is essentially the cumulative spectral gradient across the wavelength range that is used for analysis. It depends on the intrinsic spectral features of the star, but also on additional line broadening, in particular, spectral resolution and stellar surface rotation, $v \sin i$.

4.1. Empirical radial velocity information

For all CARMENES observations, we have empirical values of δv_{rms} for each individual spectral order. For details on the calculation of δv_{rms} , we refer to Zechmeister et al. (2017), where it is called ϵ_v . In short, our pipeline fits each individual spectrum to a coadded template calculated from all our observations of that star. The value of δv_{rms} is the uncertainty of the optimal radial velocity in this fit. We begin our analysis of the RV precision by looking into its dependence on wavelength for different M-star spectral types. For this analysis, we used 6625 observations that were taken with both CARMENES channels simultaneously. Observations were only considered for the 261 stars that were observed more than five times with each of the channels. Of these data, the values of δv_{rms} differ even for stars of the same spectral types because the individual stars are not equally bright and they are observed under varying sky conditions, which results in different S/Ns. Furthermore, the quality factor can differ between stars of the same spectral type because of rotation. In

order to make our observations comparable, we rescaled the RV precisions δv_{rms} for each individual spectrum according to S/N and $v \sin i$. Before doing so, we checked in the individual values that δv_{rms} could be described as a function of both S/N and $v \sin i$. In both cases, we found clear relations for all stars of a given spectral type by comparing δv_{rms} in one order. The relations are identical between the different spectral types. As expected, we find that δv_{rms} is directly proportional to S/N^{-1} . For the dependence on $v \sin i$, we find a relation of $\delta v_{\text{rms}} \propto (v \sin i)^{0.6}$. We scaled the values of δv_{rms} between different stars and observations to a fiducial observation of a slowly rotating star observed at an S/N of 150 per resolution element in the J band.

We show in Fig. 6 the rescaled RV precision δv_{rms} for all individual spectral orders for which RVs were calculated by our analysis procedure (excluding orders with very heavy telluric contamination or too low S/N). The wavelength range we considered for this analysis is 550–1700 nm. From the rescaled values, we computed for each order the median value from all observations of stars with similar spectral types. These are the black points plotted in the individual panels of Fig. 6. The error bars shown are the 25th and the 75th percentile of all observations, that is, half of all observations for any given spectral type and spectral order fall within the range of the error bars. The number of observations used for each spectral type plot is given in upper right corner of each panel.

The information from individual orders is very useful to assess the amount of information in small spectral regions. To gain a better idea about the RV precision calculated from larger wavelength areas, we quadratically added the RV information from different spectral orders in 100 nm (VIS) or 200 nm (NIR) bands. This choice is rather arbitrary, but it partially reflects the fact that at constant spectral resolution, and at wavelengths that are longer by a factor of two, the same number of resolution elements are contained in a range that is a factor of two longer in units of wavelength. In the NIR channel, our 200 nm chunks are also similar to the Y , J , and H bands. Their values are shown as gray circles with horizontal lines that mark the wavelength ranges covered in each band. Finally, we quadratically added RV information across the wavelength ranges that are covered by the CARMENES VIS and NIR channels in blue and red, respectively.

From our general considerations about S/N and the distribution of spectroscopic features (Section 1), we expect that in early-M type stars the larger amount of spectroscopic information at shorter wavelengths leads to better RV precision at visual wavelengths than at infrared wavelengths. In late-M type stars, however, the general lack of photons at visual wavelengths must lead to a severe loss of information so that the RV precision at infrared wavelengths improves relative to the performance at visual wavelengths. This picture is consistent with the empirical results we obtain from Fig. 6. In all stars of spectral type M0–M5, the RV precision improves from the shortest wavelengths at 550 nm toward 700 nm, where much RV information is contained in the TiO band that starts at 706 nm. The next spectral orders up to about 900 nm perform somewhat worse, but still relatively well. We find another region of excellent RV precision around 770 nm, where the TiO system that sets in around 760 nm is no longer contaminated by the oxygen A band. Spectral orders at wavelengths longer than 900 nm carry significantly less RV information than those at shorter wavelengths in stars of spectral types M0–M5. Specifically, when we combined all RV information in the wavelength ranges covered by CARMENES VIS and NIR (550–960 nm and 960–1700 nm, respectively), we found that in stars of spectral type M5, the RV information con-

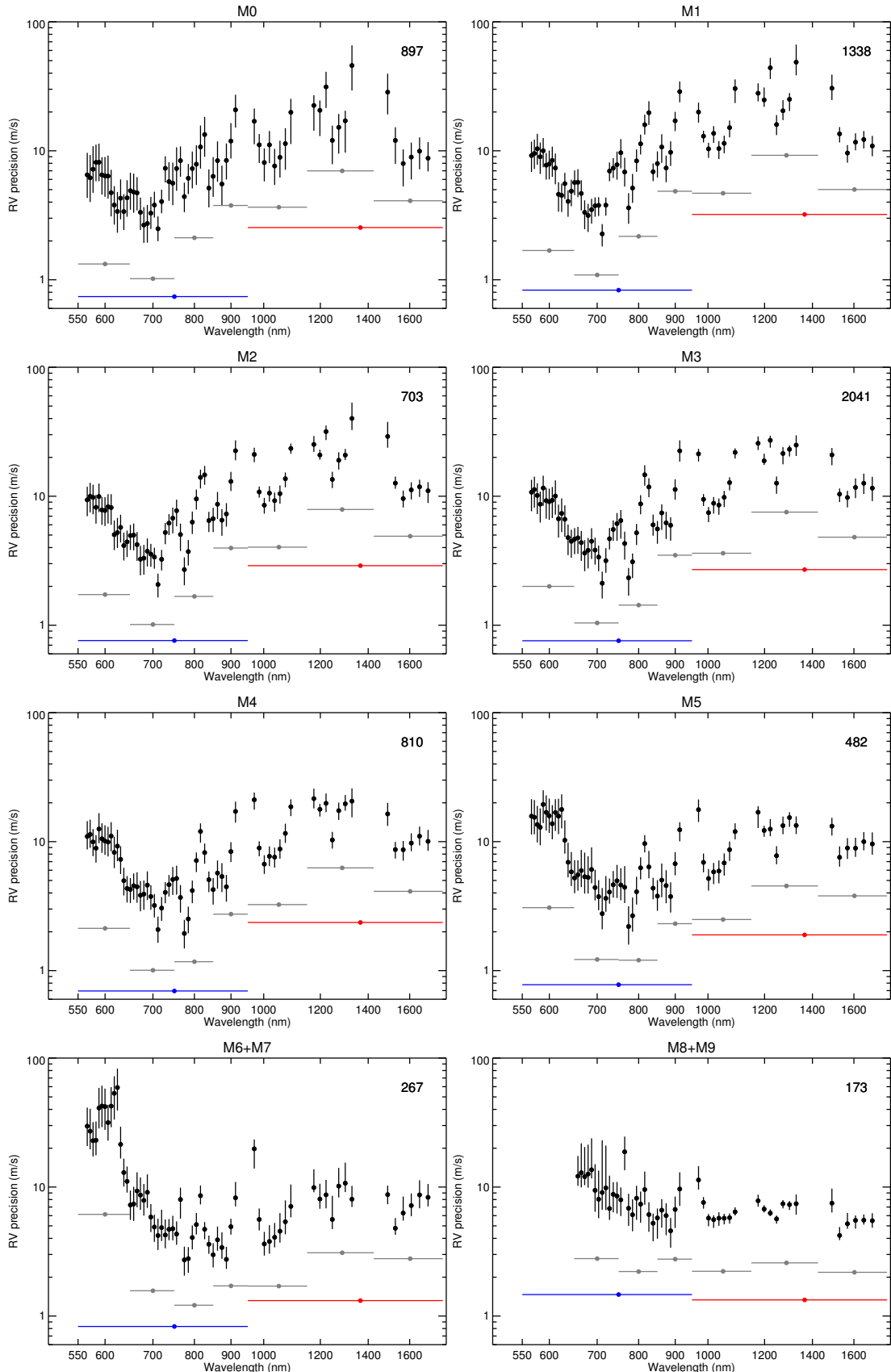


Fig. 6. Empirical RV precision (δv_{rms}) for individual spectral orders of CARMENES observed in the sample stars. Each panel shows for each order the median value for all observations taken of stars with spectral types M0 and M0.5 (upper left panel), M1 and M1.5 (upper right panel), and so forth. Error bars mark the 25th and 75th percentile of all observations. Gray points show quadratically added δv_{rms} for 100 or 200 nm wide spectral windows, as indicated by the horizontal bars. Blue and red symbols show the CARMENES VIS and NIR spectral ranges. The number of observations per spectral type is given in the upper right corner of each panel.

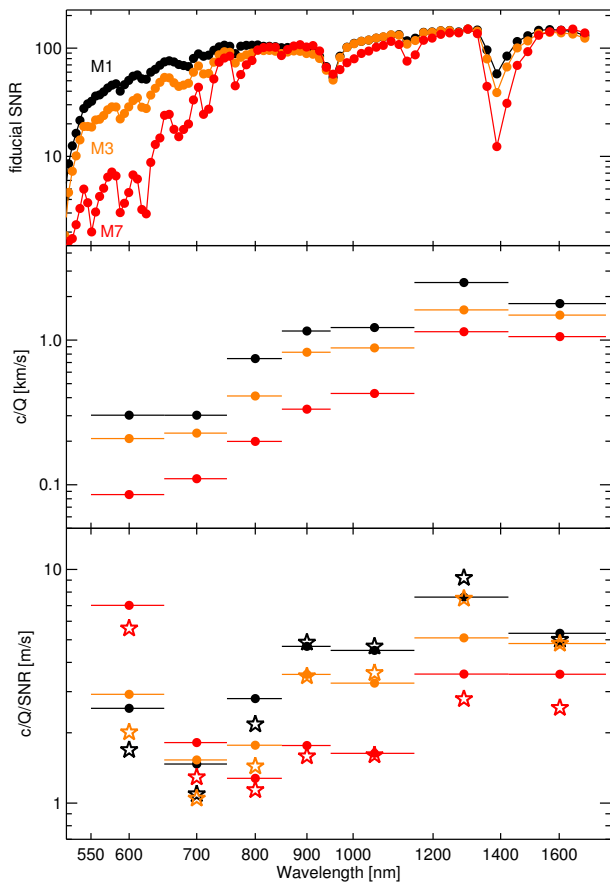


Fig. 7. Comparison between empirical values for RV precision δv_{rms} and its constituents S/N and c/Q . *Top panel:* normalized S/N from individual spectra of GX And (M1), Luyten’s star (M3.5), and Teegarden’s star (M7). *Middle panel:* cumulative spectroscopic information c/Q calculated from coadded spectra of the three example stars. *Bottom panel:* ratio between c/Q and S/N (filled circles) together with empirical values of δv_{rms} (open stars, see Fig. 6).

tent is about a factor of 2.5 higher in the VIS channel than in the NIR channel.

For stars of spectral type M6 and later, we can observe in Fig. 6 the influence of the spectral energy distribution on RV precision. In our M6 and M7 stars, we can still compute RVs at wavelengths down to 550 nm, but the poor S/N leads to typical RV precisions exceeding 20 m s $^{-1}$ (the spectral orders at wavelengths shorter than 650 nm are no longer computed in M8 and M9 stars). Nevertheless, the RV precision we observe in stars of spectral types M6–M9 is still relatively high (the values are low) at red visual wavelengths. In M6 and M7 stars, most RV information is available at wavelengths 700–900 nm, and the combined VIS channel information outperforms the NIR channel information by approximately 50 %. In our combined sample of M8 and M9 stars, the VIS and the NIR channel are roughly equal in terms of RV information. In particular, these stars still show a high RV signal at 800–900 nm. Similar performance is reached in the Y and H bands; the J band provides slightly less information.

4.2. Spectroscopic information and signal-to-noise ratio

As next step, we aim to distinguish the factors of δv_{rms} , Q , and S/N, and individually show them as a function of wavelength.

Our goal here is to see in which way the influence of S/N and the amount of spectral information, Q , determines the RV precision in M dwarfs. As an example of the S/N as a function of wavelength, we show normalized S/N curves for three stars in the top panel of Fig. 7 as observed with CARMENES. For our example, we again selected the three stars shown in our spectroscopic atlas: M1: GX And (black), M3.5: Luyten’s star (orange), and M7: Teegarden’s star (red). The S/N curves are normalized to S/N = 150 at J band. We clearly see the lack of signal at short wavelengths in the very cool M7 star. For the S/N curve, we used all available spectral orders, including those with strong telluric absorption. Thus, the S/N here is a combination of the stellar flux and telluric absorption.

In the center panel of Fig. 7, we visualize the amount of spectroscopic information (c/Q) that we calculated from observed spectra of the three example stars. We computed this value as the cumulative spectral gradient across the wavelength ranges, see Eq. (6) in Butler et al. (1996). The wavelength regions are the same 100 nm and 200 nm wide windows as in Fig. 6. For this computation, we used the coadded spectra from all observations of our three example stars; see Zechmeister et al. (2017) for details. During coadding, wavelength regions contaminated by telluric lines were masked. As discussed below, this is a potential source of uncertainty particularly at long wavelengths, where telluric contamination is significant. For the computation of c/Q , the photon noise in the coadded spectra is negligible. The number of observations used per star at VIS/NIR are GX And: 181/163; Luyten’s star: 691/677; and Teegarden’s star: 48/43. In all three example stars, there is significantly more RV information at shorter wavelengths. Furthermore, the spectra of cooler stars carry more RV information than the spectra from early-M dwarfs because they exhibit more spectral features from molecular absorption.

In the bottom panel of Fig. 7, we compare RV uncertainties for CARMENES spectra following two different approaches: a) assuming a signal-to-noise ratio of $S/N = 150$ at the J band, we calculate the amount of spectroscopic RV information, $(c/Q)/S/N$, using a coadded high-quality spectrum for each of our example stars (filled circles; see Eq. 1); and b) from a large number of observations (e.g., 2041 CARMENES observations of M3 and M3.5 stars), we calculated the median of their internal RV uncertainties, δv_{rms} , (open stars) from fitting every individual spectrum to a coadded template of the observed star as shown in Fig. 6 (scaled to $S/N = 150$ at the J band and slow rotation, see above). With this comparison, we aim to reveal any systematic problems in our RV determination. In general, the values calculated following the two different approaches compare very well; for all wavelength bands and spectral types, they agree within a factor of two; most of the values agree even better. Consistent with our calculations from spectral fitting, our analysis of the S/N and the amount of spectroscopic features shows that in all M dwarfs down to M7, the highest RV precision can be reached at around 700 nm or 800 nm. At 600 nm, observations of M dwarfs show considerably lower RV precision because of their very low S/N. At 700 and 800 nm, however, the signal is still high enough to provide higher RV precision than regions at longer wavelengths (it levels out only in M8/9 stars, see Fig. 6). The reason for this is the substantial loss in spectroscopic features from VIS to NIR wavelengths.

One important source of uncertainty in our calculation of Q is the occurrence of telluric features, in particular, at infrared wavelengths. In the bottom panel of Fig. 7, we observe that the values of $(c/Q)/S/N$ are lower than our measured RV precision, in particular in the J band. A possible explanation is that our

coadded spectra are contaminated by telluric features. These features can contribute to Q because they introduce additional spectral gradients. They also increase the value of our empirically measured RV uncertainty because the individual observations and the coadded spectra do not resemble each other at these features. The result of poorly treated telluric lines is therefore a bias toward higher values in our empirical RV uncertainty and toward lower values in the uncertainty estimate $(c/Q)/S/N$. We identify the treatment of telluric lines as one of the main areas where infrared (and also red visual) RV precision can be improved, but we also note that in the presence of a sufficient amount of spectroscopic features like in our M7 star, this appears to be a negligible problem.

There are a number of instrumental effects that can affect our analysis of precision vs. λ from the CARMENES data. These effects include global efficiency offsets between the VIS and the NIR, varying spectrograph throughput and detector efficiency, or λ -dependent read noise. The difference in spectral resolution between the VIS and the NIR channel slightly penalizes the NIR channel RV precision, but the expected effect is on the order of only 10 % and not significant for our conclusions. Although our analysis was carried out using observed data and S/N values that were determined empirically, we note that instrumental effects may be hidden. However, the two CARMENES channels are very similar in their optical design and performance, and our results can probably be taken as fairly typical for other high-resolution spectrographs.

5. Summary

After all targets of the CARMENES survey were observed at least once, we derived basic spectroscopic information for each target about radial velocity, $H\alpha$ emission, and projected surface rotation. We provide this information together with the list of the 324 targets of our CARMENES M-dwarf survey in this work. For each star, we provide one spectrum observed with the two CARMENES channels, which cover the wavelength range 550–1700 nm. This is the first large library of high-resolution near-infrared spectra of low-mass stars. We also show a spectroscopic atlas of three example M dwarfs (M1, M3.5, M7) and compare their spectra to a telluric standard and synthetic models at very high spectral resolution. We find that the synthetic spectra in general succeed in predicting the main features in M-dwarf spectra, but the amount of spectroscopic features is sometimes higher than in the models.

Our analysis of stellar rotation and activity adds precise $v \sin i$ measurements to the available catalogues of M-dwarf rotation. Several of our stars rotate as fast as $v \sin i = 20 \text{ km s}^{-1}$ and more. Our values are included in the more detailed analysis of rotation and activity by Jeffers et al. (2017). They are consistent with the general picture of M-dwarf activity. We find some very early M-dwarfs that exhibit significant rotation but no $H\alpha$ emission. These stars have rotation periods close to $P = 10 \text{ d}$, and they are probably rotating slowly enough to explain the lack of $H\alpha$ emission (see also Jeffers et al. 2017).

We employed several thousand observations of M dwarfs taken at visual and near-infrared wavelengths to calculate the RV uncertainty as a function of wavelength for individual spectral subtypes. We conclude that the wavelength range 700–900 nm provides an excellent source of RV information for all M dwarfs. At shorter wavelengths, the RV precision is lower and deteriorates toward later spectral types. At longer wavelengths, the RV precision is significantly lower up to spectral types M6/M7. The turnover point where RV information content at NIR wave-

lengths becomes comparable to the one at VIS wavelengths is located at spectral types as late as M8/M9.

Our results answer the question at which wavelength the best RV precision can be reached in observations of M dwarfs with a stabilized spectrograph: the optimal range for M-dwarf RV spectroscopy is the spectral range 700–900 nm. Calculating the spectroscopic quality factor Q and the S/N for three example stars, we showed that our conclusions about the RV uncertainties are consistent with the spectroscopic information we find in the spectra. At wavelengths shorter than 700 nm, the lack of photons limits the RV precision; at wavelengths longer than 900 nm, the amount of spectroscopic information is so much lower than at shorter wavelengths that the advantage in S/N cannot compensate for the loss in RV precision. Only in the latest spectral types (M8 and M9) did we find the RV precision at near-infrared wavelengths to match the amount of information at shorter wavelengths.

Our result is especially interesting for other planned M-dwarf surveys and the spectroscopic follow-up of transiting M dwarfs. Instruments used for this purpose are often mounted at 4m class telescopes that have a similar performance as the 3.5m telescope at Calar Alto that is used for the CARMENES survey. For these, very late-M dwarfs are difficult to observe because they are extremely faint (at all wavelengths), and the limited RV precision is further affected by their often high rotation rates. Thus, instruments at 4m class telescopes will typically reach an RV precision on the order of 1 m s^{-1} only in early- and mid-M dwarfs, where the spectral range 700–900 nm is the most efficient. However, an RV precision of 2 m s^{-1} can be reached at 4m class telescopes within reasonable times in many stars of spectral type M6 and earlier. Here, NIR RV data cannot outperform red visual RV observations, but NIR RVs can reach below the typical limit of radial velocity jitter in M dwarfs that is on the order of $3\text{--}4 \text{ m s}^{-1}$ (Bonfils et al. 2013). The main reasons for this jitter are corotating active regions (including their effect on convective blueshift) and granulation, and their RV signal is expected to be wavelength dependent. The combination of RV observations at visual and near-infrared wavelengths is ideal to distinguish between Keplerian signals and stellar variability. CARMENES delivers these data across a very large wavelength range. It is therefore optimally suited to search for low-mass planets around mid-type M dwarfs where variability is a serious concern.

Acknowledgements. We thank an anonymous referee for prompt attention and helpful comments that helped to improve the quality of this paper. CARMENES is an instrument for the Centro Astronómico Hispano-Alemán de Calar Alto (CAHA, Almería, Spain). CARMENES is funded by the German Max-Planck-Gesellschaft (MPG), the Spanish Consejo Superior de Investigaciones Científicas (CSIC), the European Union through FEDER/ERF FIOTS-2011-02 funds, and the members of the CARMENES Consortium (Max-Planck-Institut für Astronomie, Instituto de Astrofísica de Andalucía, Landessternwarte Königstuhl, Institut de Ciències de l’Espai, Institut für Astrophysik Göttingen, Universidad Complutense de Madrid, Thüringer Landessternwarte Tautenburg, Instituto de Astrofísica de Canarias, Hamburger Sternwarte, Centro de Astrobiología and Centro Astronómico Hispano-Alemán), with additional contributions by the Spanish Ministry of Economy, the German Science Foundation through the Major Research Instrumentation Programme and DFG Research Unit FOR2544 “Blue Planets around Red Stars”, the Klaus Tschira Stiftung, the states of Baden-Württemberg and Niedersachsen, and by the Junta de Andalucía. This work has made use of the VALD database, operated at Uppsala University, the Institute of Astronomy RAS in Moscow, and the University of Vienna. We acknowledge the following funding programs: European Research Council (ERC-279347), Deutsche Forschungsgemeinschaft (RE 1664/12-1, RE 2694/4-1), Bundesministerium für Bildung und Forschung (BMBF-05A14MG3, BMBF-05A17MG3), Spanish Ministry of Economy and Competitiveness (MINECO, grants AYA2015-68012-C2-2-P, AYA2016-79425-C3-1,2,3-P, AYA2015-69350-C3-2-P, AYA2014-54348-C03-01, AYA2014-56359-P, AYA2014-54348-C3-2-R, AYA2016-79425-C3-3-P and 2013 Ramón y Cajal program RYC-2013-14875), Fondo Europeo de Desarrollo Regional (FEDER, grant ESP2016-

80435-C2-1-R, ESP2015-65712- C5-5-R), Generalitat de Catalunya/CERCA programme, Spanish Ministerio de Educacin, Cultura y Deporte, programa de Formacin de Profesorado Universitario (grant FPU15/01476), Deutsches Zentrum fr Luft- und Raumfahrt (grants 50OW0204 and 50OO1501), Office of Naval Research Global (award no. N62909-15-1-2011), Mexican CONACyT grant CB-2012-183007.

References

- Alonso-Floriano, F. J., Morales, J. C., Caballero, J. A., et al. 2015, *A&A*, 577, A128
- Amado, P. J. 2007, Communications in Asteroseismology, 151, 57
- Amado, P. J., Surez, J. C., Garrido, R., Moya, A., & Martn-Ruiz, S. 2007, Communications in Asteroseismology, 150, 311
- Anglada-Escud, G., Amado, P. J., Barnes, J., et al. 2016, *Nature*, 536, 437
- Anglada-Escud, G., Arriagada, P., Tuomi, M., et al. 2014, *MNRAS*, 443, L89
- Anglada-Escud, G., Tuomi, M., Gerlach, E., et al. 2013, *A&A*, 556, A126
- Artigau, ., Kouach, D., Donati, J.-F., et al. 2014, in Proc. SPIE, Vol. 9147, Ground-based and Airborne Instrumentation for Astronomy V, 914715
- Baliunas, S. L., Hartmann, L., Noyes, R. W., et al. 1983, *ApJ*, 275, 752
- Baraffe, I., Chabrier, G., Allard, F., & Hauschildt, P. H. 1998, *A&A*, 337, 403
- Barnes, J. R., Jeffers, S. V., Anglada-Escud, G., et al. 2017, *MNRAS*, 466, 1733
- Barnes, J. R., Jeffers, S. V., & Jones, H. R. A. 2011, *MNRAS*, 412, 1599
- Benedict, G. F., Henry, T. J., Franz, O. G., et al. 2016, *AJ*, 152, 141
- Bonfils, X., Delfosse, X., Udry, S., et al. 2013, *A&A*, 549, A109
- Bottom, M., Muirhead, P. S., Johnson, J. A., & Blake, C. H. 2013, *PASP*, 125, 240
- Bouchy, F., Pepe, F., & Queloz, D. 2001, *A&A*, 374, 733
- Butler, R. P., Marcy, G. W., Williams, E., et al. 1996, *PASP*, 108, 500
- Caballero, J. A., Gurdia, J., Lpez del Fresno, M., et al. 2016, in Proc. SPIE, Vol. 9910, Observatory Operations: Strategies, Processes, and Systems VI, 99100E
- Campbell, B. & Walker, G. A. H. 1979, *PASP*, 91, 540
- Cegla, H. M., Stassun, K. G., Watson, C. A., Bastien, F. A., & Pepper, J. 2014, *ApJ*, 780, 104
- Chugainov, P. F. 1974, Izvestiya Ordena Trudovogo Krasnogo Znameni Krymskoy Astrofizicheskoy Observatorii, 52, 3
- Claudi, R., Benatti, S., Carleo, I., et al. 2016, in Proc. SPIE, Vol. 9908, Ground-based and Airborne Instrumentation for Astronomy VI, 99081A
- Connes, P. 1985, *Ap&SS*, 110, 211
- Corts-Contreras, M., B jar, V. J. S., Caballero, J. A., et al. 2017, *A&A*, 597, A47
- Crepp, J. R., Crass, J., King, D., et al. 2016, in Proc. SPIE, Vol. 9908, Ground-based and Airborne Instrumentation for Astronomy VI, 990819
- Cushing, M. C., Rayner, J. T., & Vacca, W. D. 2005, *ApJ*, 623, 1115
- Delfosse, X., Forveille, T., S gransan, D., et al. 2000, *A&A*, 364, 217
- Desort, M., Lagrange, A.-M., Galland, F., Udry, S., & Mayor, M. 2007, *A&A*, 473, 983
- Fekel, F. C. & Henry, G. W. 2000, *AJ*, 120, 3265
- Figueira, P., Adibekyan, V. Z., Oshagh, M., et al. 2016, *A&A*, 586, A101
- Fischer, D. A., Anglada-Escude, G., Arriagada, P., et al. 2016, *PASP*, 128, 066001
- Garcia-Piquer, A., Morales, J. C., Ribas, I., et al. 2017, *A&A*, 604, A87
- Gibson, S. R., Howard, A. W., Marcy, G. W., et al. 2016, in Proc. SPIE, Vol. 9908, Ground-based and Airborne Instrumentation for Astronomy VI, 990870
- Gizis, J. E., Reid, I. N., & Hawley, S. L. 2002, *AJ*, 123, 3356
- Hartman, J. D., Bakos, G. ., Noyes, R. W., et al. 2011, *AJ*, 141, 166
- Hawley, S. L., Gizis, J. E., & Reid, I. N. 1996, *AJ*, 112, 2799
- Herzberg, G. 1950, Molecular spectra and molecular structure. Vol.1: Spectra of diatomic molecules
- Houdebine, E. R. & Mullan, D. J. 2015, *ApJ*, 801, 106
- Husser, T.-O., Wende-von Berg, S., Dreizler, S., et al. 2013, *A&A*, 553, A6
- Irwin, J., Berta, Z. K., Burke, C. J., et al. 2011, *ApJ*, 727, 56
- Jeffers, S. V., Barnes, J. R., Jones, H. R. A., et al. 2014, *MNRAS*, 438, 2717
- Jeffers, S. V., Sch fer, P., Lamert, A., et al. 2017, submitted to *A&A*
- Jurgenson, C., Fischer, D., McCracken, T., et al. 2016, in Proc. SPIE, Vol. 9908, Ground-based and Airborne Instrumentation for Astronomy VI, 990867
- Kiraga, M. 2012, *Acta Astron.*, 62, 67
- Kiraga, M. & Stepi , K. 2013, *Acta Astron.*, 63, 53
- Kiraga, M. & Stepi , K. 2007, *Acta Astron.*, 57, 149
- Kochukhov, O. & Lavail, A. 2017, *ApJ*, 835, L4
- Korhonen, H., Andersen, J. M., Piskunov, N., et al. 2015, *MNRAS*, 448, 3038
- Korhonen, H., Vida, K., Husarik, M., et al. 2010, *Astronomische Nachrichten*, 331, 772
- Kotani, T., Tamura, M., Suto, H., et al. 2014, in Proc. SPIE, Vol. 9147, Ground-based and Airborne Instrumentation for Astronomy V, 914714
- Lagrange, A.-M., Desort, M., & Meunier, N. 2010, *A&A*, 512, A38
- Lanza, A. F., Molaro, P., Monaco, L., & Haywood, R. D. 2016, *A&A*, 587, A103
- Lebzelter, T., Seifahrt, A., Uttenthaler, S., et al. 2012, *A&A*, 539, A109
- L pine, S., Hilton, E. J., Mann, A. W., et al. 2013, *AJ*, 145, 102
- Mahadevan, S., Ramsey, L. W., Terrien, R., et al. 2014, in Proc. SPIE, Vol. 9147, Ground-based and Airborne Instrumentation for Astronomy V, 91471G
- Marchwinski, R. C., Mahadevan, S., Robertson, P., Ramsey, L., & Harder, J. 2015, *ApJ*, 798, 63
- Martn, E. L., Guenther, E., Barrado y Navascu s, D., et al. 2005, *Astronomische Nachrichten*, 326, 1015
- Martn, E. L., Guenther, E., Zapatero Osorio, M. R., Bouy, H., & Wainscoat, R. 2006, *ApJ*, 644, L75
- Mayor, M., Bonfils, X., Forveille, T., et al. 2009a, *A&A*, 507, 487
- Mayor, M., Udry, S., Lovis, C., et al. 2009b, *A&A*, 493, 639
- Merline, W. J. 1985, in *Stellar Radial Velocities*, ed. A. G. D. Philip & D. W. Latham, Vol. 88, 87
- Meunier, N., Desort, M., & Lagrange, A.-M. 2010a, *A&A*, 512, A39
- Meunier, N., Lagrange, A.-M., & Desort, M. 2010b, *A&A*, 519, A66
- Newton, E. R., Irwin, J., Charbonneau, D., et al. 2016, *ApJ*, 821, 93
- Norton, A. J., Wheatley, P. J., West, R. G., et al. 2007, *A&A*, 467, 785
- Oliva, E., Origlia, L., Scuderi, S., et al. 2015, *A&A*, 581, A47
- Pepe, F. A., Cristiani, S., Rebolo Lopez, R., et al. 2010, in Proc. SPIE, Vol. 7735, Ground-based and Airborne Instrumentation for Astronomy III, 77350F
- Plavchan, P., Latham, D., Gaudi, S., et al. 2015, ArXiv e-prints [arXiv:1503.01770]
- Quirrenbach, A., Amado, P. J., Caballero, J. A., et al. 2016, in Proc. SPIE, Vol. 9908, Ground-based and Airborne Instrumentation for Astronomy VI, 990812
- Reid, I. N., Hawley, S. L., & Gizis, J. E. 1995, *AJ*, 110, 1838
- Reiners, A. 2007, *A&A*, 467, 259
- Reiners, A. & Basri, G. 2006, *ApJ*, 644, 497
- Reiners, A. & Basri, G. 2008, *ApJ*, 684, 1390
- Reiners, A., Bean, J. L., Huber, K. F., et al. 2010, *ApJ*, 710, 432
- Reiners, A., Homeier, D., Hauschildt, P. H., & Allard, F. 2007, *A&A*, 473, 245
- Reiners, A., Joshi, N., & Goldman, B. 2012, *AJ*, 143, 93
- Reiners, A., Shulyak, D., Anglada-Escud, G., et al. 2013, *A&A*, 552, A103
- Rivera, E. J., Lissauer, J. J., Butler, R. P., et al. 2005, *ApJ*, 634, 625
- Rodler, F., Del Burgo, C., Witte, S., et al. 2011, *A&A*, 532, A31
- Ryabchikova, T., Piskunov, N., Kurucz, R. L., et al. 2015, *Phys. Scr.*, 90, 054005
- Saar, S. H. & Donahue, R. A. 1997, *ApJ*, 485, 319
- Scalo, J., Kaltenegger, L., Segura, A. G., et al. 2007, *Astrobiology*, 7, 85
- Seifahrt, A., Bean, J. L., St rmer, J., et al. 2016, in Proc. SPIE, Vol. 9908, Ground-based and Airborne Instrumentation for Astronomy VI, 990818
- Shulyak, D., Reiners, A., Engeln, A., et al. 2017, *Nature Astronomy*, 1, 0184
- Shulyak, D., Seifahrt, A., Reiners, A., Kochukhov, O., & Piskunov, N. 2011, *MNRAS*, 418, 2548
- Skrutskie, M. F., Cutri, R. M., Stiening, R., et al. 2006, *AJ*, 131, 1163
- Soubiran, C., Jasniewicz, G., Chemin, L., et al. 2013, *A&A*, 552, A64
- Surez Mascare o, A., Rebolo, R., & Gonzlez Hernndez, J. I. 2016, *A&A*, 595, A12
- Surez Mascare o, A., Rebolo, R., Gonzlez Hernndez, J. I., & Esposito, M. 2015, *MNRAS*, 452, 2745
- Tarter, J. C., Backus, P. R., Mancinelli, R. L., et al. 2007, *Astrobiology*, 7, 30
- Testa, P., Drake, J. J., & Peres, G. 2004, *ApJ*, 617, 508
- Tinney, C. G. & Reid, I. N. 1998, *MNRAS*, 301, 1031
- Trifonov, T., K rster, M., Zechmeister, M., et al. 2017, ArXiv e-prints [arXiv:1710.01595]
- Udry, S. & Santos, N. C. 2007, *ARA&A*, 45, 397
- Wang, J. & Ford, E. B. 2011, *MNRAS*, 418, 1822
- West, A. A., Weisenburger, K. L., Irwin, J., et al. 2015, *ApJ*, 812, 3
- Zechmeister, M., Anglada-Escud, G., & Reiners, A. 2014, *A&A*, 561, A59
- Zechmeister, M., Reiners, A., Amado, P. J., et al. 2017, ArXiv e-prints [arXiv:1710.10114]

- ¹ Institut für Astrophysik, Georg-August-Universität, Friedrich-Hund-Platz 1, D-37077 Göttingen, Germany
e-mail: Ansgar.Reiners@phys.uni-goettingen.de
- ² Centro de Astrobiología (CSIC-INTA), Instituto Nacional de Técnica Aeroespacial, Ctra. de Torrejón a Ajalvir, km 4, E-28850 Torrejón de Ardoz, Madrid, Spain
- ³ Zentrum für Astronomie der Universität Heidelberg, Landessternwarte, Königstuhl 12, D-69117 Heidelberg, Germany
- ⁴ Institut de Ciències de l'Espai (CSIC-IEEC), Campus UAB, c/ de Can Magrans s/n, E-08193 Bellaterra, Barcelona, Spain
- ⁵ Instituto de Astrofísica de Andalucía (IAA-CSIC), Glorieta de la Astronomía s/n, E-18008 Granada, Spain
- ⁶ Centro Astronómico Hispano-Alemán (CSIC-MPG), Observatorio Astronómico de Calar Alto, Sierra de los Filabres, E-04550 Gérgal, Almería, Spain
- ⁷ Max-Planck-Institut für Astronomie, Königstuhl 17, D-69117 Heidelberg, Germany
- ⁸ Departamento de Astrofísica y Ciencias de la Atmósfera, Facultad de Ciencias Físicas, Universidad Complutense de Madrid, E-28040 Madrid, Spain
- ⁹ Instituto de Astrofísica de Canarias, Vía Láctea s/n, 38205 La Laguna, Tenerife, Spain, and Departamento de Astrofísica, Universidad de La Laguna, E-38206 La Laguna, Tenerife, Spain
- ¹⁰ Hamburger Sternwarte, Gojenbergsweg 112, D-21029 Hamburg, Germany
- ¹¹ Thüringer Landessternwarte Tautenburg, Sternwarte 5, D-07778 Tautenburg, Germany
- ¹² Leiden Observatory, Leiden University, Postbus 9513, 2300 RA, Leiden, The Netherlands
- ¹³ Max-Planck-Institut für Sonnensystemforschung, Justus-von-Liebig-Weg 3, D-37077 Göttingen, Germany
- ¹⁴ School of Physics and Astronomy, Queen Mary, University of London, 327 Mile End Road, London, E1 4NS
- ¹⁵ Instituto Nacional de Astrofísica, Óptica y Electrónica, Luis Enrique Erro 1, Sta. Ma. Tonantzintla, Puebla, Mexico
- ¹⁶ FRACTAL SLNE. C/ Tulipán 2, P13-1A, E-28231 Las Rozas de Madrid, Spain
- ¹⁷ Institut für Theoretische Physik und Astrophysik, Leibnizstraße 15, D-24118 Kiel, Germany
- ¹⁸ Osservatorio Astrofisico di Catania, Via S. Sofia 78, 95123 Catania, Italy
- ¹⁹ Dipartimento di Fisica, Università di Roma, "Tor Vergata", Via della Ricerca Scientifica, 1 - 00133 Roma, Italy
- ²⁰ Weizmann Institute of Science, 234 Herzl Street, Rehovot 761001, Israel
- ²¹ University College Dublin, School of Physics, Belfield, Dublin 4, Ireland
- ²² European Southern Observatory, Alonso de Córdova 3107, Vitacura, Casilla 19001, Santiago de Chile, Chile
- ²³ The Department of Astronomy and Astrophysics, University of Chicago, 5640 S. Ellis Ave, Chicago, IL 60637, USA
- ²⁴ Universidad de Granada, Av. del Hospicio, s/n, E-18010 Granada, Spain
- ²⁵ QUCAM Astronomical Detectors, <http://www.qucam.com/>
- ²⁶ European Southern Observatory, Karl-Schwarzschild-Str. 2, D-85748 Garching bei München
- ²⁷ Dpto. de Teoría de la Señal y Comunicaciones, Universidad Carlos III de Madrid, Escuela Politécnica Superior, Avda. de la Universidad, 30. E-28911 Leganés, Madrid, Spain
- ²⁸ Dpto. de Física, Ingeniería de Sistemas y Teoría de la Señal, Escuela Politécnica Superior, Universidad de Alicante, Apdo.99, E-03080, Alicante, Spain
- ²⁹ INAF, Osservatorio Astrofisico di Torino, via Osservatorio 20, 10025, Pino Torinese, Italy

Appendix A: Atlas of near-infrared spectra

In Figs. A.1 – A.40 we plot spectra of a telluric standard star and three survey targets in black and the synthetic model spectra in red. See Section 3 for details.

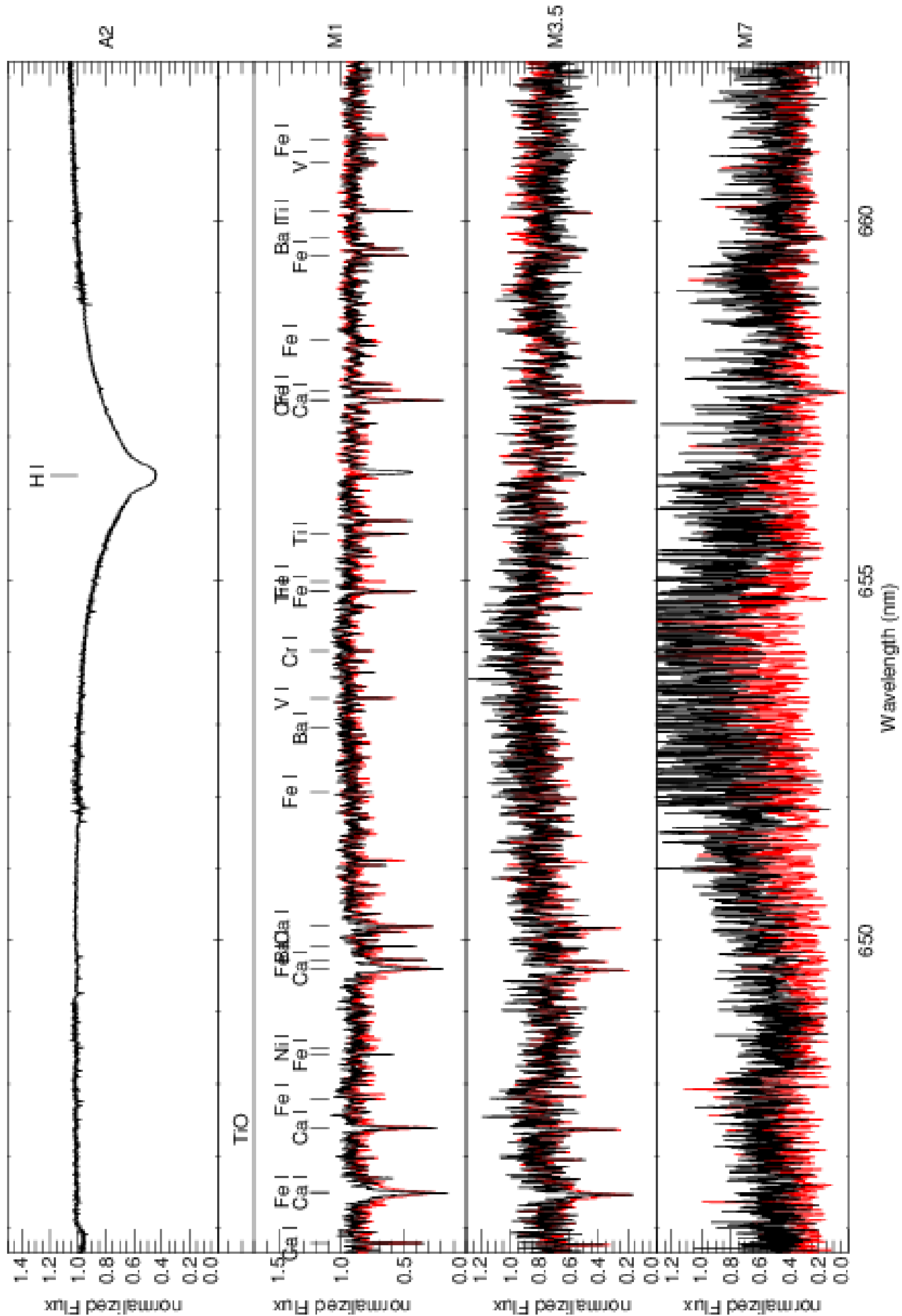


Fig. A.1. CARMENES spectral atlas.

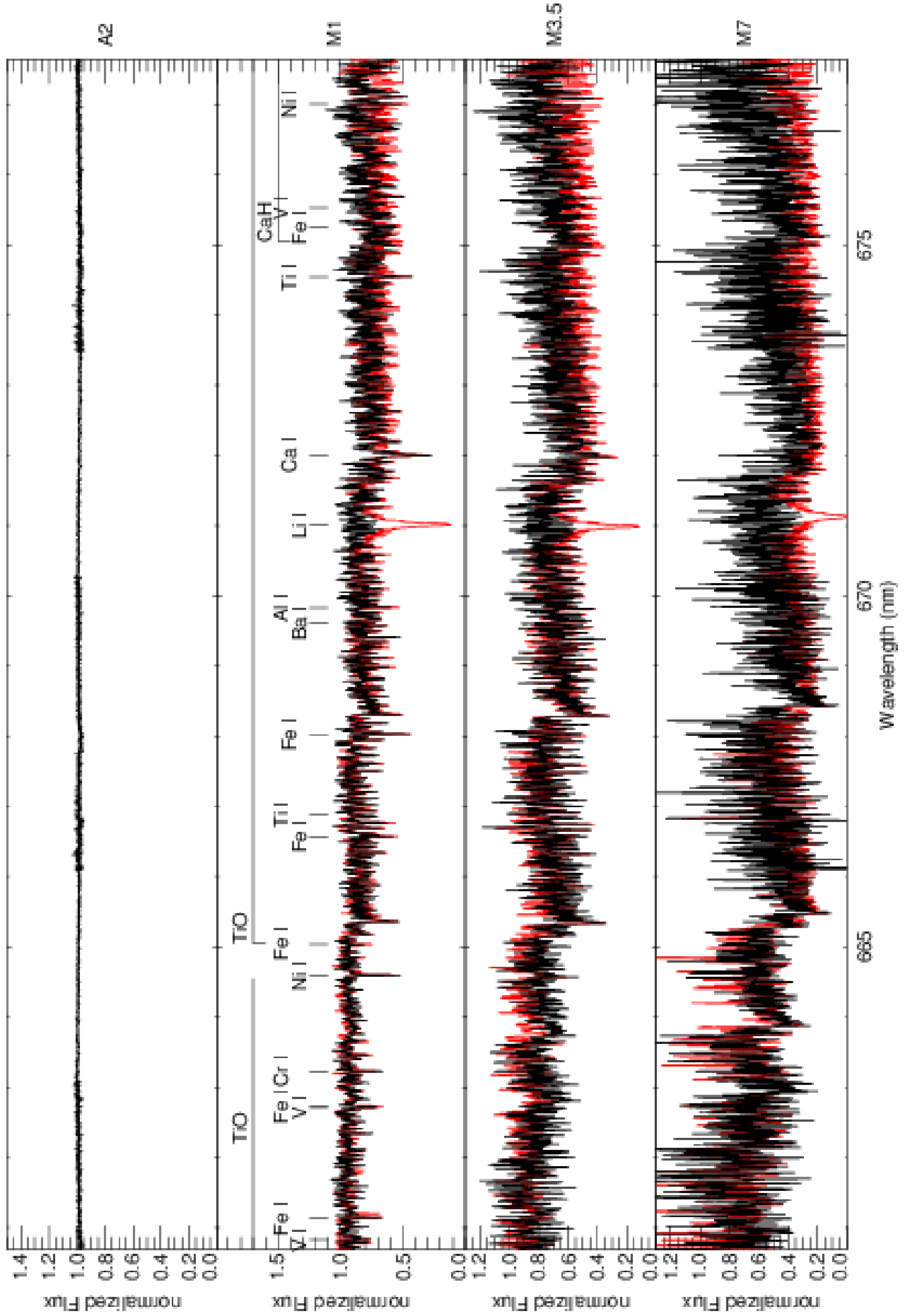


Fig. A.2. CARMENES spectral atlas.
Article number, page 16 of 63

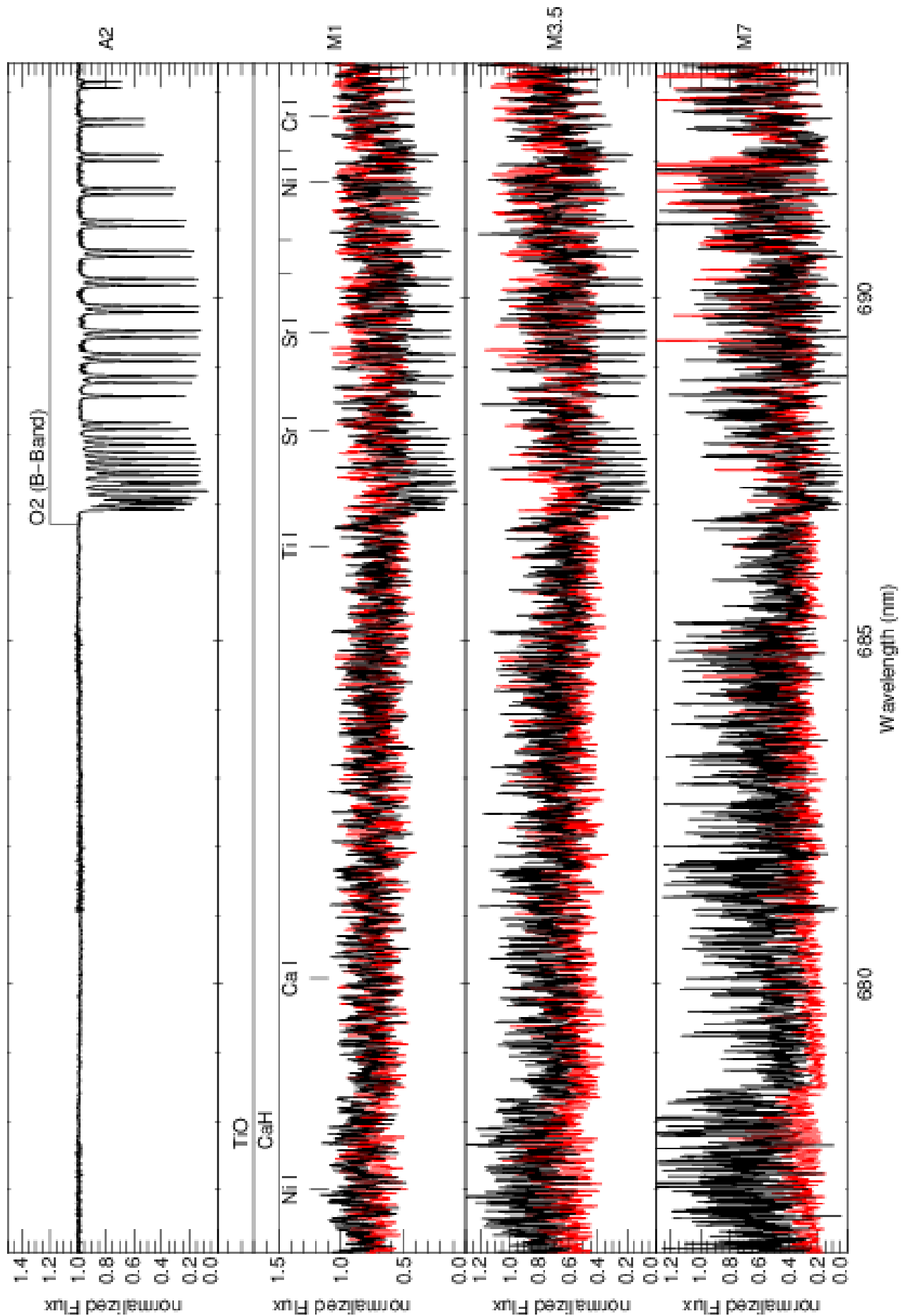


Fig. A.3. CARMENES spectral atlas.

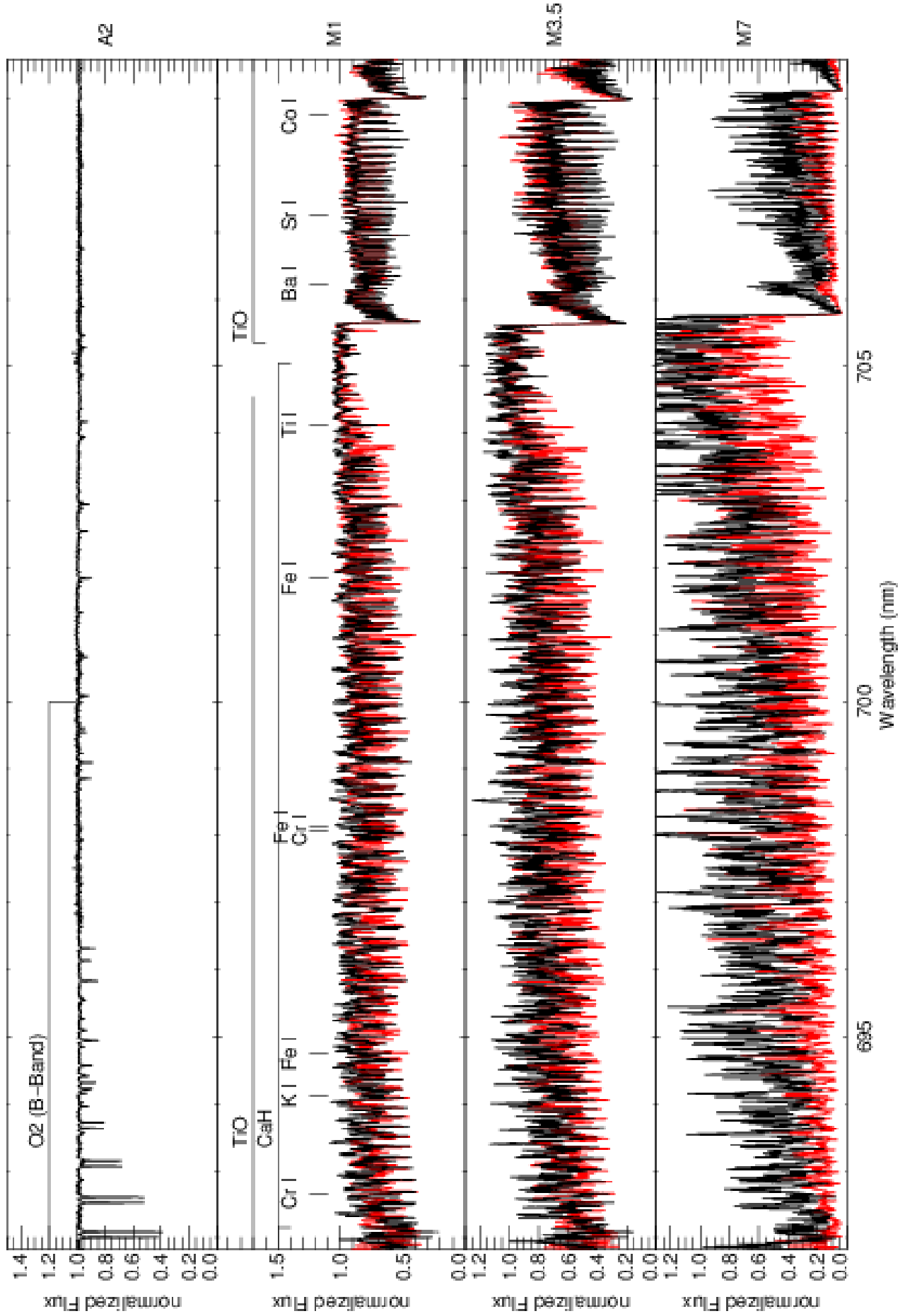


Fig. A.4. CARMENES spectral atlas.
Article number, page 18 of 63

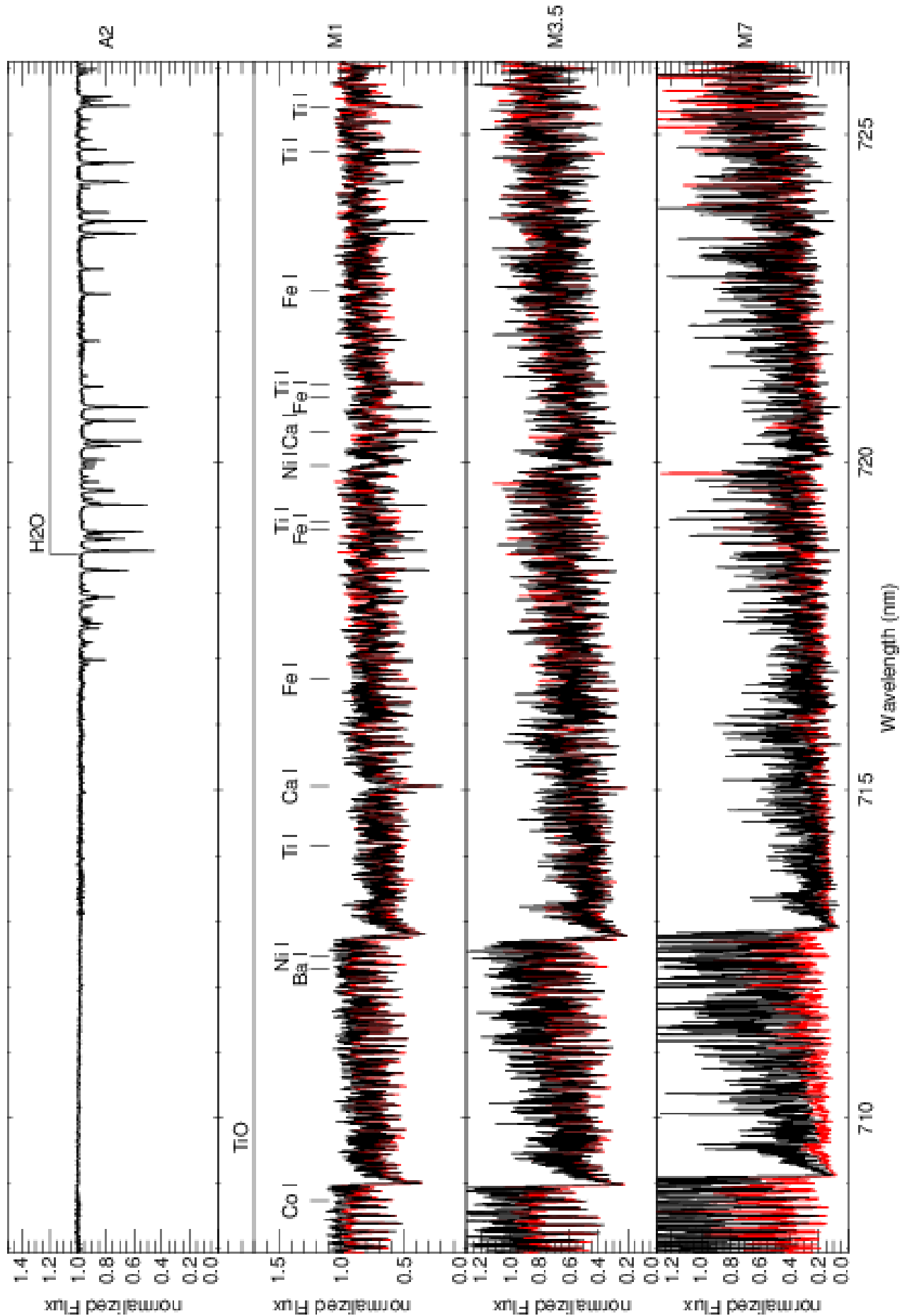


Fig. A.5. CARMENES spectral atlas.

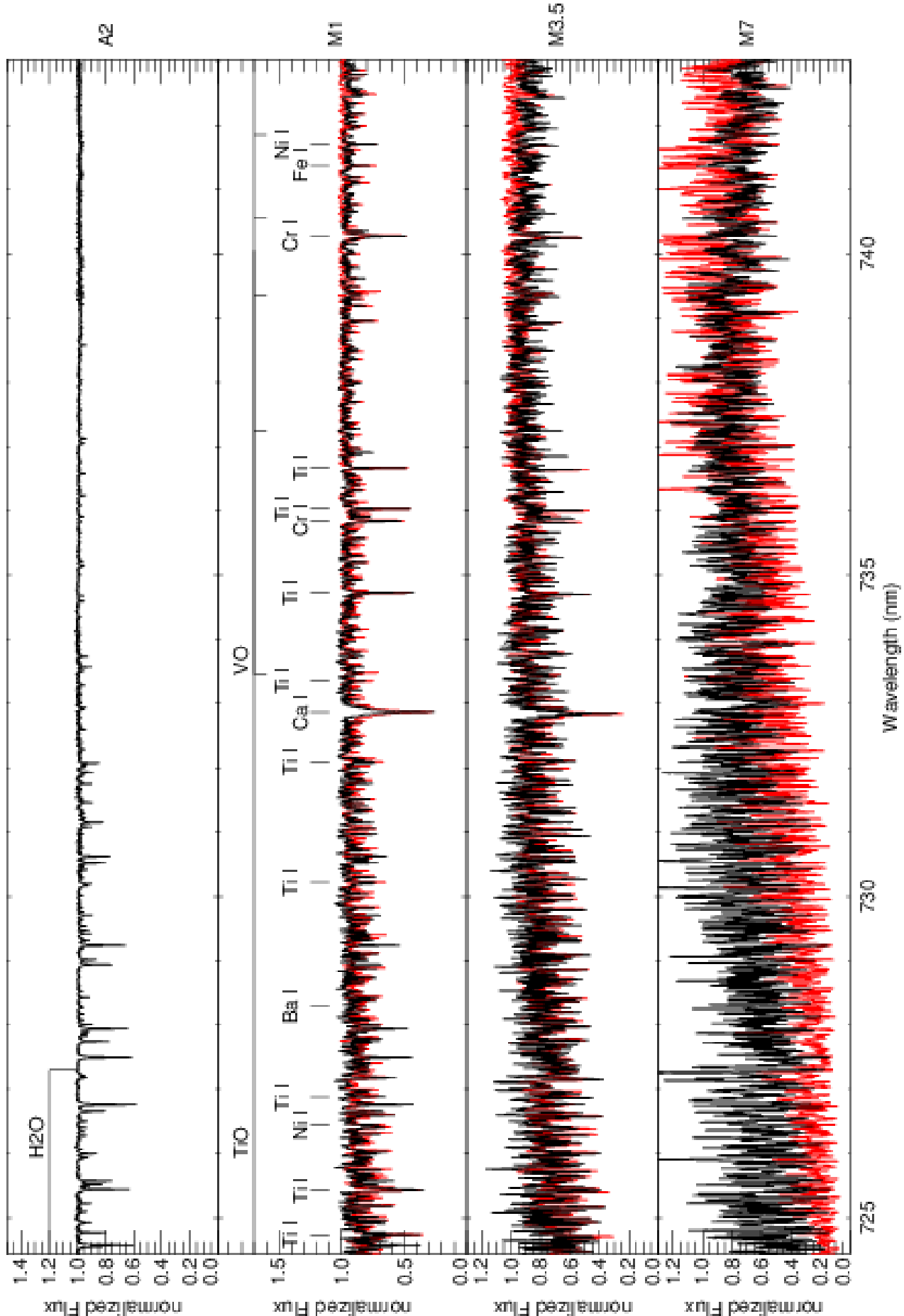


Fig. A.6. CARMENES spectral atlas.
Article number, page 20 of 63

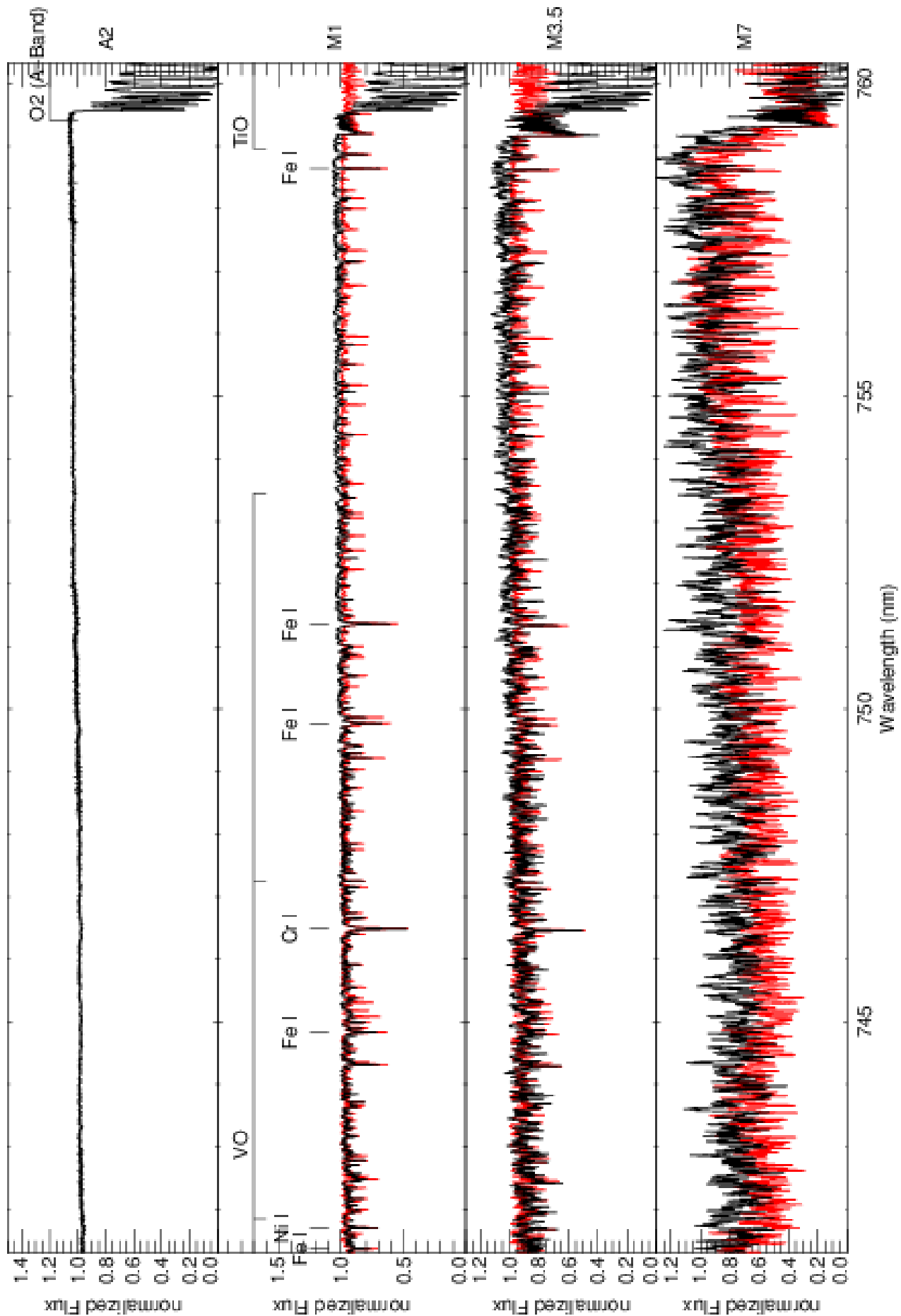


Fig. A.7. CARMENES spectral atlas.

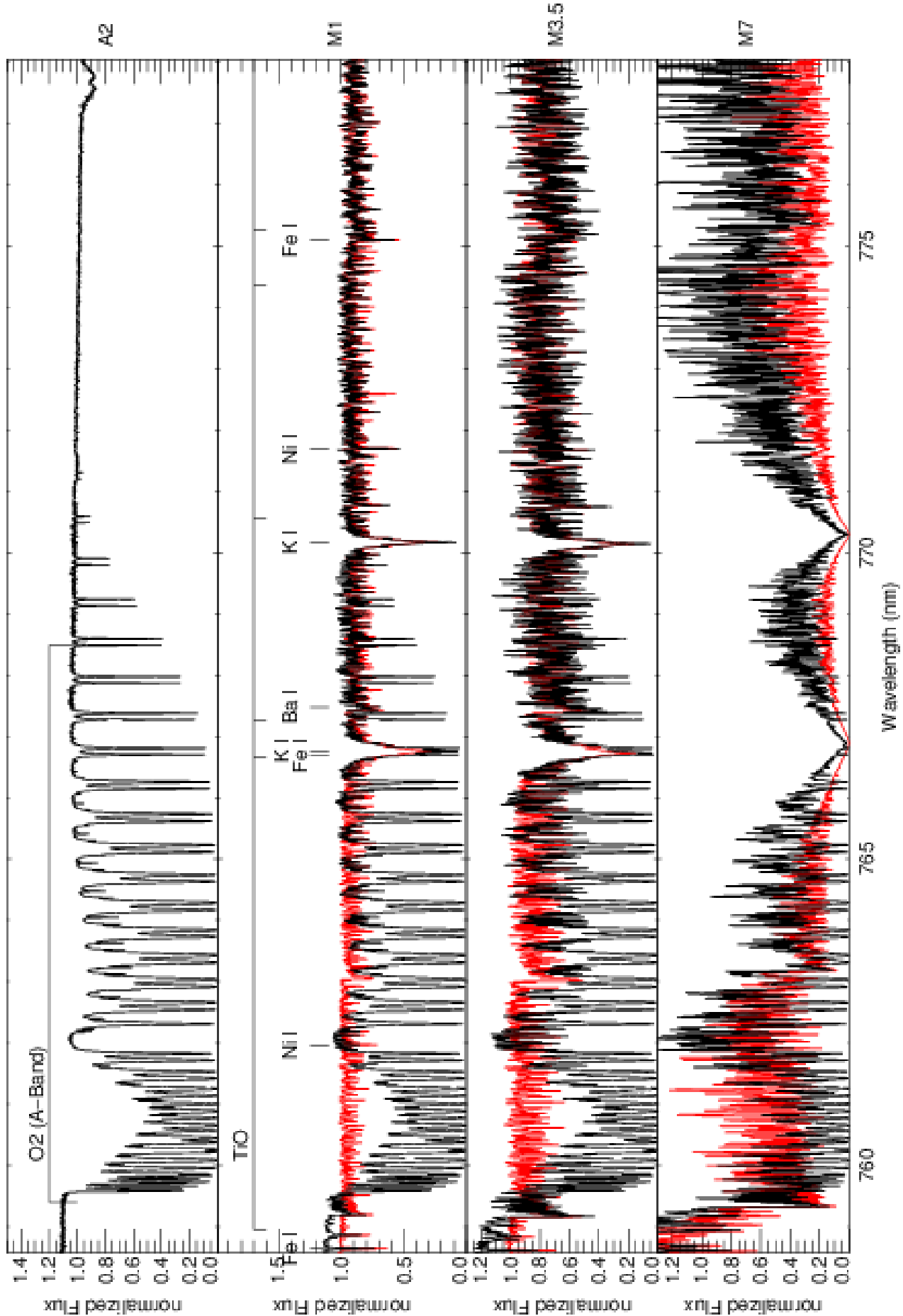


Fig. A.8. CARMENES spectral atlas.
Article number, page 22 of 63

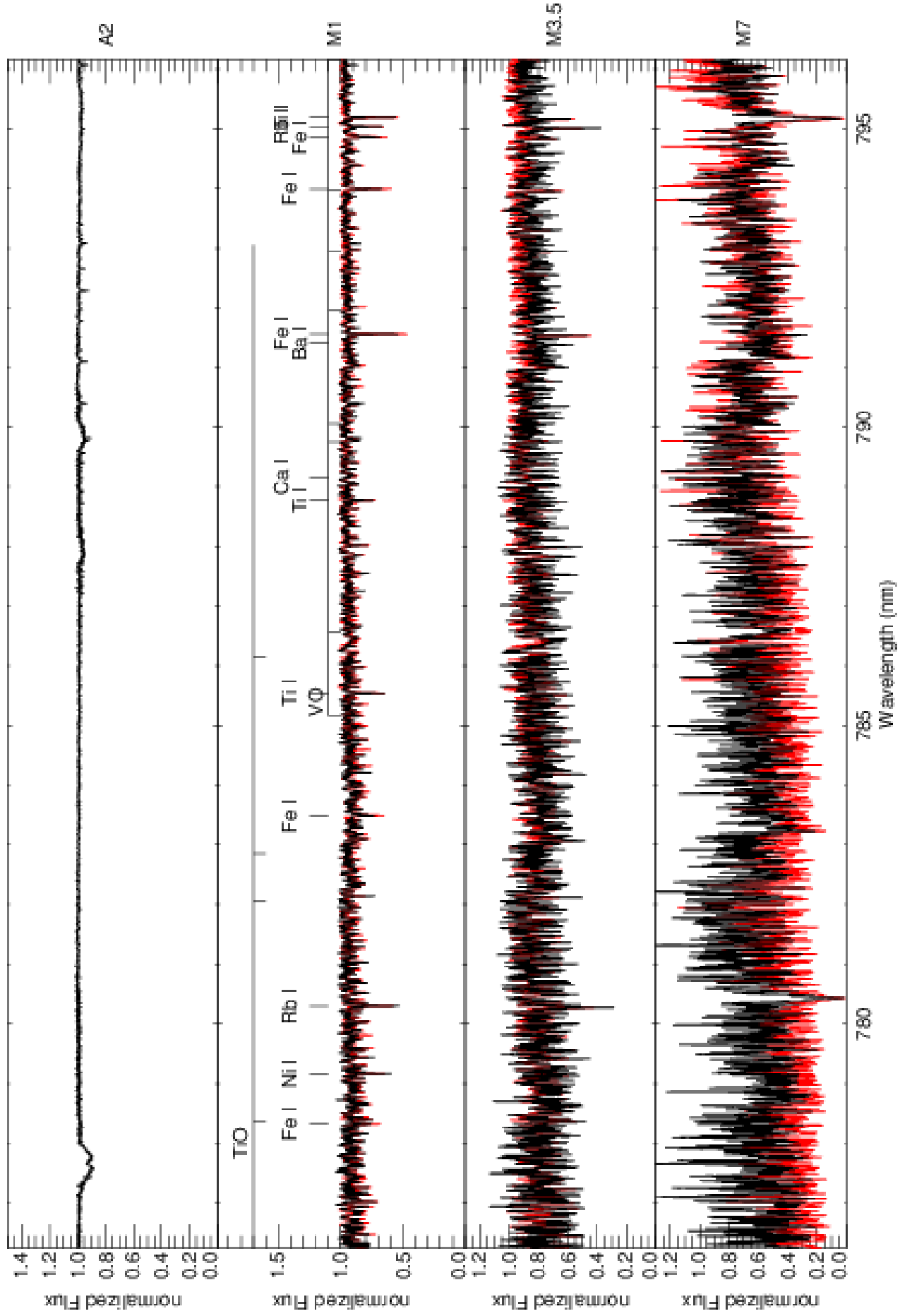


Fig. A.9. CARMENES spectral atlas.

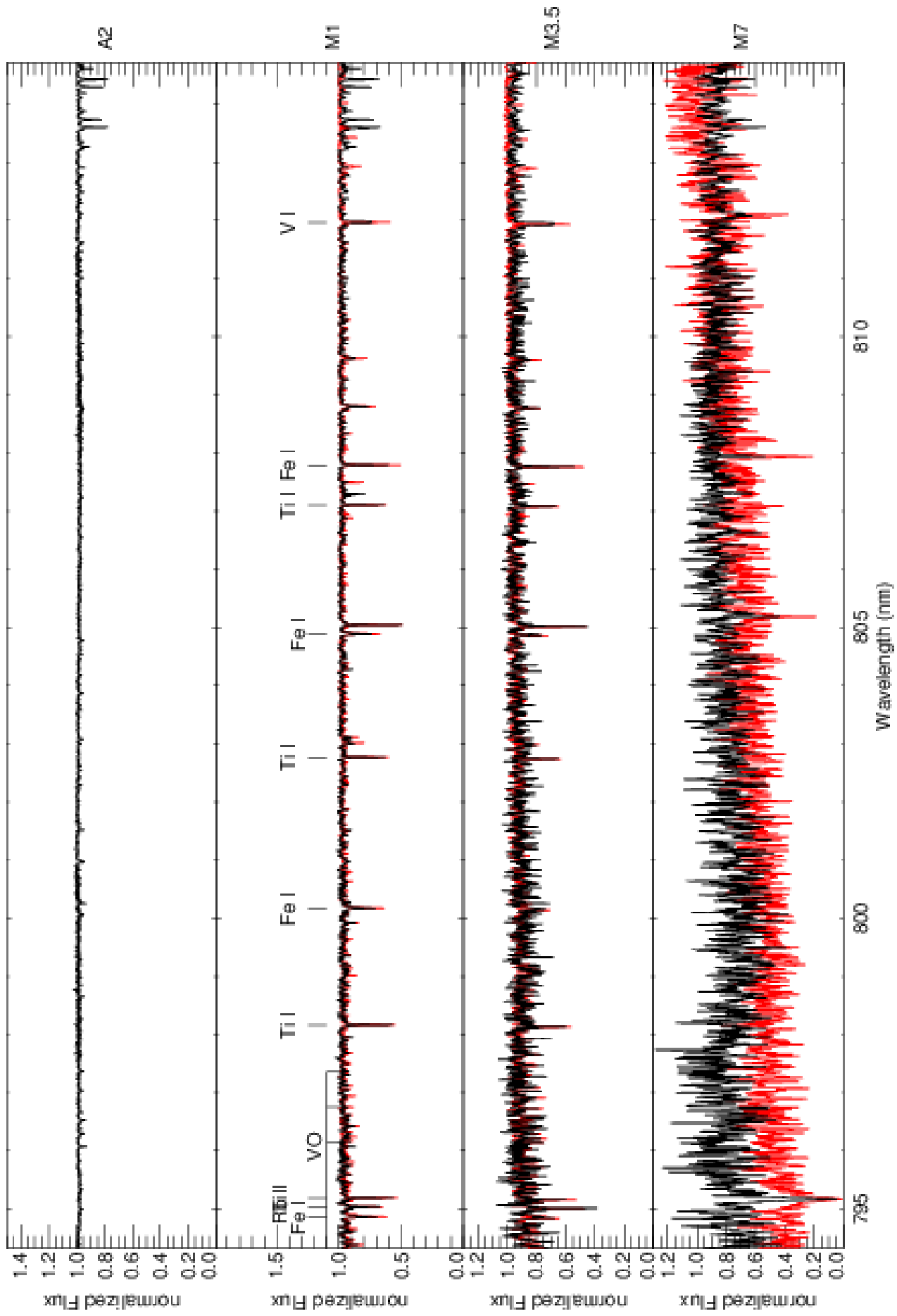


Fig. A.10. CARMENES spectral atlas.
Article number, page 24 of 63

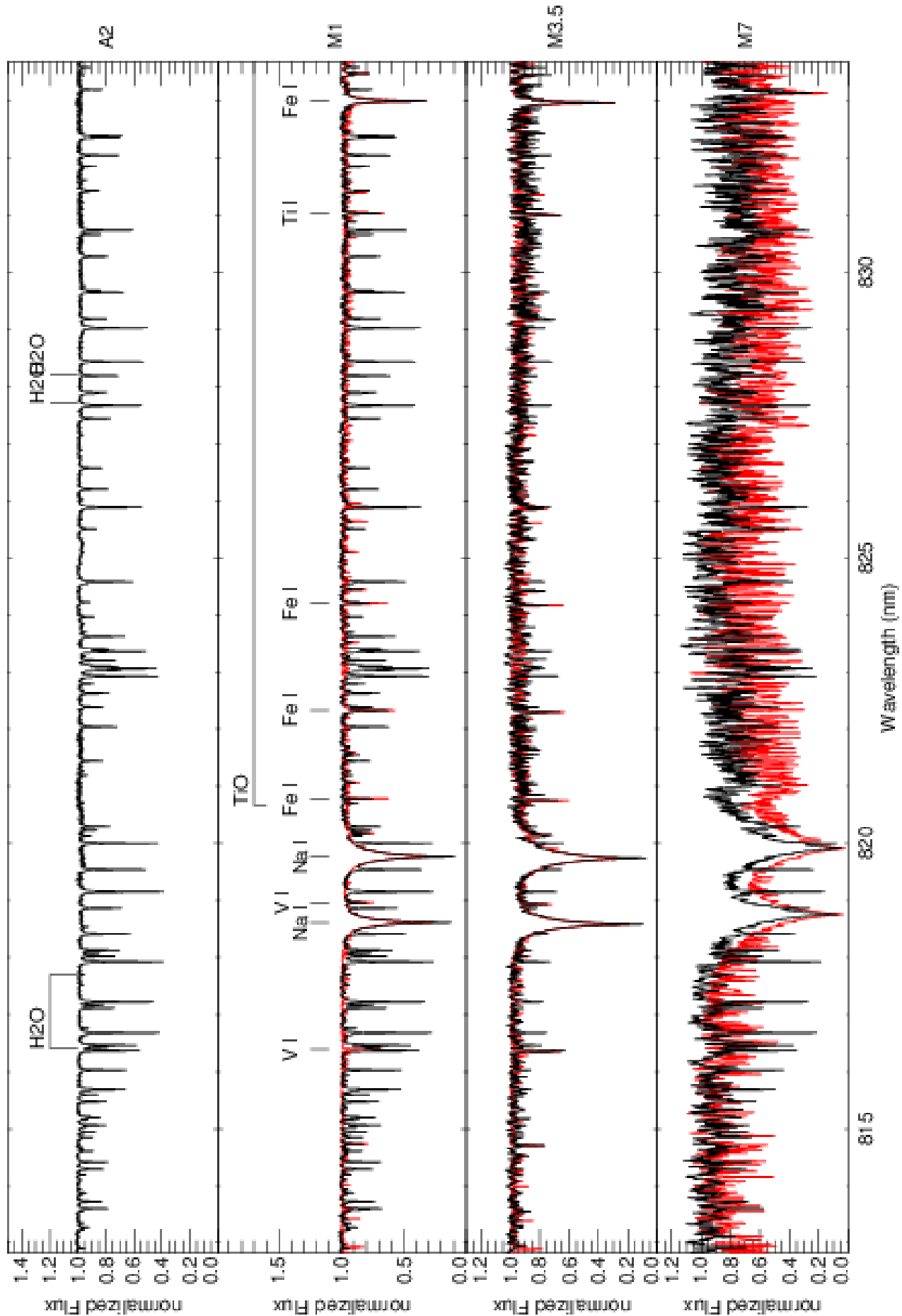


Fig. A.11. CARMENES spectral atlas.

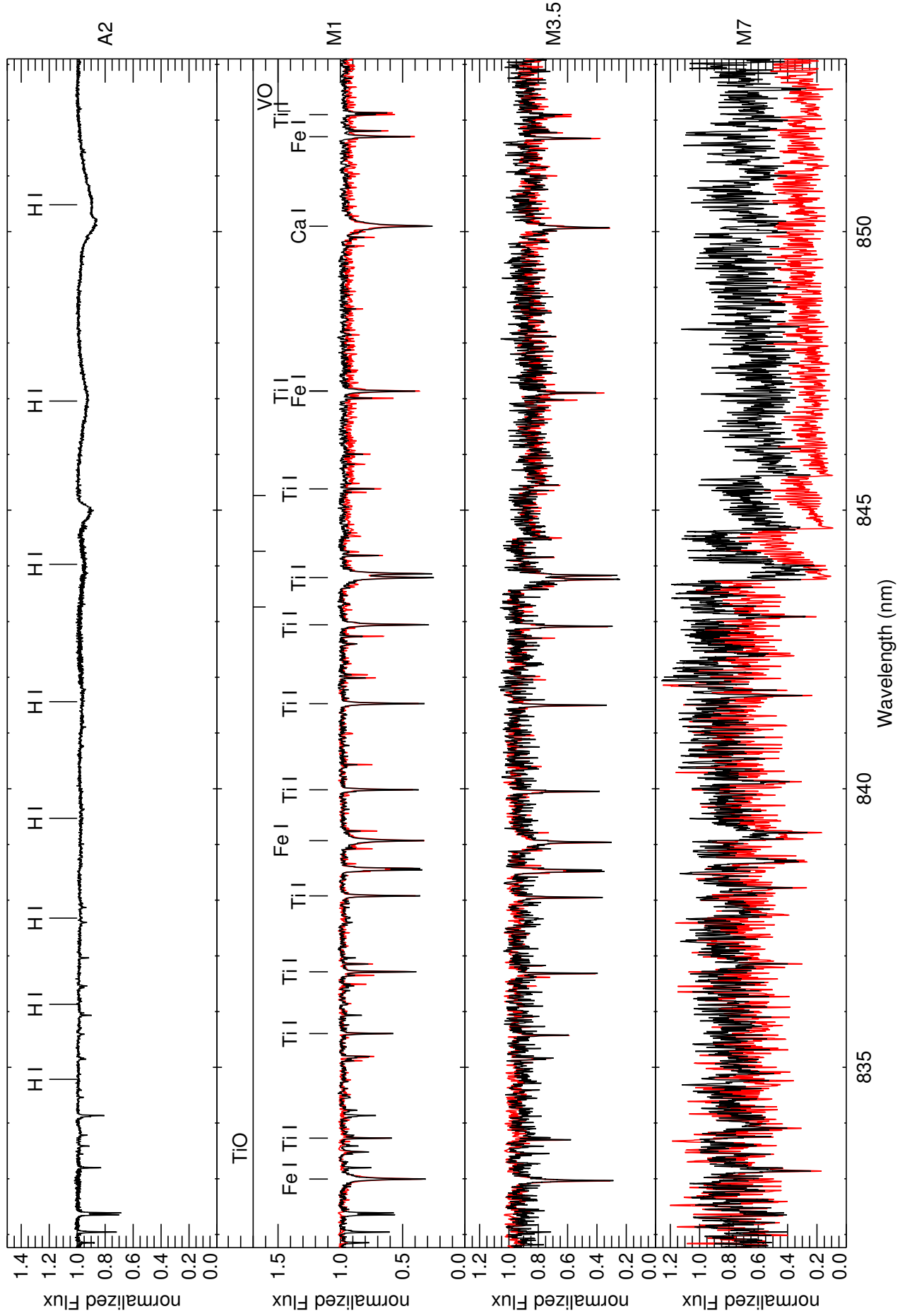


Fig. A.12. CARMENES spectral atlas.
Article number, page 26 of 63

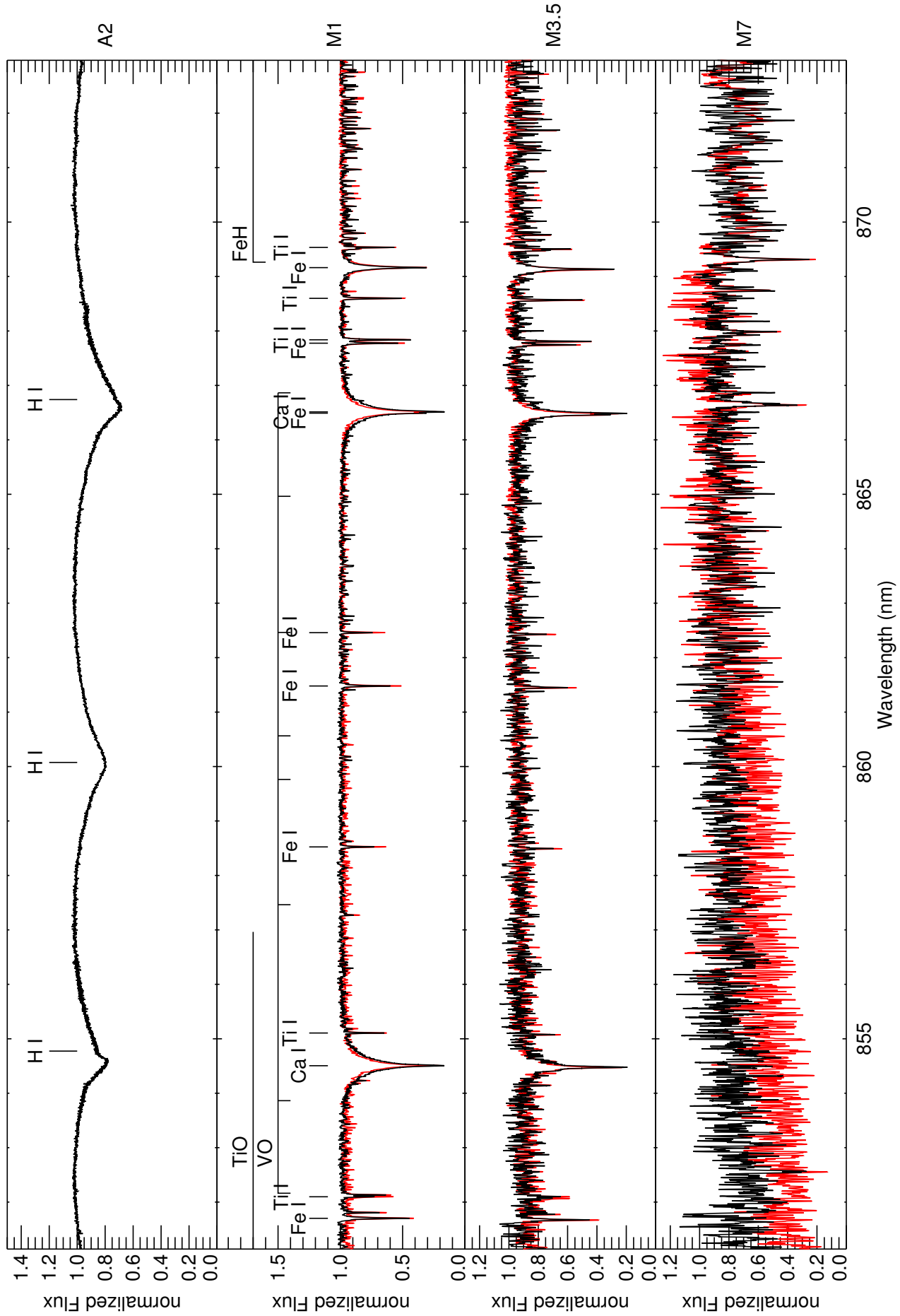


Fig. A.13. CARMENES spectral atlas.

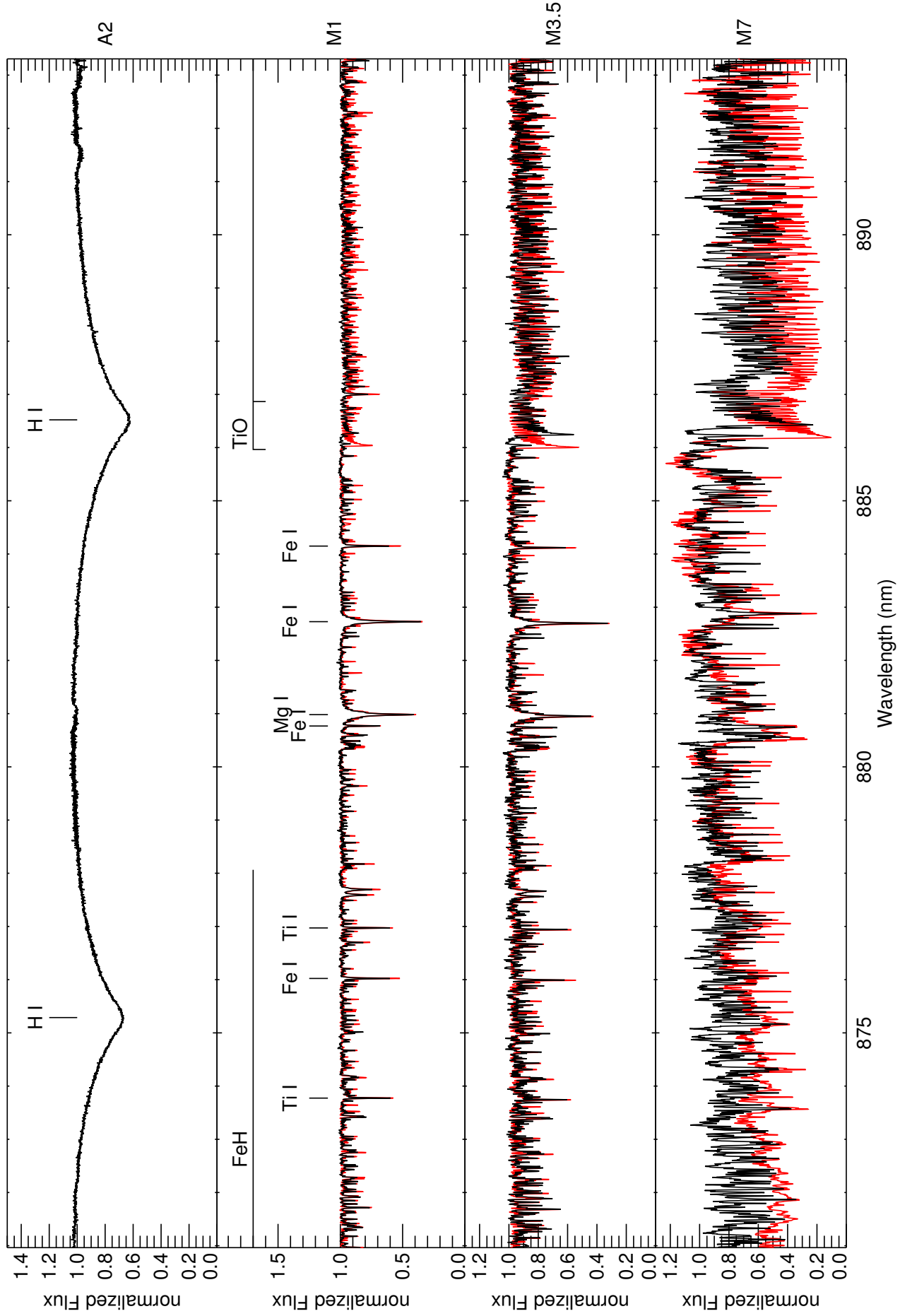


Fig. A.14. CARMENES spectral atlas.
Article number, page 28 of 63

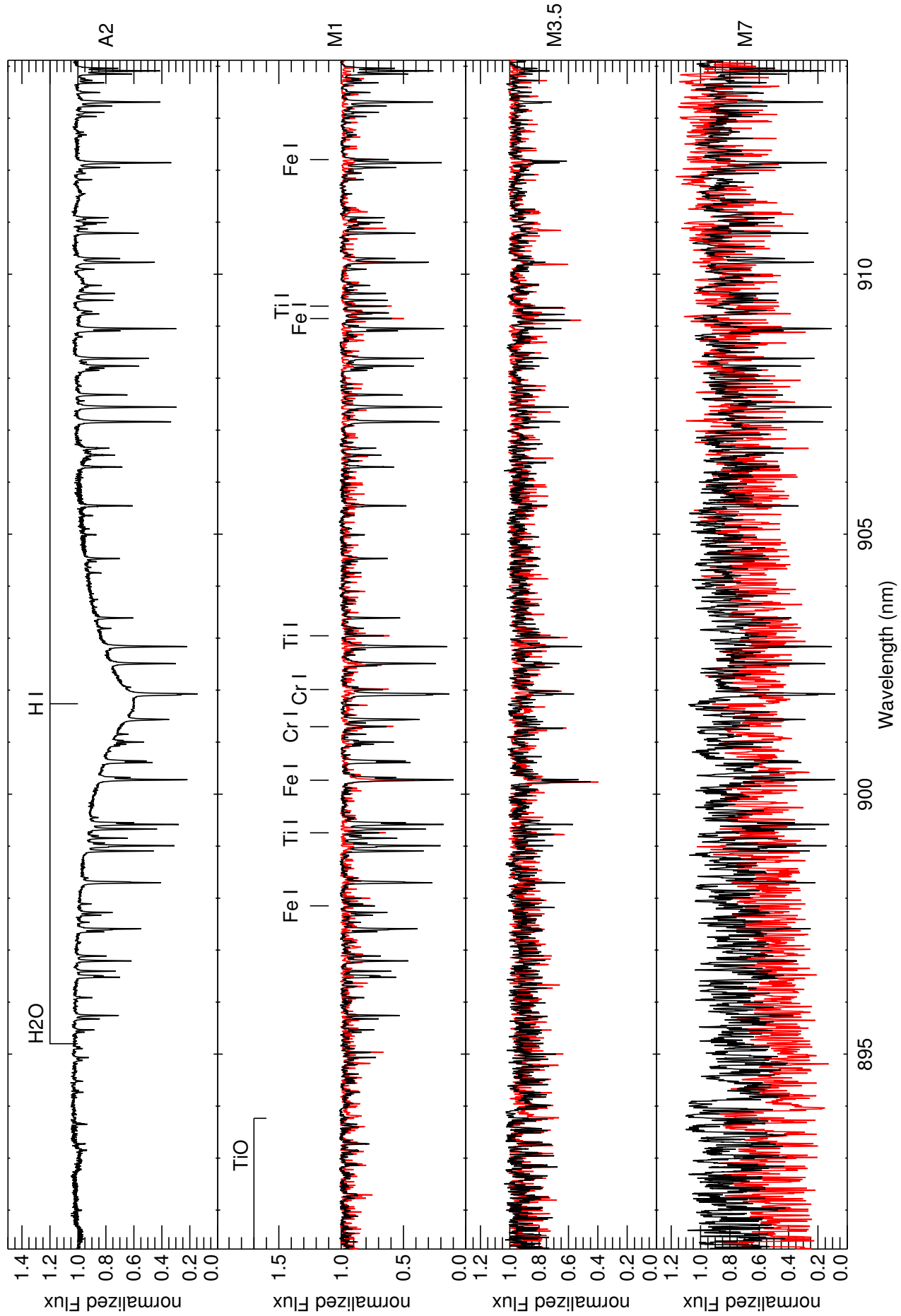


Fig. A.15. CARMENES spectral atlas.

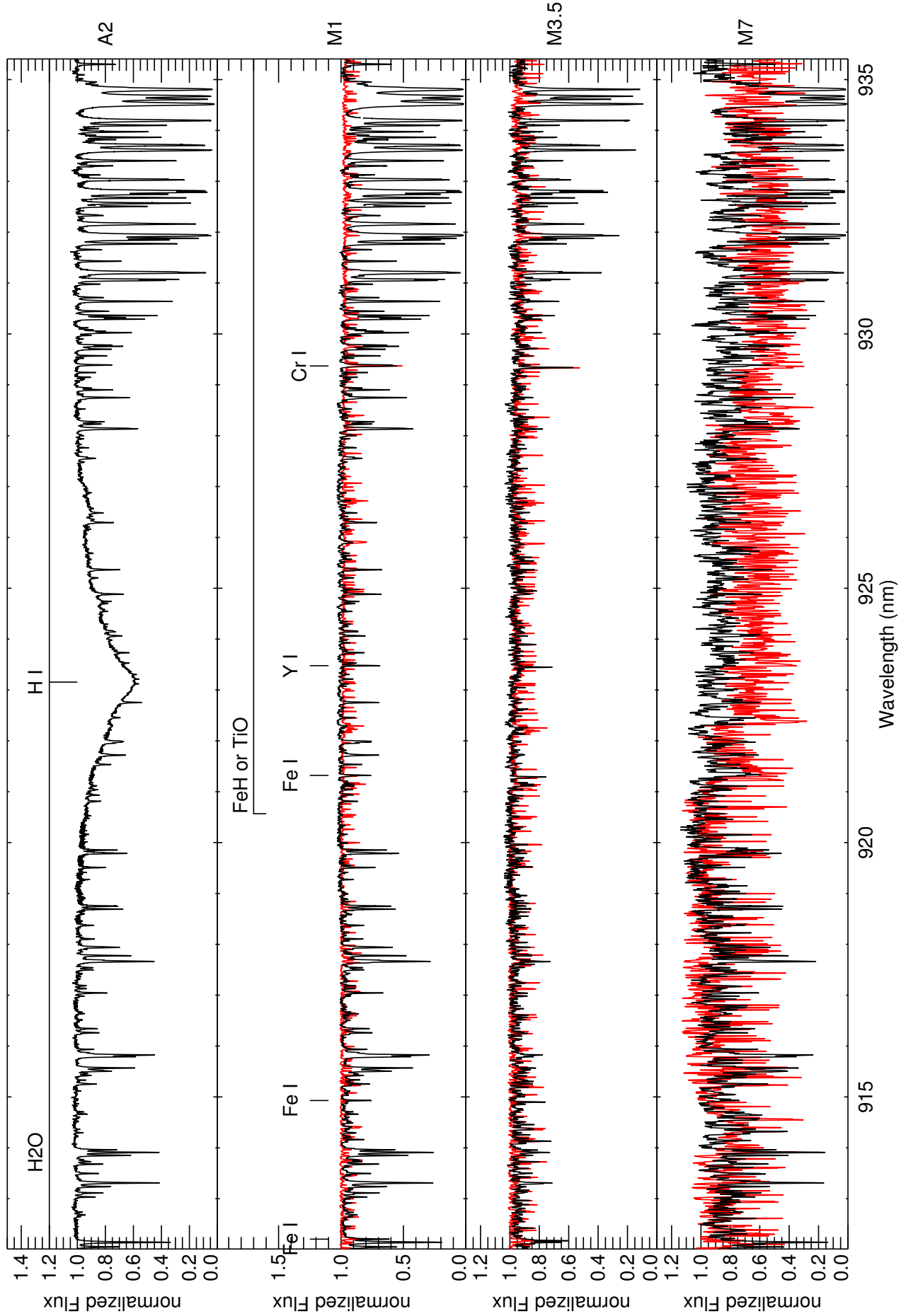


Fig. A.16. CARMENES spectral atlas.
Article number, page 30 of 63

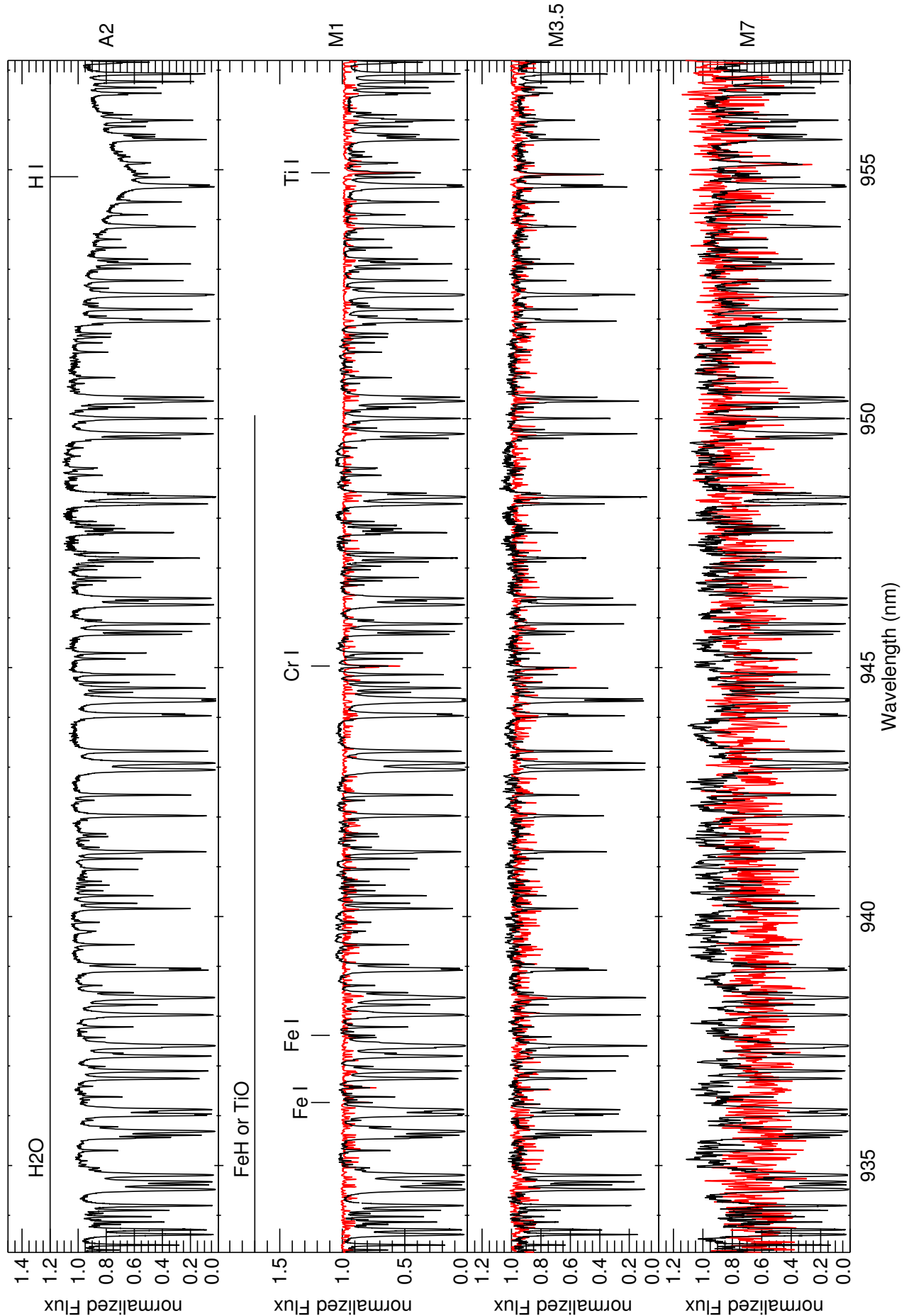


Fig. A.17. CARMENES spectral atlas.

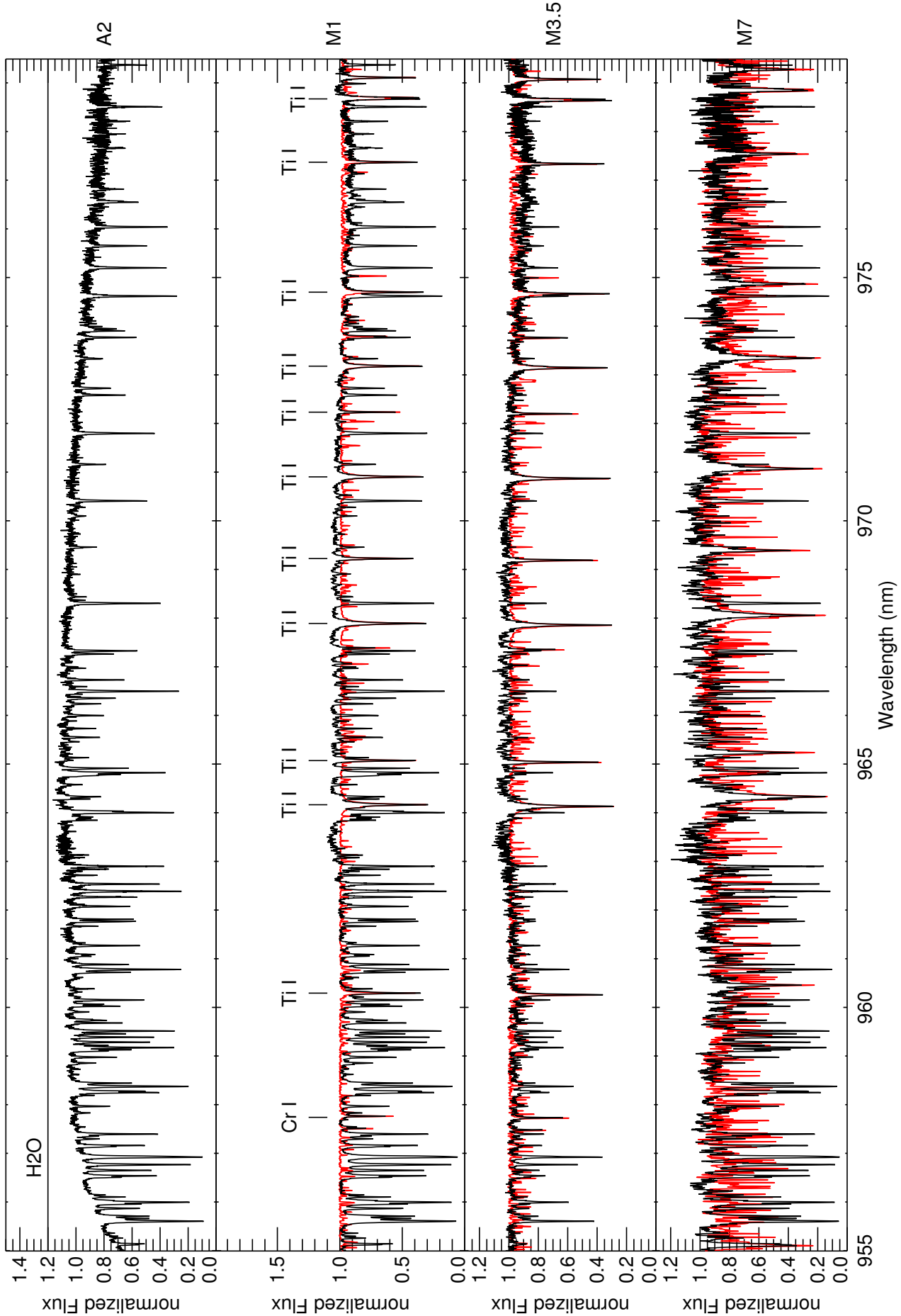


Fig. A.18. CARMENES spectral atlas.
Article number, page 32 of 63

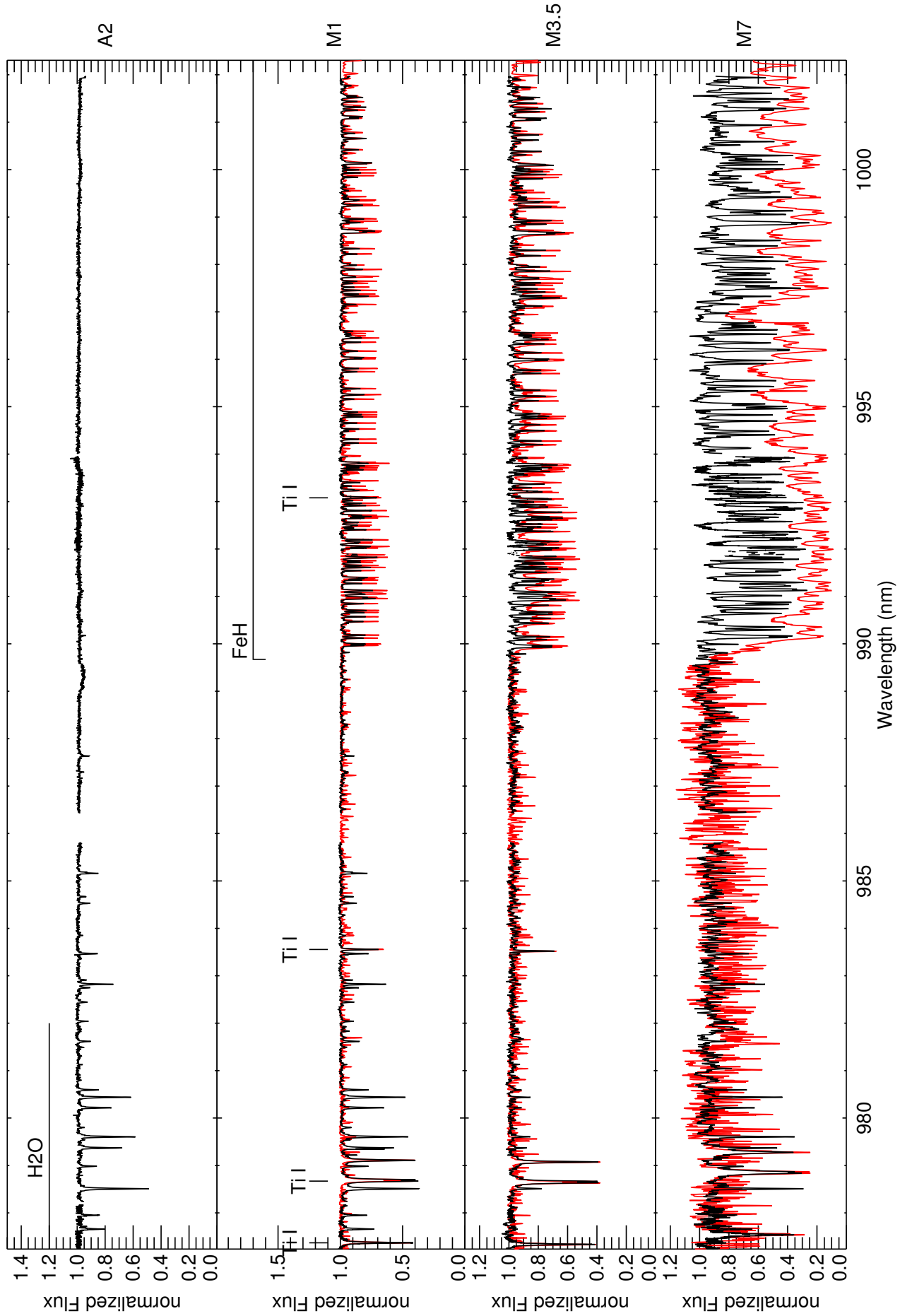


Fig. A.19. CARMENES spectral atlas.

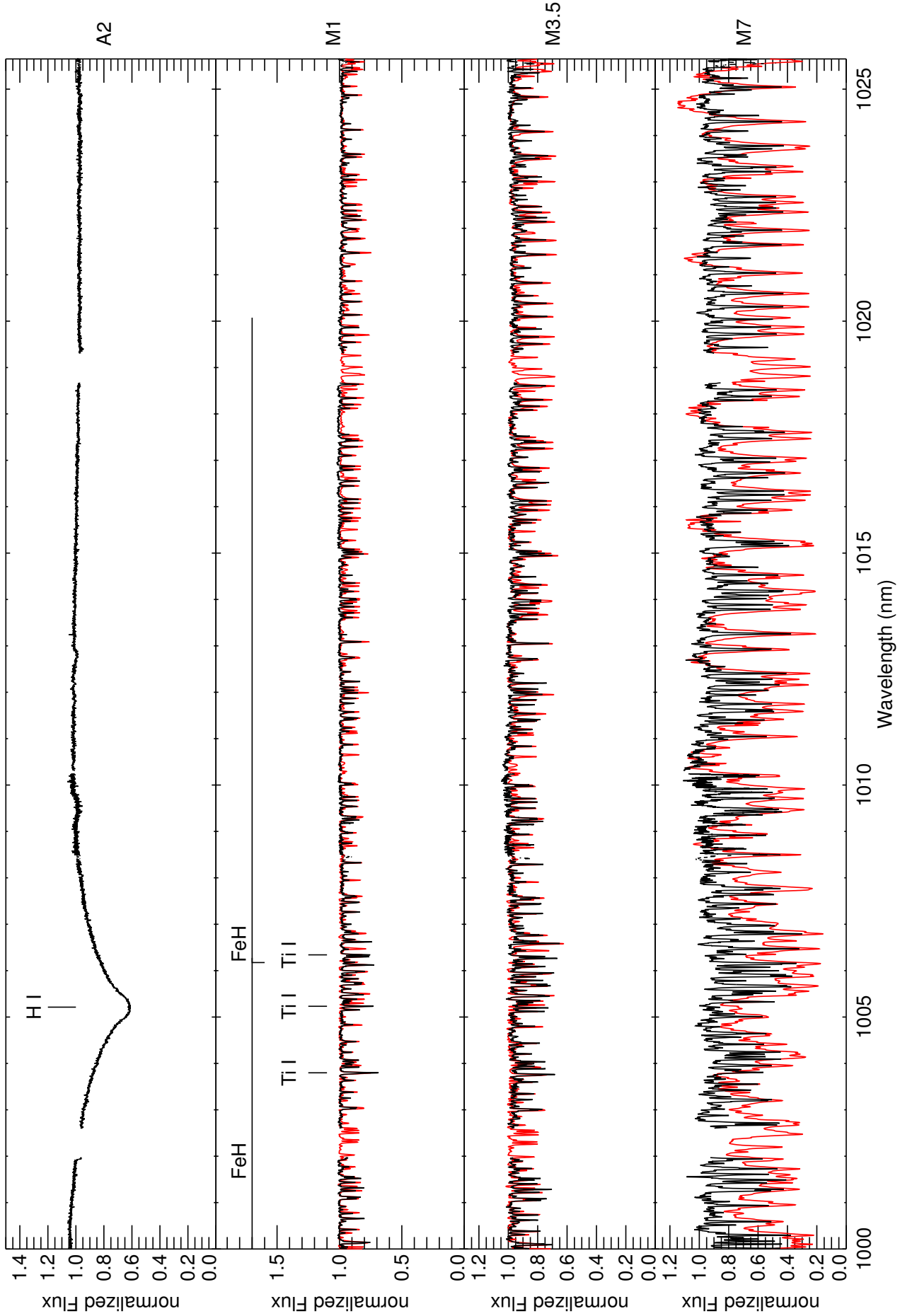


Fig. A.20. CARMENES spectral atlas.
Article number, page 34 of 63

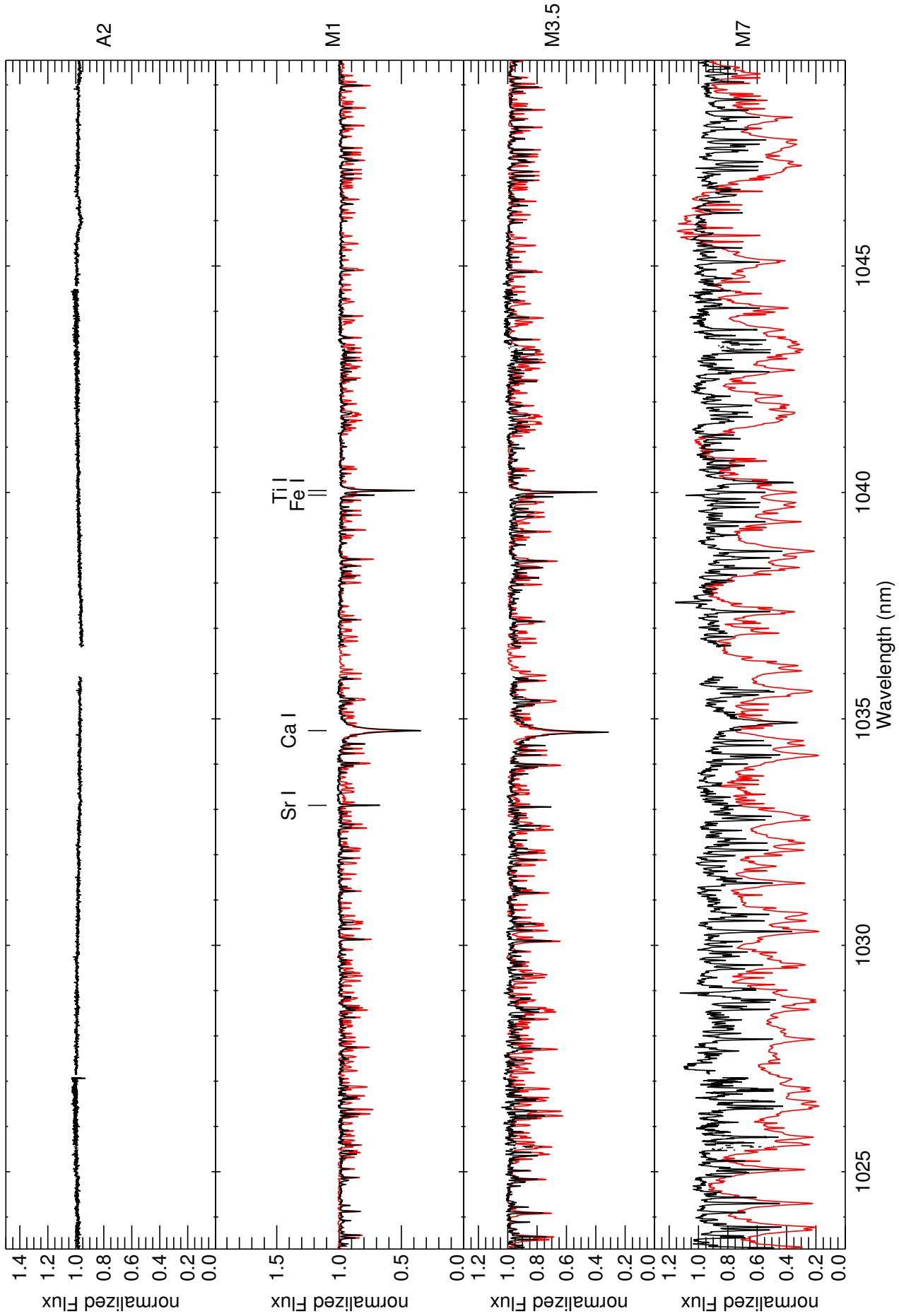


Fig. A.21. CARMENES spectral atlas.

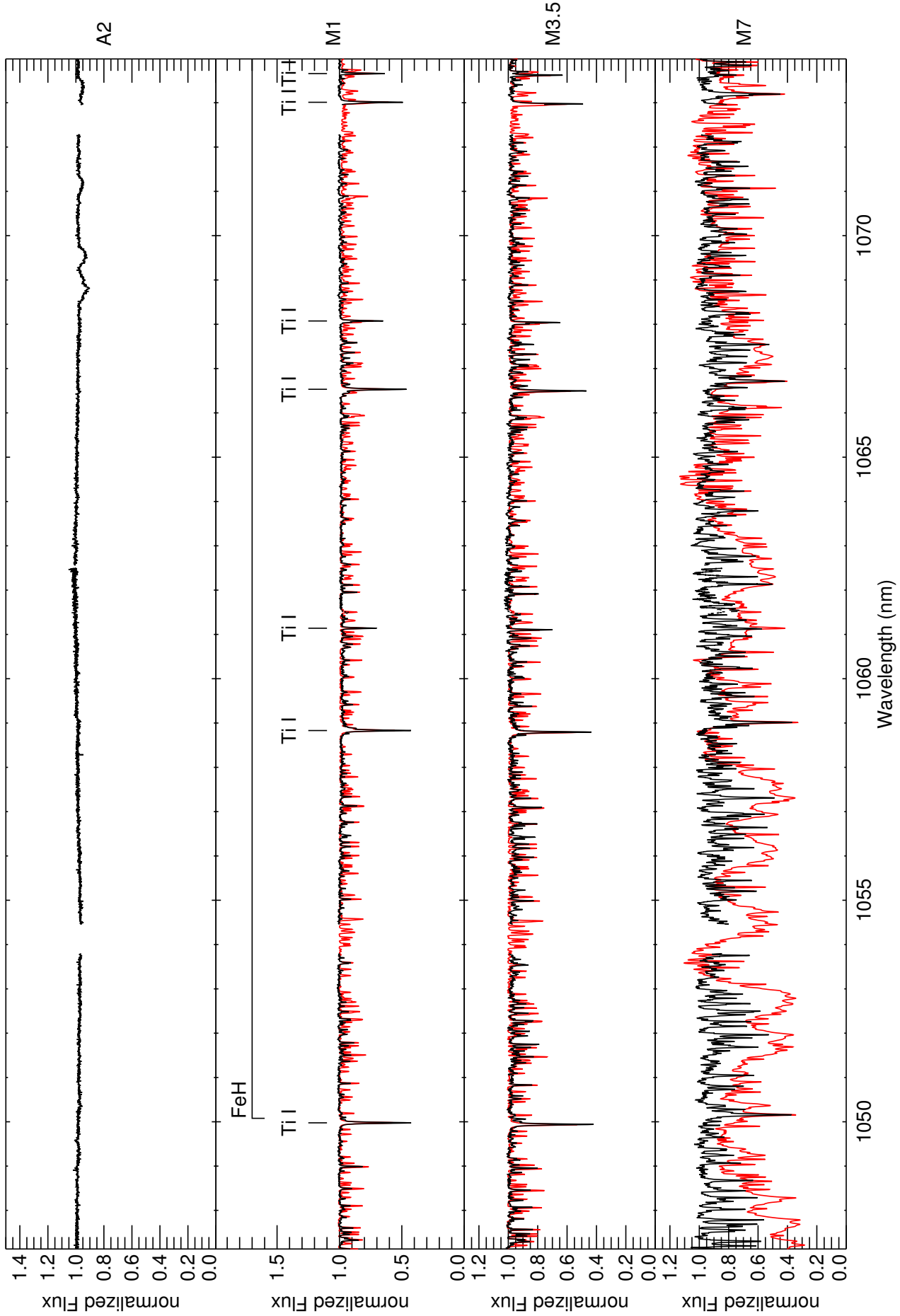


Fig. A.22. CARMENES spectral atlas.
Article number, page 36 of 63

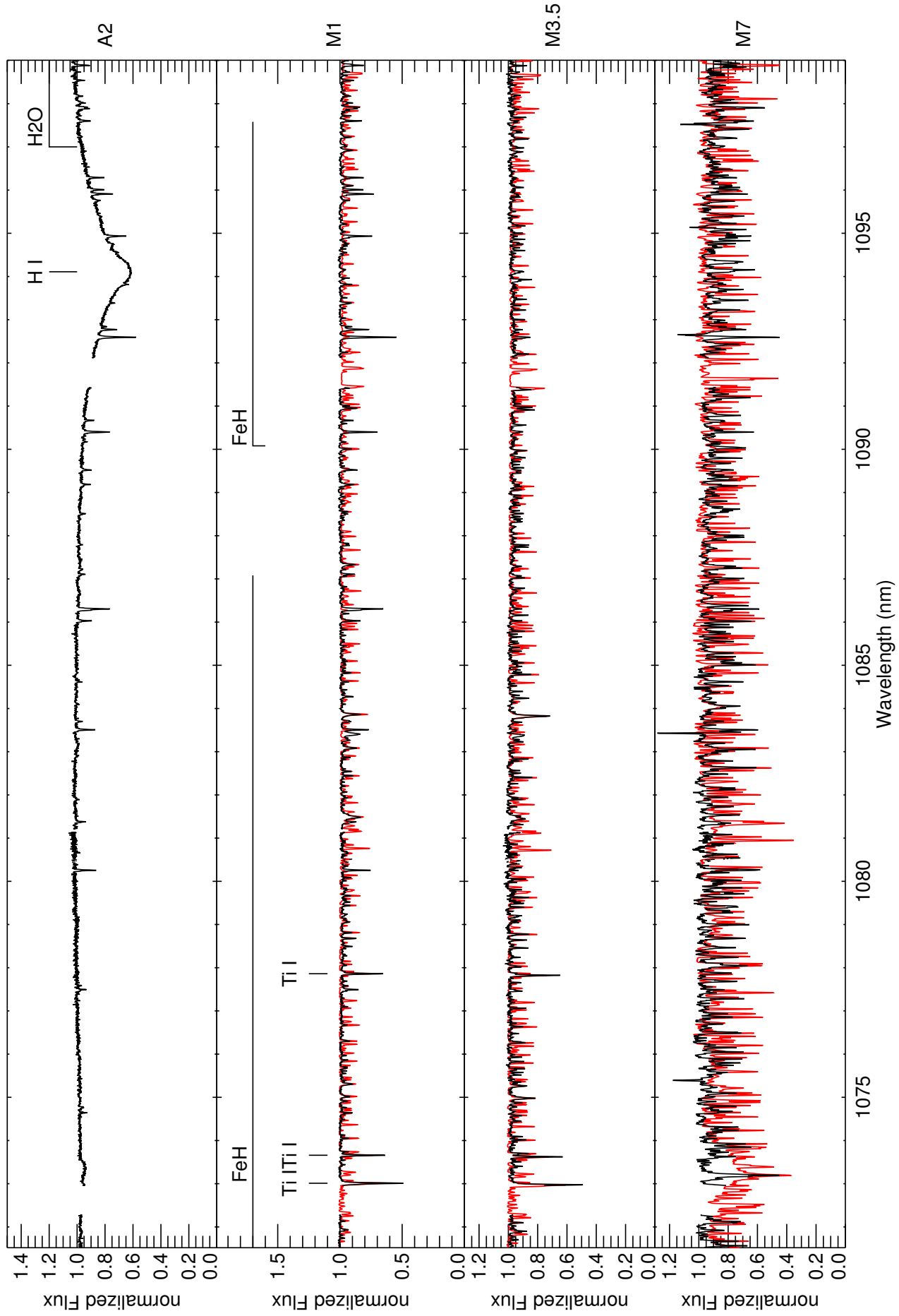


Fig. A.23. CARMENES spectral atlas.

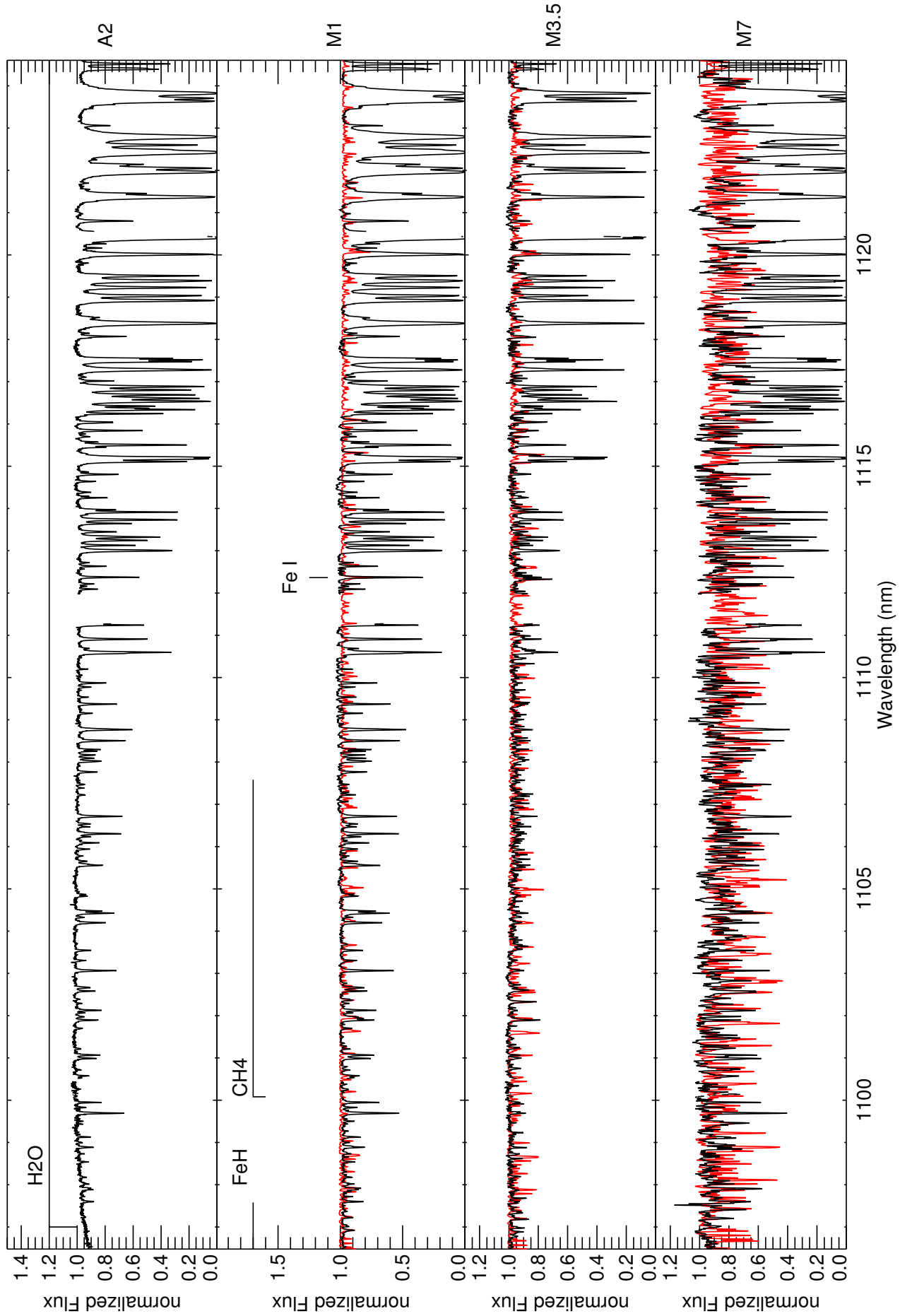


Fig. A.24. CARMENES spectral atlas.
Article number, page 38 of 63

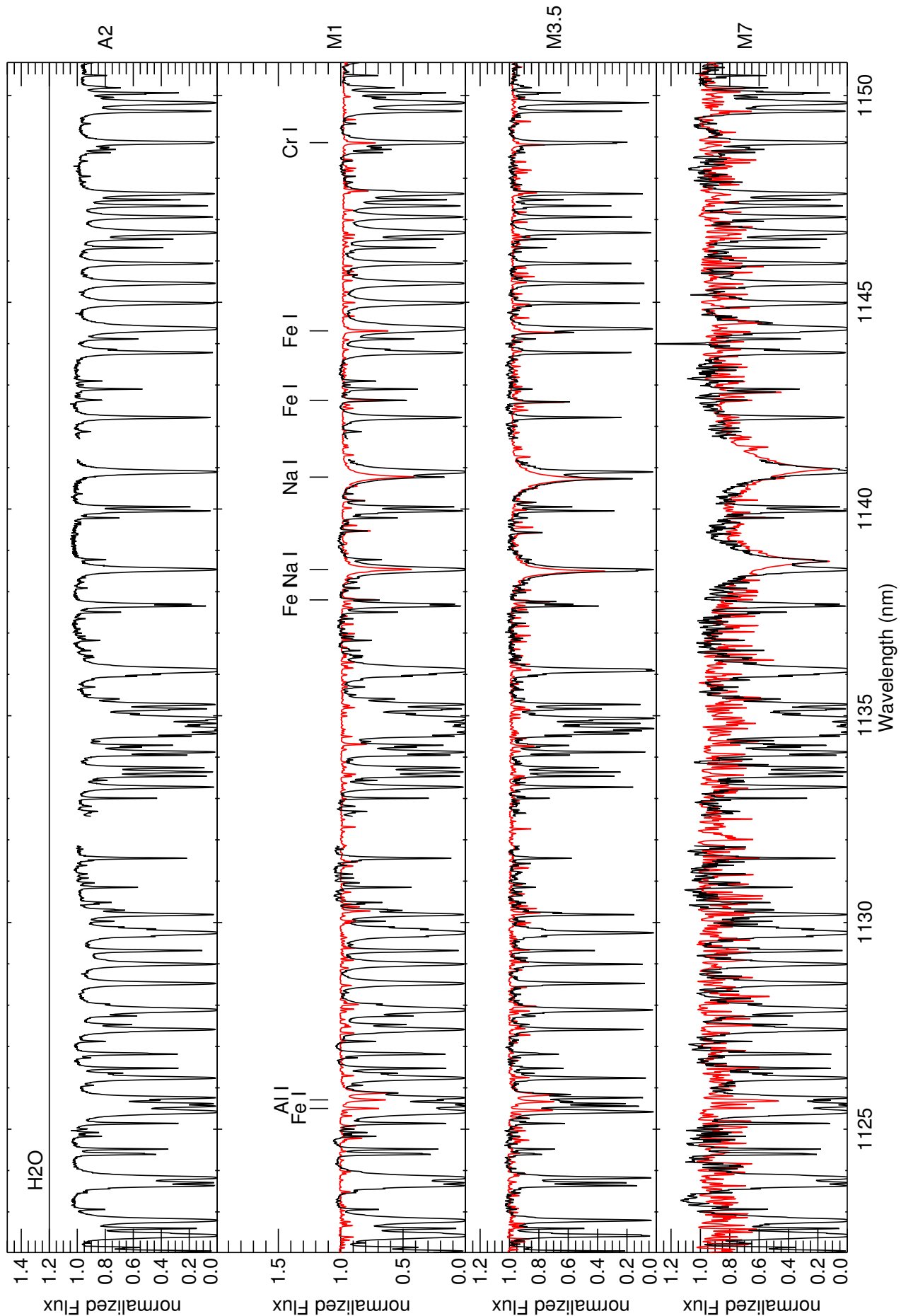


Fig. A.25. CARMENES spectral atlas.

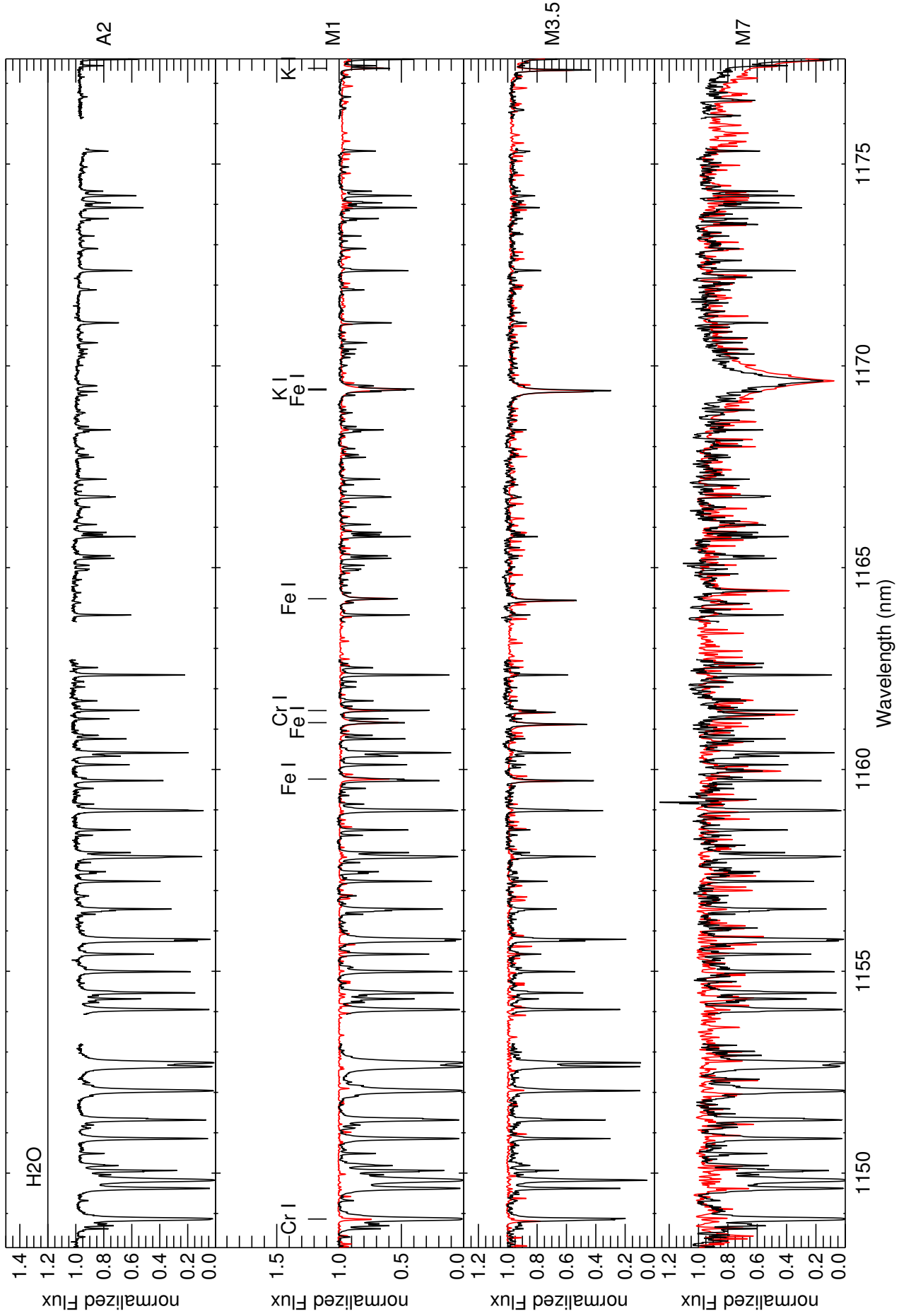


Fig. A.26. CARMENES spectral atlas.
Article number, page 40 of 63

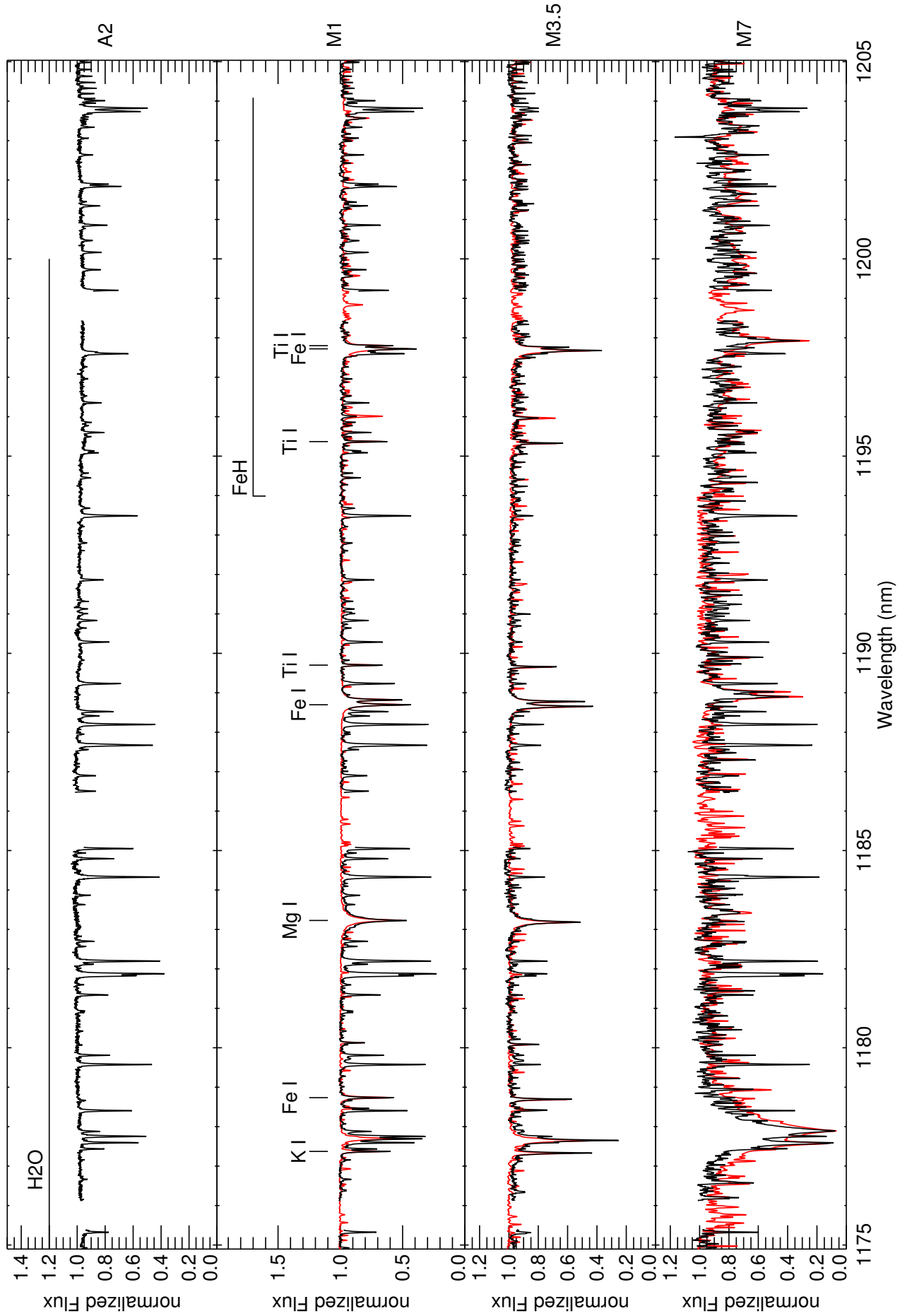


Fig. A.27. CARMENES spectral atlas.

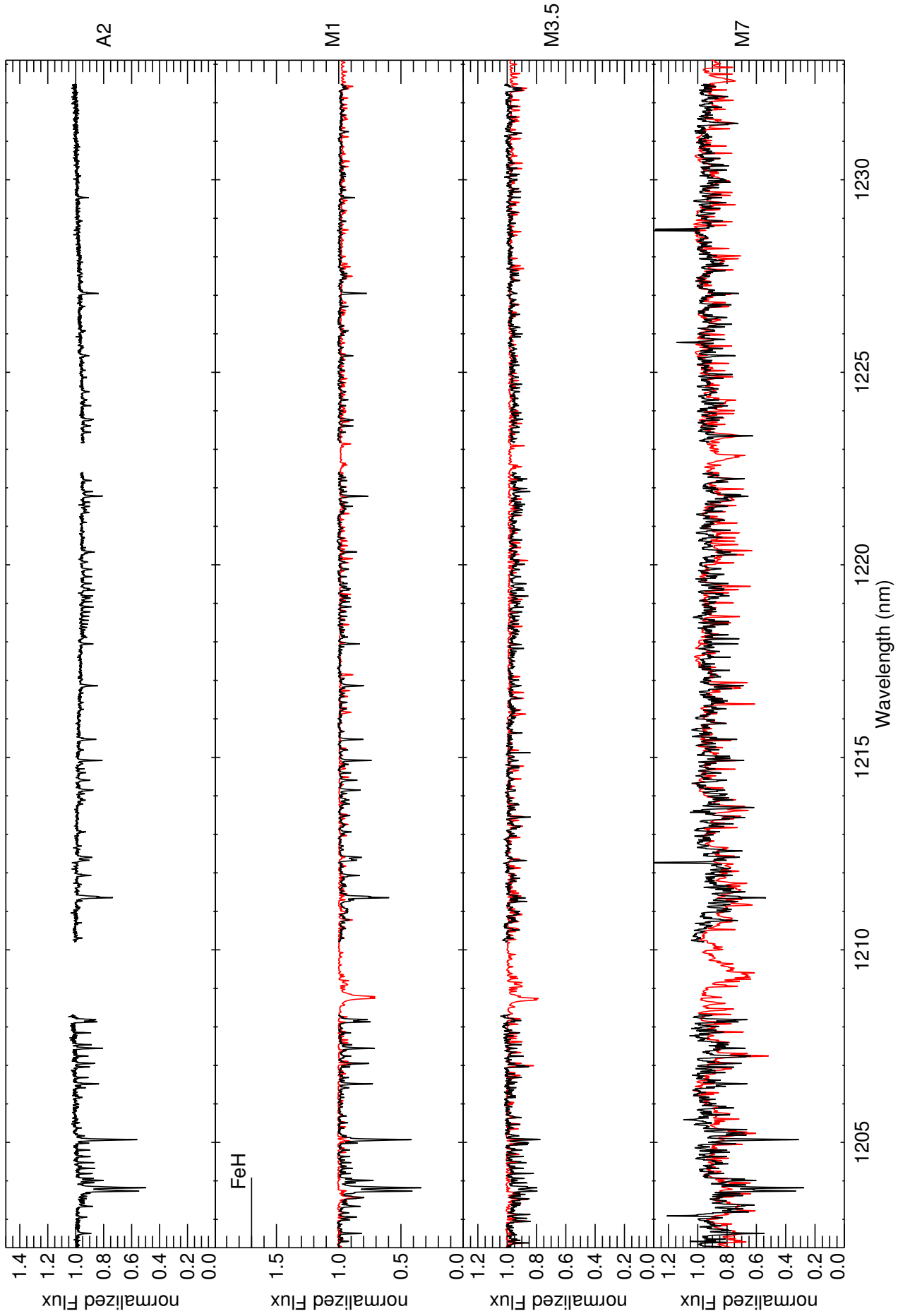


Fig. A.28. CARMENES spectral atlas.
Article number, page 42 of 63

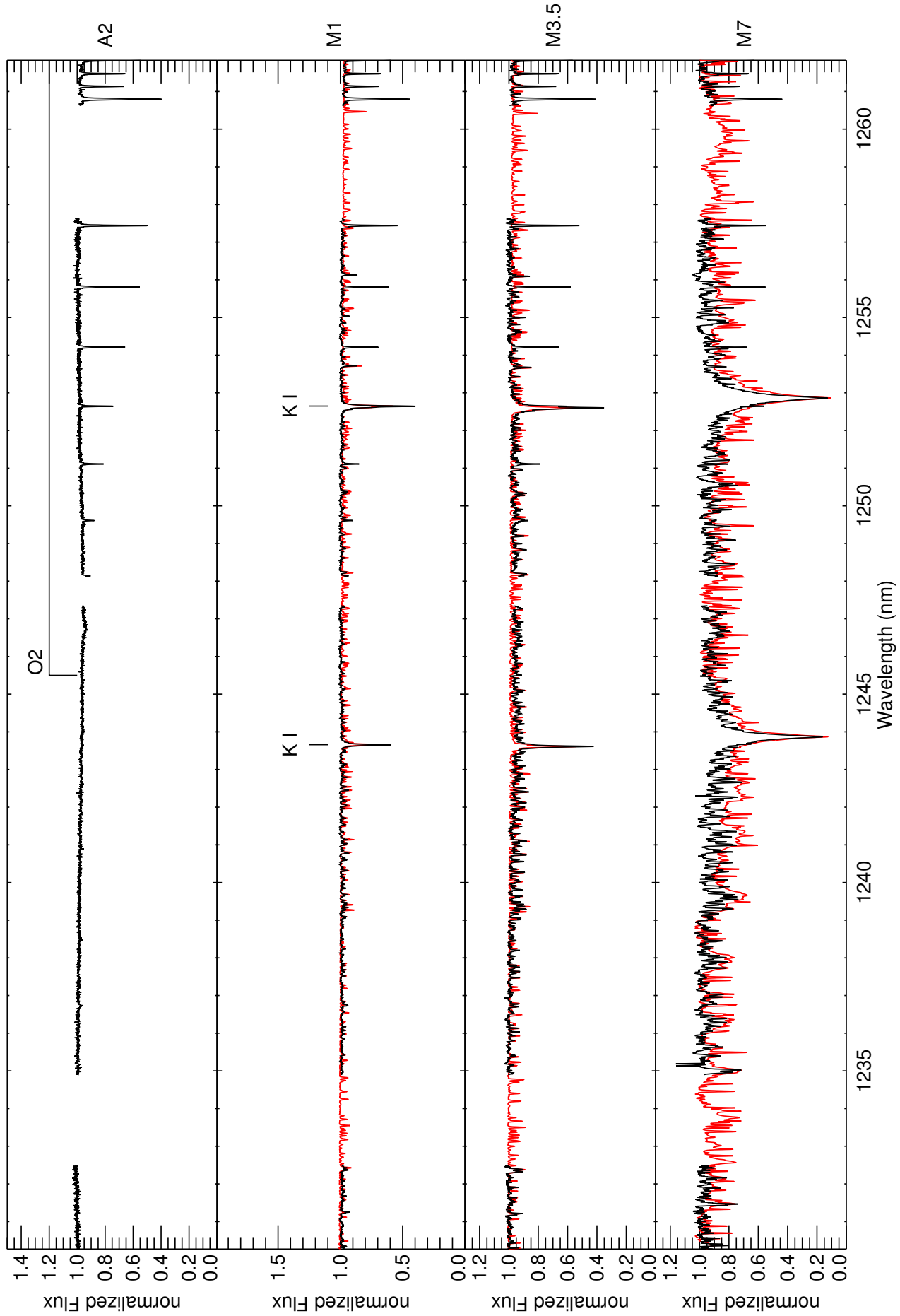


Fig. A.29. CARMENES spectral atlas.

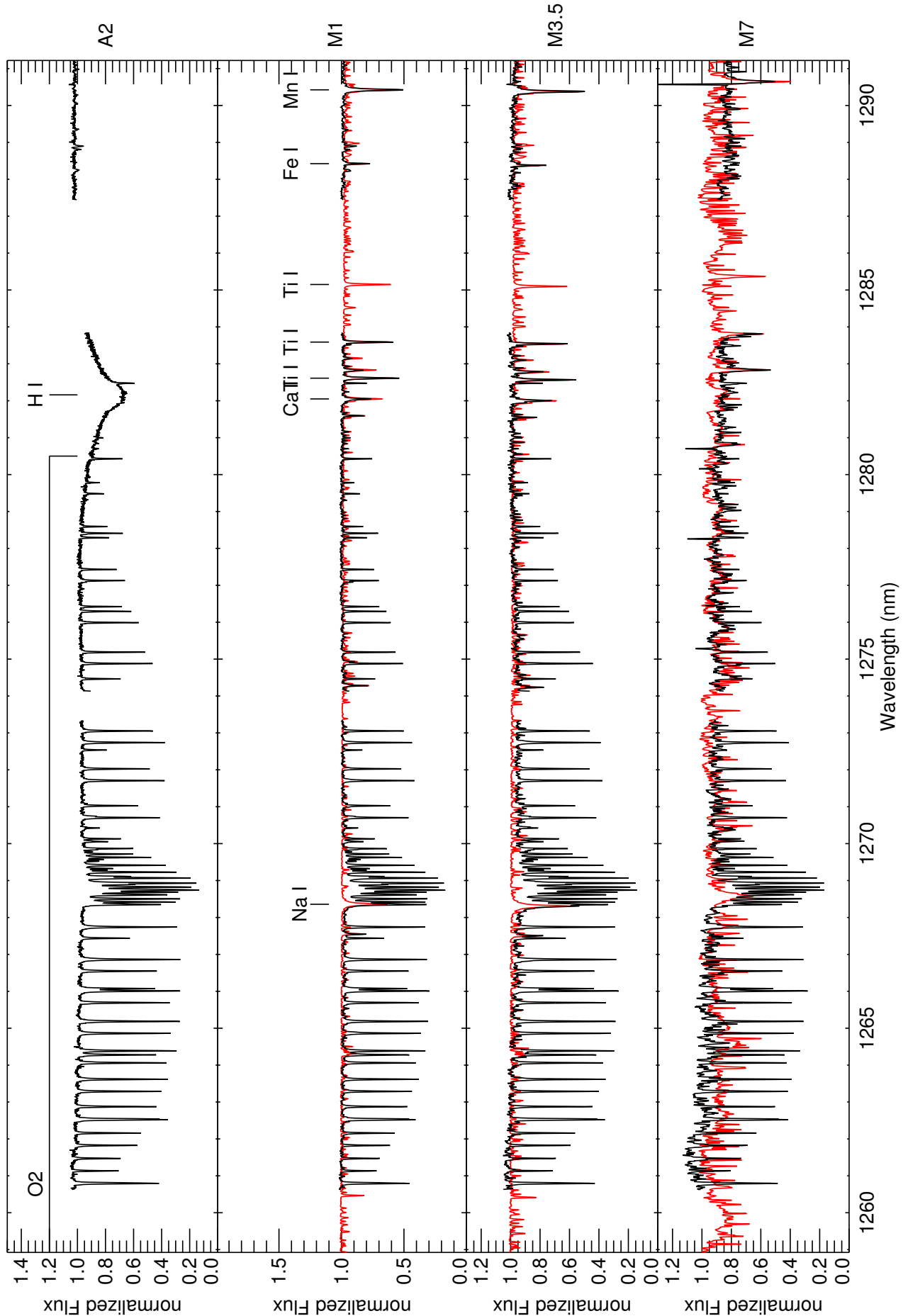


Fig. A.30. CARMENES spectral atlas.
Article number, page 44 of 63

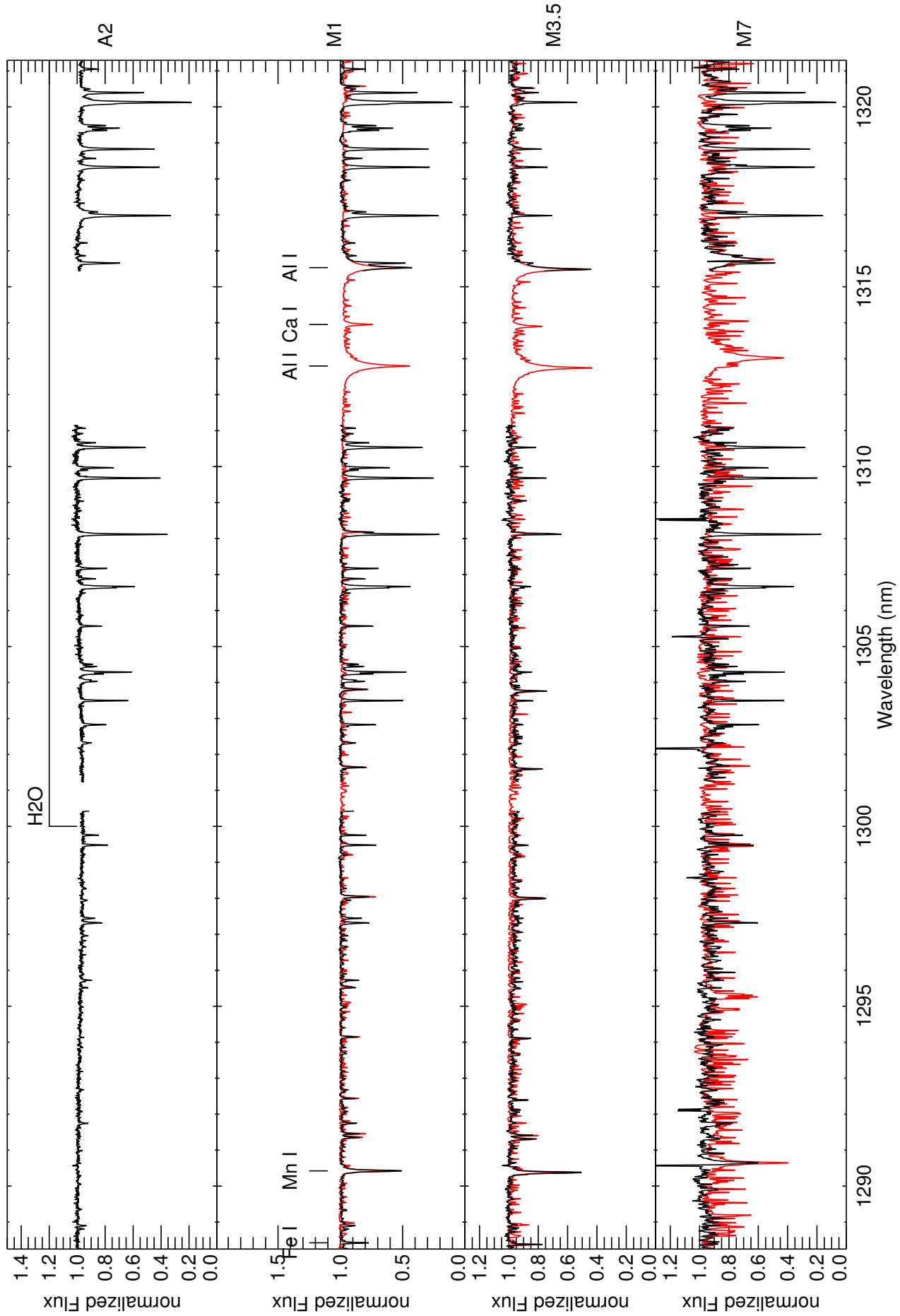


Fig. A.31. CARMENES spectral atlas.

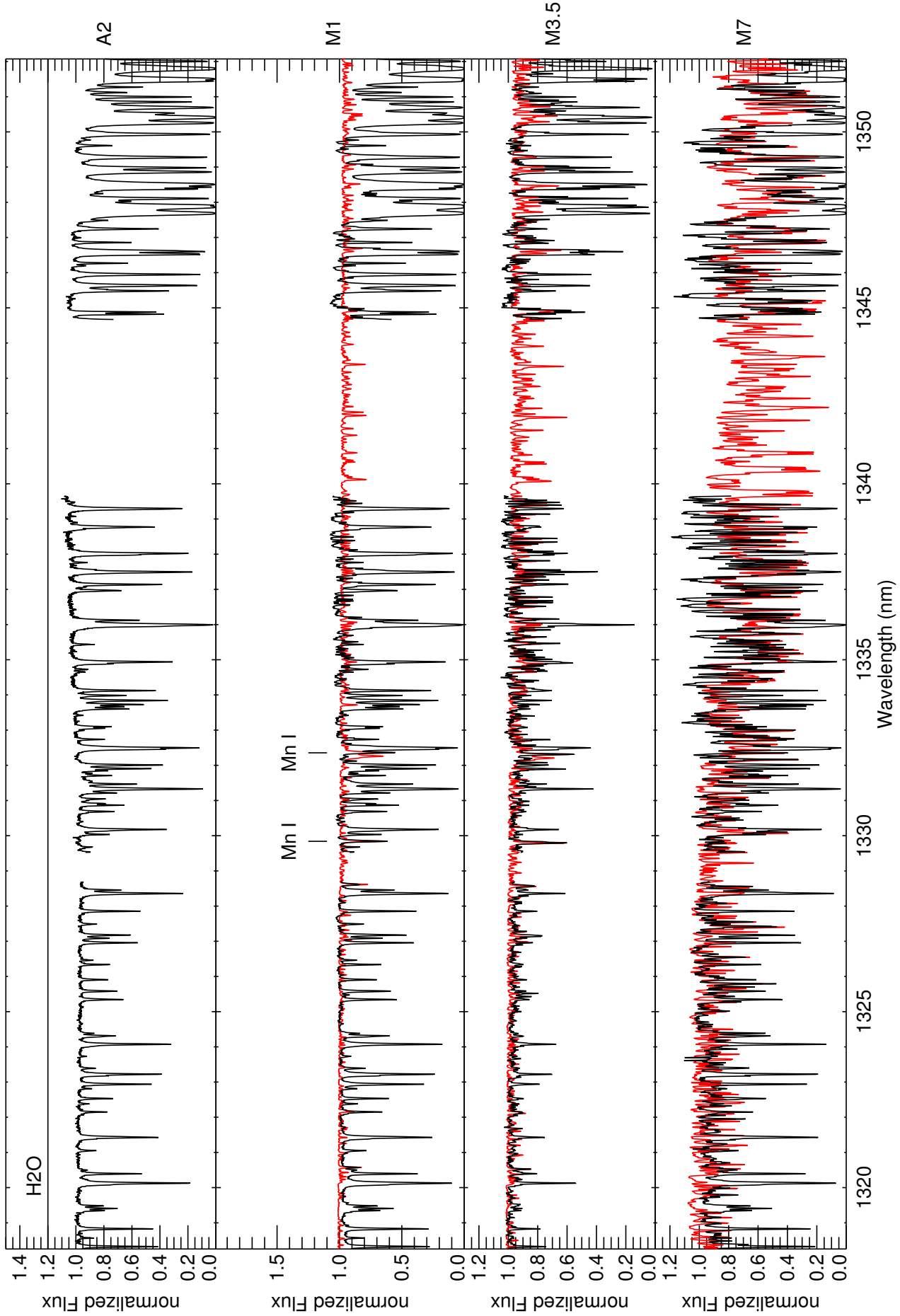


Fig. A.32. CARMENES spectral atlas.
Article number, page 46 of 63

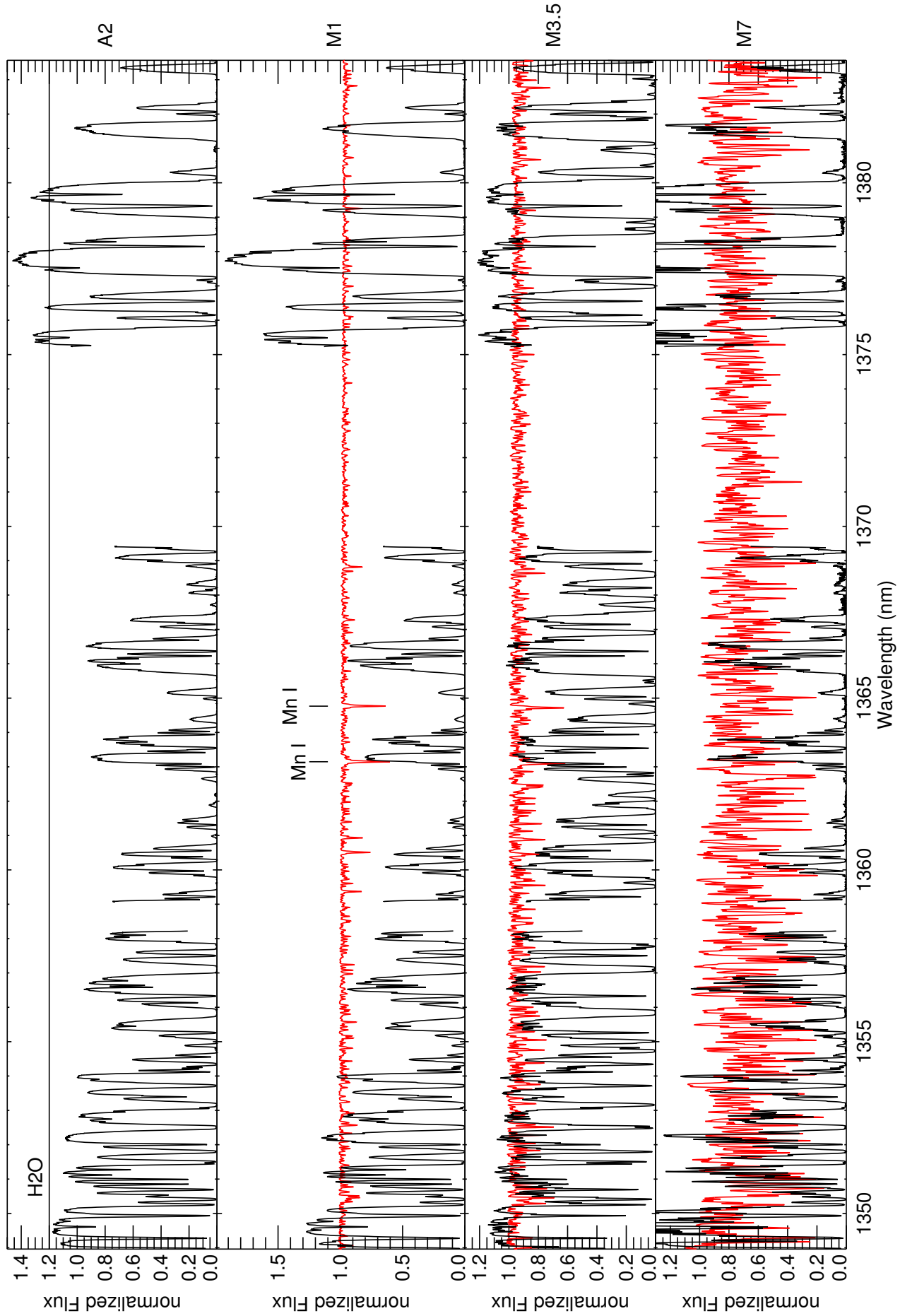


Fig. A.33. CARMENES spectral atlas.

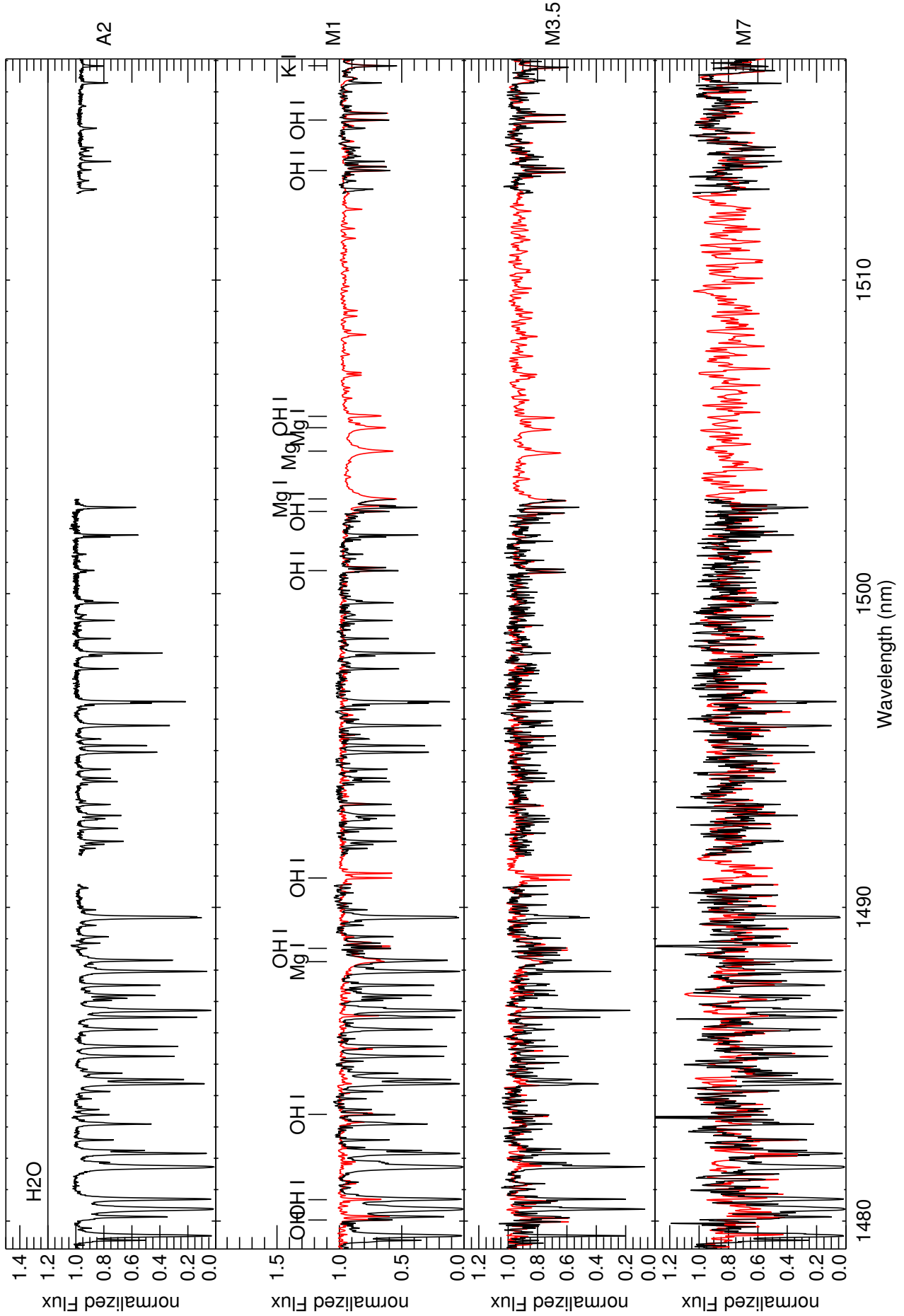


Fig. A.34. CARMENES spectral atlas.
Article number, page 48 of 63

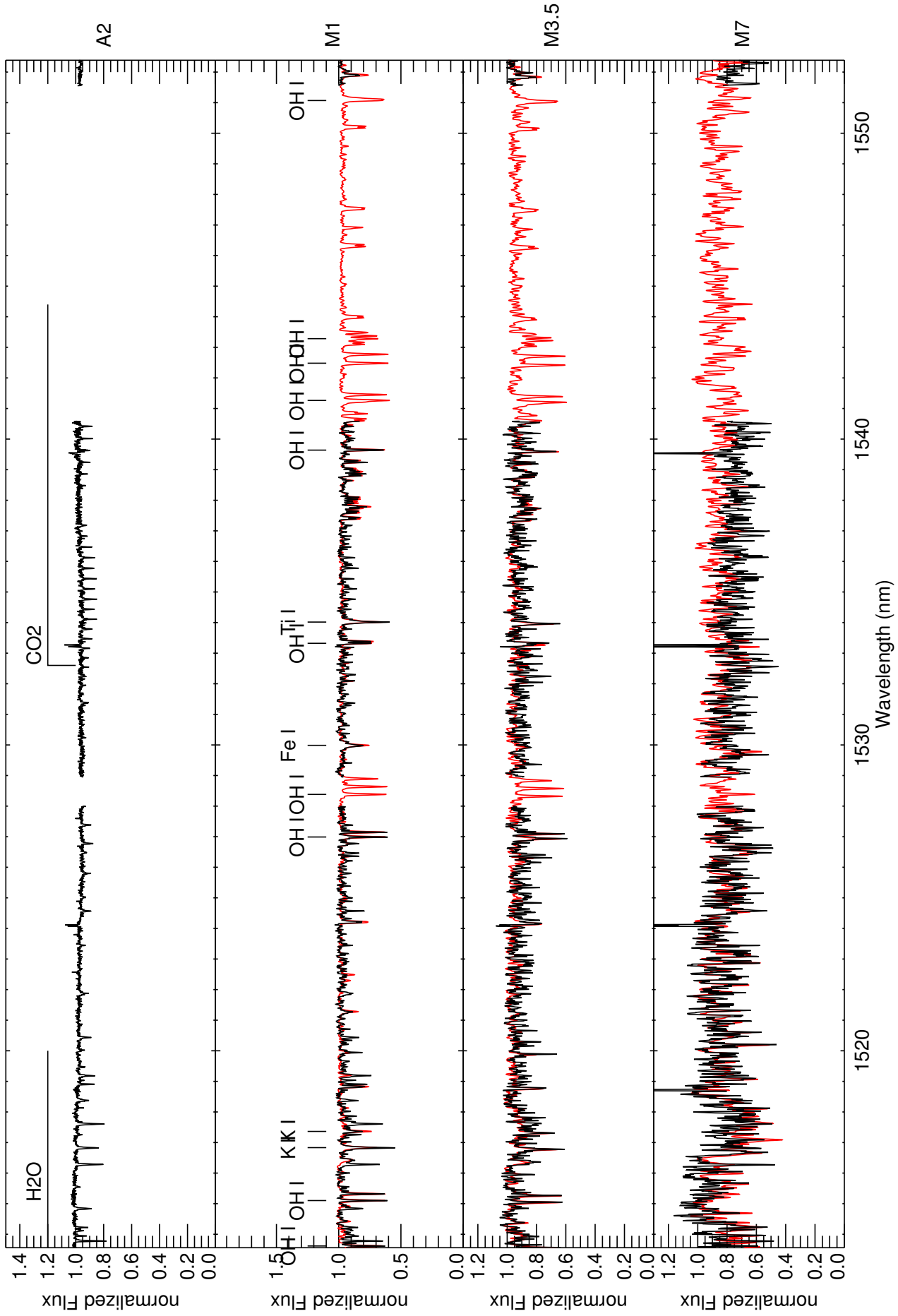


Fig. A.35. CARMENES spectral atlas.

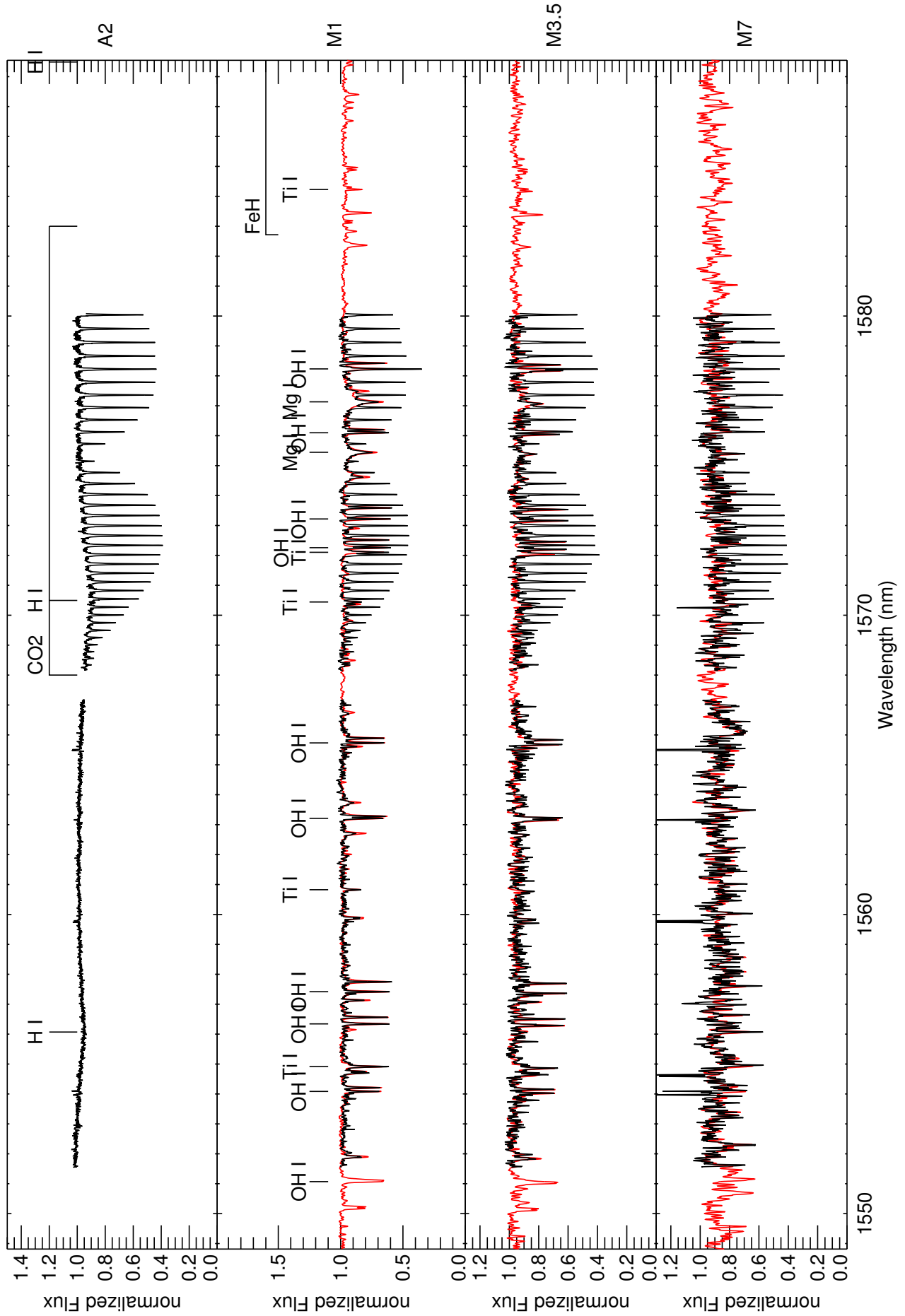


Fig. A.36. CARMENES spectral atlas.
Article number, page 50 of 63

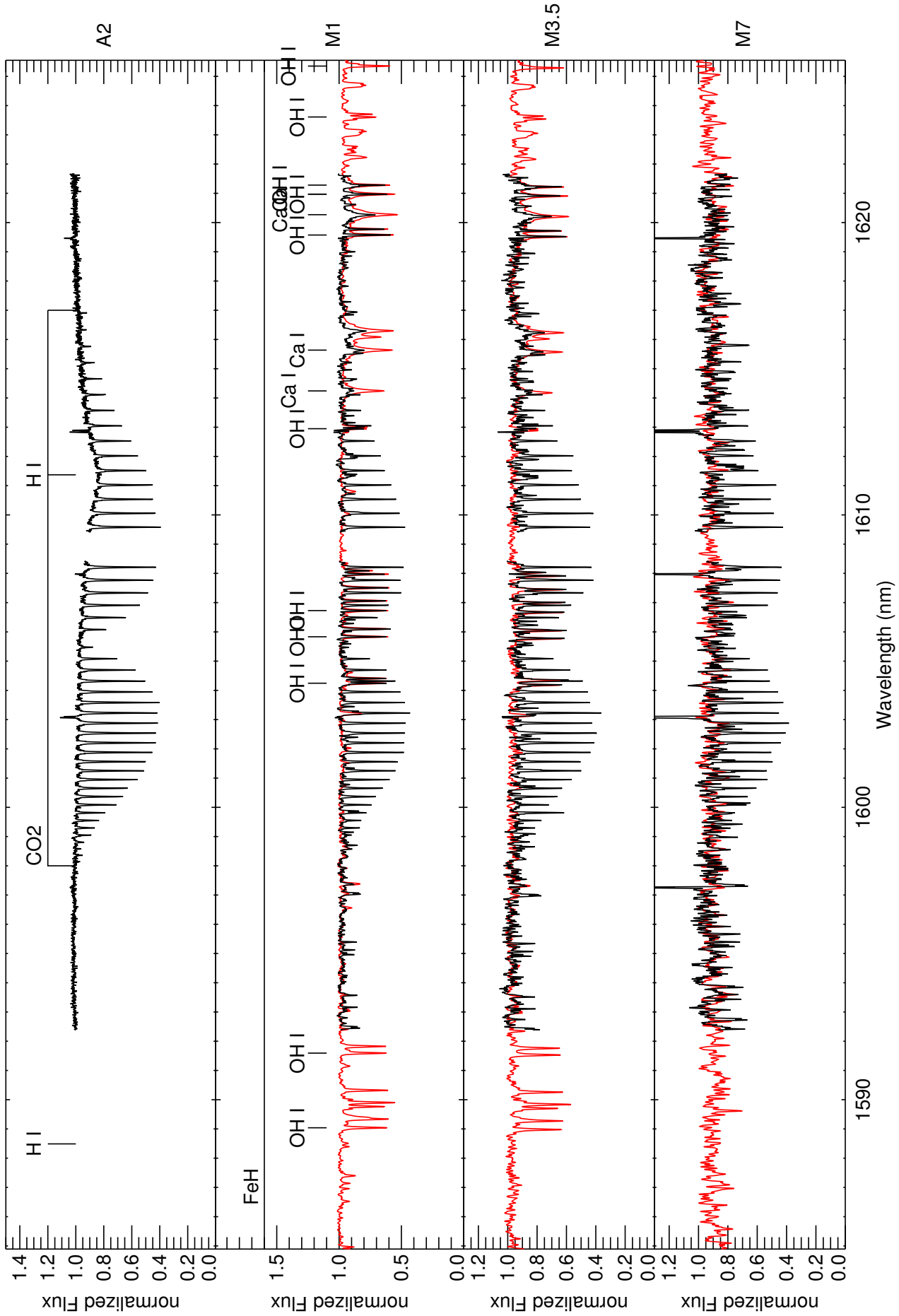


Fig. A.37. CARMENES spectral atlas.

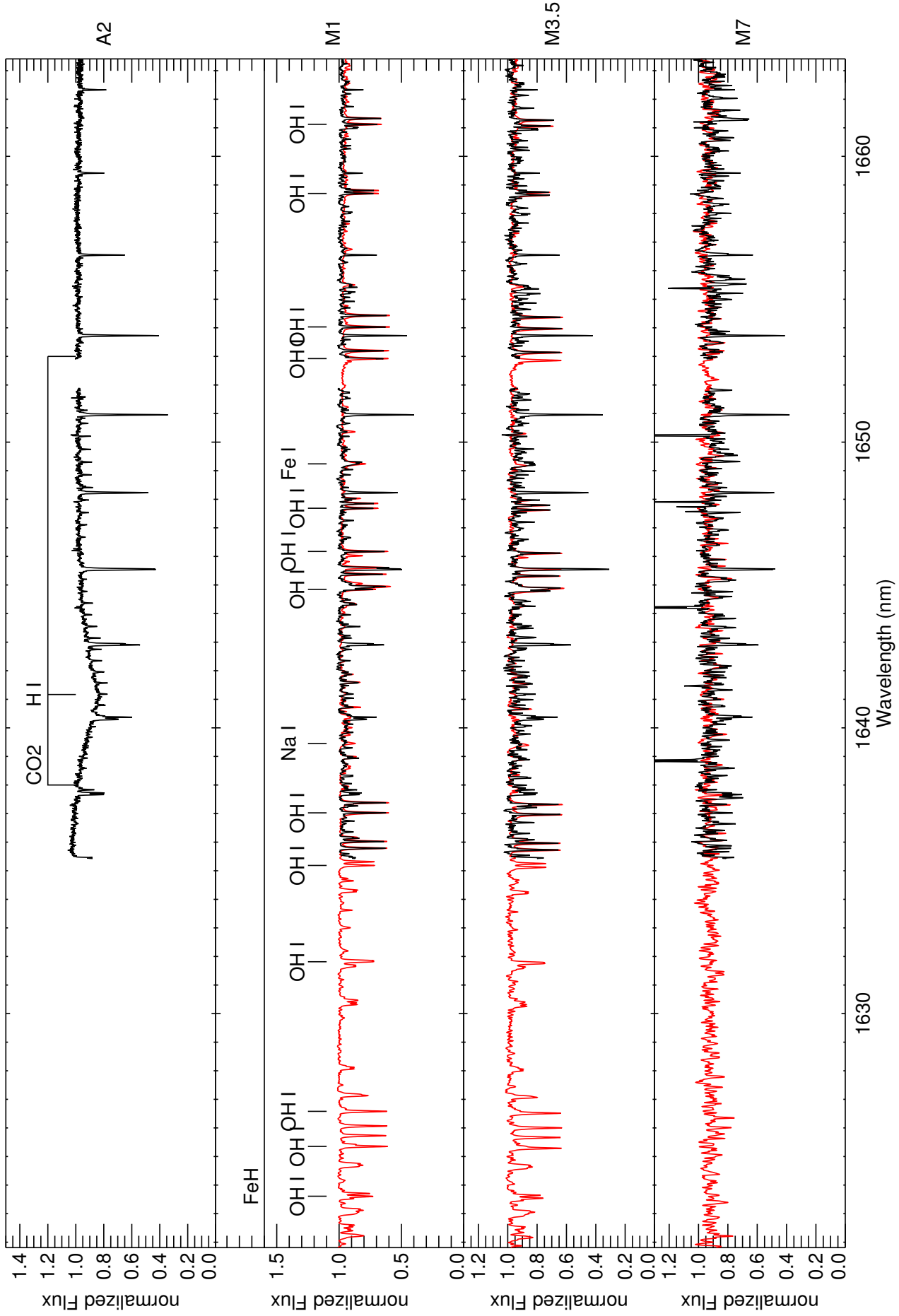


Fig. A.38. CARMENES spectral atlas.
Article number, page 52 of 63

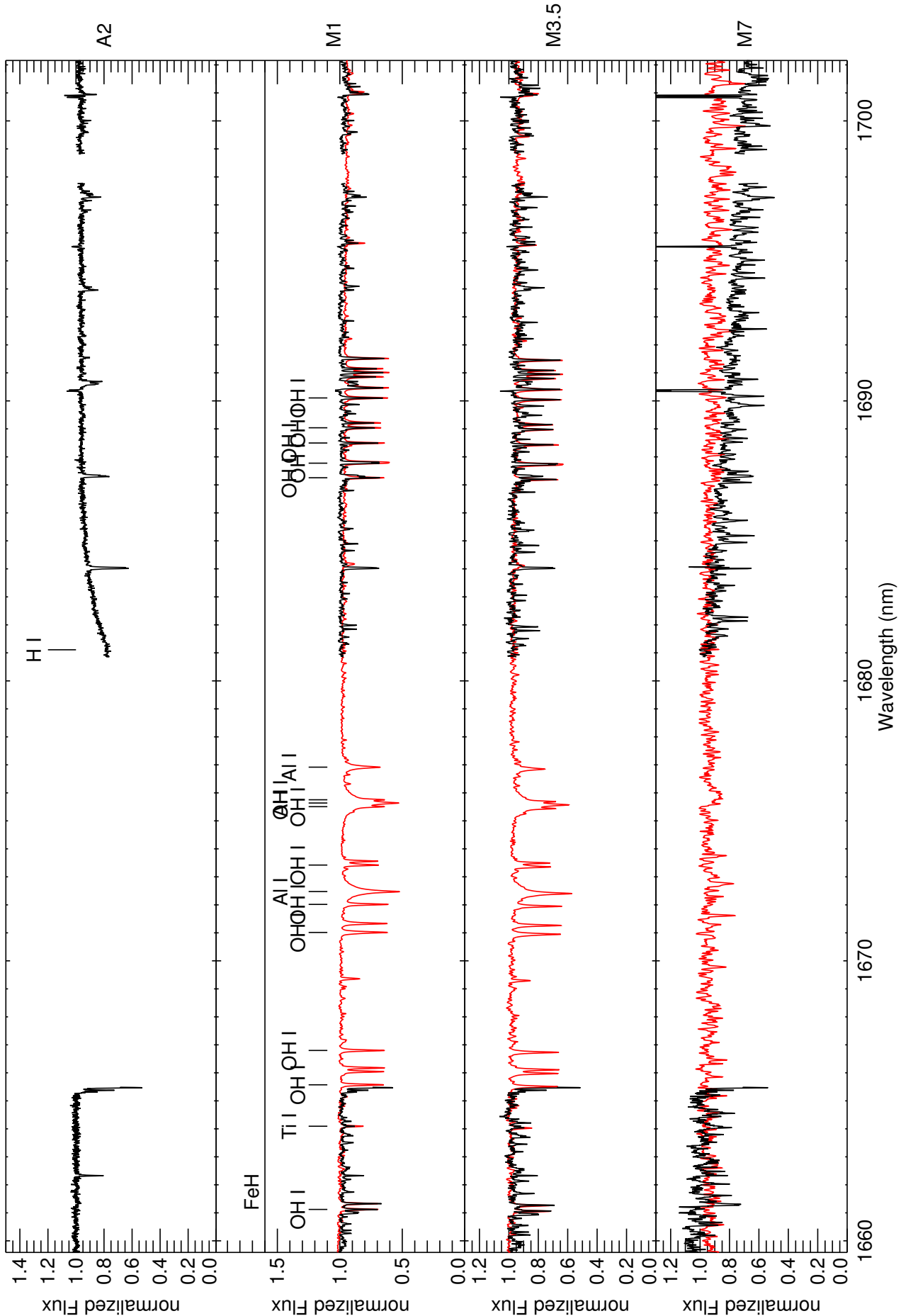


Fig. A.39. CARMENES spectral atlas.

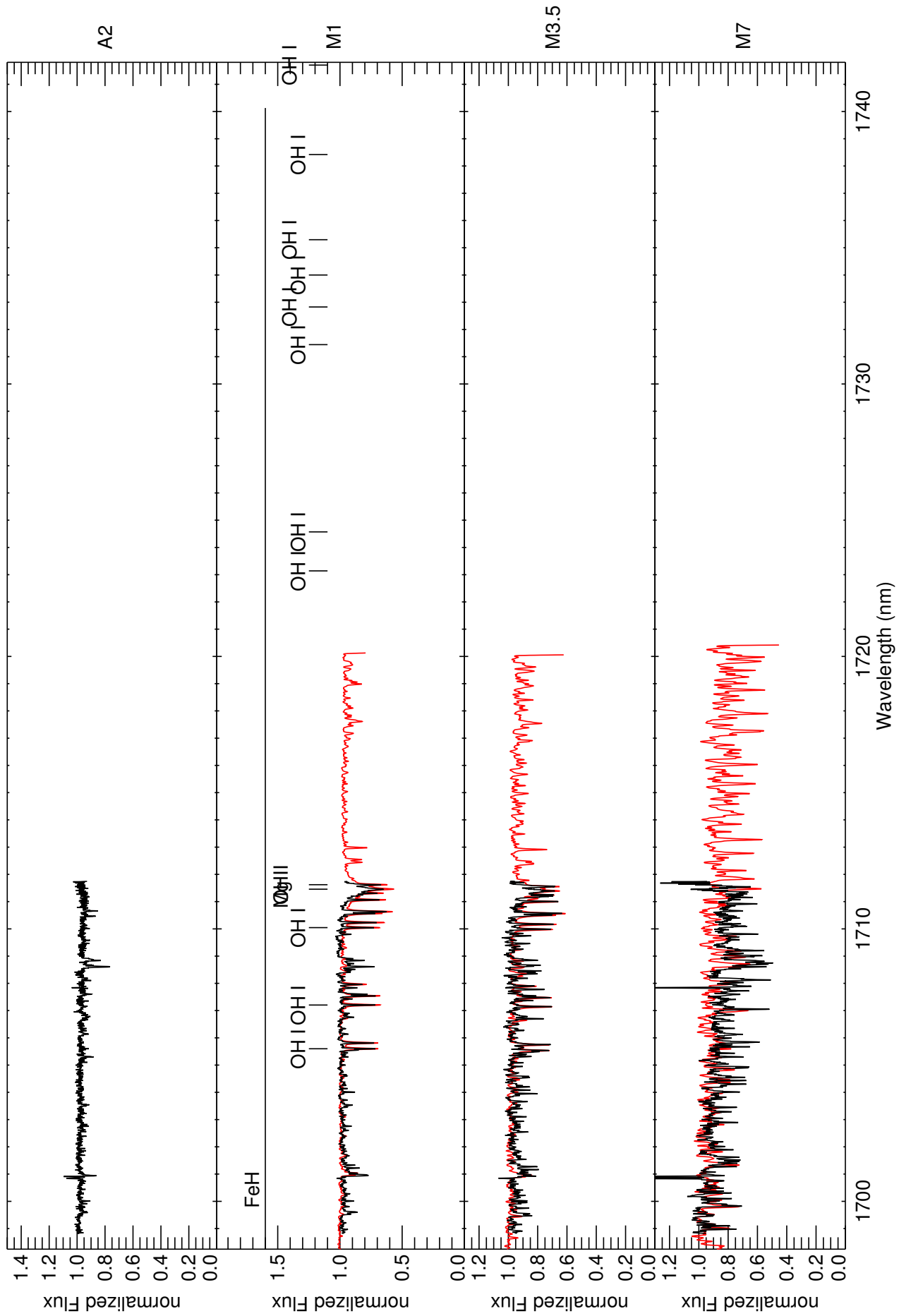


Fig. A.40. CARMENES spectral atlas.
Article number, page 54 of 63

Appendix B: Table of Targets

Basic data for the CARMENES GTO targets are provided in Table B.1. Columns are discussed in the main text. Uncertainties for estimates of the inclination angle i are computed only from the uncertainties in $v \sin i$.

Table B.1. Basic data of the CARMENES GTO sample

No.	ID	GJ	Name	SpT	J	M	v_{rad}	P	Ref.	$v \sin i$	$P_v \sin i / \sin i$	i	$\log L_{\text{H}\alpha} / L_{\text{bol}}$
					(mag)	(M $_{\odot}$)	(km s $^{-1}$)	(d)		(km s $^{-1}$)	(d)	deg	
001	J00051+457	2	GJ 2	M1.0	6.70	0.56	-0.392	< 2	> 13.3				-4.83
002	J00067-075	1002	GJ 1002	M5.5	8.32	0.11	-40.058	< 2	> 3.5				
003	J00162+198E	1006B	LP 404-062	M4.0	8.89	0.30	-1.457	104.00 ± 31.20	Irw11	< 2	> 7.4	≤ 90	
004	J00183+440	15A	GX And	M1.0	5.25	0.45	11.671	< 2	> 10.5				
005	J00184+440	15B	GQ And	M3.5	6.79	0.16	10.876	< 2	> 4.6				
006	J00286-066	1012	GJ 1012	M4.0	8.04	0.39	-12.531	< 2	> 9.1				
007	J00389+306	26	Wolf 1056	M2.5	7.45	0.47	-0.499	< 2	> 11.1				
008	J00570+450		G 172-030	M3.0	8.10	0.39	6.396	< 2	> 9.3				
009	J01013+613	47	GJ 47	M2.0	7.27	0.44	7.426	< 2	> 10.4				-4.47
010	J01019+541	3069	G 218-020	M5.0	9.78	0.13	-6.127	0.28	New16a	30.6 ± 3.1	0.25 ± 0.02	90 ± 9	-3.76
011	J01025+716	48	BD+70 68	M3.0	6.30	0.51	1.362	< 2	> 12.1				
012	J01026+623	49	BD+61 195	M1.5	6.23	0.60	-6.131	< 2	> 14.1				
013	J01033+623	51	V388 Cas	M5.0	8.61	0.20	-6.291	1.06 ± 0.02	Irw11	10.5 ± 1.5	1.1 ± 0.2	90 ± 12	-3.54
014	J01048-181	1028	GJ 1028	M5.0	9.39	0.14	11.407	< 2	> 4.0				
015	J01125-169	54.1	YZ Cet	M4.5	7.26	0.13	27.984	69.20 ± 0.10	SM16	< 2	> 3.9	≤ 90	-4.32
016	J01339-176		LP 768-113	M4.0	8.84	0.25	6.292	< 2	> 6.5				-4.15
017	J01352-072		Barta 161	M4.0	8.96	0.26	6.039	59.8 ± 6.9		0.22 ± 0.03			-3.49
018	J01433+043	70	GJ 70	M2.0	7.37	0.45	-26.009	< 2	> 10.6				
019	J01518+644	3117A	G 244-037	M2.5	7.84	0.47	-1.2935	< 2	> 11.0				
020	J02002+130	83.1	TZ Ari	M3.5	7.51	0.14	-28.639	< 2	> 4.2				-4.03
021	J02015+637	3126	G 244-047	M3.0	7.26	0.52	-84.287	< 2	> 12.3				
022	J02070+496		G 173-037	M3.5	8.37	0.43	18.934	< 2	> 10.1				-4.54
023	J02088+494	3136	G 173-039	M3.5	8.42	0.32	-9.924	24.1 ± 2.4		0.64 ± 0.06			-3.53
024	J02123+035	87	BD+02 348	M1.5	6.83	0.50	-2.694	< 2	> 11.7				
025	J02222+478	96	BD+47 612	M0.5	6.38	0.62	-38.150	< 2	> 14.6				
026	J02336+249	102	GJ 102	M4.0	8.47	0.21	-6.495	3.0 ± 1.5		3.7 ± 1.8			
027	J02358+202	104	BD+19 381	M2.0	7.21	0.56	0.896	< 2	> 13.1				
028	J02362+068	105B	BX Cet	M4.0	7.33	0.26	26.131	< 2	> 6.6				
029	J02442+255	109	VX Ari	M3.0	6.75	0.38	30.425	< 2	> 9.1				
030	J02519+224		RBS 365	M4.0	8.92	0.25	-18.849	27.2 ± 2.7		0.47 ± 0.05			-3.60
031	J02530+168		Teegardens	M7.0	8.39	0.09	68.375	< 2	> 2.9				-5.18
032	J02565+554W	119A	Ross 364	M1.0	7.42	0.69	76.454	< 2	> 16.1				
033	J03133+047	1057	CD Cet	M5.0	8.78	0.16	28.187	< 2	> 4.6	≤ 90			
034	J03181+382	134	HD 275122	M1.5	7.02	0.64	-4.365	< 2	> 15.1				
035	J03213+799	133	GI 133	M2.0	7.70	0.47	-13.394	< 2	> 10.9				
036	J03217-066	3218	G 077-046	M2.0	7.86	0.52	26.297	< 2	> 12.3				
037	J03463+262	154	HD 23453	M0.0	6.69	0.66	35.942	< 2	> 15.1				
038	J03473-019		G 080-021	M3.0	7.80	0.51	17.891	3.88	Kira12	5.2 ± 1.5	4.7 ± 1.4	55 ± 16	-3.67
039	J03531+625		Ross 567	M3.0	7.78	0.38	-120.236	< 2	> 9.0				
040	J04153-076	166C	om02 Eri	M4.5	6.75	0.23	-4.3415	2.1 ± 1.5		5.9 ± 4.3			-3.95
041	J04198+425		LSR J0419+	M8.5	11.09	0.09	38.008	3.6 ± 2.3		1.5 ± 1.0			-4.27
042	J04225+105		LSPM J0422	M3.5	8.47	0.57	36.904	< 2	> 13.6				
043	J04290+219	169	BD+21 652	M0.5	5.67	0.74	-35.312	3.9 ± 1.5		8.8 ± 3.3			

Table B.1. continued.

No.	ID	GJ	Name	SpT	<i>J</i>	<i>M</i>	v_{rad} (km s $^{-1}$)	<i>P</i> (d)	Ref.	$v \sin i$ (km s $^{-1}$)	$P_v \sin i / \sin i$ (d)	<i>i</i> deg	$\log L_{\text{H}\alpha} / L_{\text{bol}}$
044	J04376+528	172	BD+52 857	M0.0	5.87	0.65	34,249			3.4 ± 1.5	9.0 ± 4.0		
045	J04376-110	173	BD-11 916	M1.5	6.94	0.52	-6,902	< 2		< 2	> 12.2		
046	J04429+189	176	HD 285968	M2.0	6.46	0.54	26,075	38.92	KS07	< 2	> 12.7	≤ 90	
047	J04429+214	2M J044255		M3.5	7.96	0.32	2,994			< 2	> 7.8		-3.54
048	J04472+206	179	RX J0447.2	M5.0	9.38	0.15	15,081			47.6 ± 26.8	0.2 ± 0.1		
049	J04520+064	180	Wolf 1539	M3.5	7.81	0.40	-8,914			< 2	> 9.4		
050	J04538-177	181	GJ 180	M2.0	7.41	0.46	1,036			< 2	> 10.8		
051	J04588+498	181	BD+49 1280	M0.0	6.92	0.65	-34,004			< 2	> 15.3		
052	J05019+011		IRXS J0501	M4.0	8.53	0.25	-7,601			6.5 ± 1.5	2.0 ± 0.5		-3.58
053	J05019-069	3323	LP 656-038	M4.0	7.62	0.17	17,252	88.50	Kira12	< 2	> 4.8	≤ 90	-4.57
054	J05033-173	3325	LP 776-049	M3.0	7.82	0.29	-6,332			< 2	> 7.1		
055	J05062+046		RX J0506.2	M4.0	8.91	0.25	0.219	0.89	Kira12	24.9 ± 2.5	0.52 ± 0.05	90 ± 9	-3.51
056	J05084-210	2M J050827	M5.0	9.72	0.15	33,752			< 2	25.2 ± 2.5	0.35 ± 0.03		-3.32
057	J05127+196	192	GJ 192	M2.0	7.30	0.49	-25,174			< 2	> 11.5		
058	J05280+096	203	Ross 41	M3.5	8.31	0.25	60,489			< 2	> 6.4		
059	J05314-036	205	HD 36395	M1.5	5.00	0.60	8,517	33.61	KS07	< 2	> 14.1	≤ 90	
060	J05337+019	207.1	V371 Ori	M2.5	7.76	0.52	44,887	2.81 ± 0.25	HM15	9.8 ± 1.5	2.5 ± 0.4	90 ± 13	-3.53
061	J05348+138	3356	Ross 46	M3.5	7.78	0.41	37,592			< 2	> 9.5		
062	J05360-076	3357	Wolf 1457	M4.0	8.46	0.26	29,237			< 2	> 6.6		
063	J05365+113	208	V2689 Ori	M0.0	6.13	0.66	21,941	12.04	Kira12	3.8 ± 1.5	8.1 ± 3.2	90 ± 35	-4.41
064	J05366+112		2M J053638	M4.0	8.27	0.28	43,336			2.4 ± 1.5	5.8 ± 3.6		-3.93
065	J05394+406		LSR J0539+	M8.0	11.11	0.08	4,220			4.1 ± 1.5	1.2 ± 0.5		-4.42
066	J05415+534	212	HD 233153	M1.0	6.59	0.60	1,982			< 2	> 14.3		
067	J05421+124	213	V1352 Ori	M4.0	7.12	0.22	105,798			< 2	> 5.9		
068	J06000+027	3379	G 099-049	M4.0	6.91	0.24	30,087	1.81 ± 0.02	Irwl1	4.9 ± 1.5	2.5 ± 0.8	45 ± 14	-3.95
069	J06011+595	3378	G 192-013	M3.5	7.46	0.27	1,897			< 2	> 6.7		
070	J06024+498	3380	G 192-015	M5.0	9.35	0.13	20,291	99,60 ± 10,00	Irwl1	< 2	> 3.9	≤ 90	
071	J06103+821	226	GJ 226	M2.0	6.87	0.46	-1,747			< 2	> 10.8		
072	J06105-218	229A	HD 42581 A	M0.5	5.10	0.60	4,540	27.30 ± 0.10	SM16	< 2	> 14.1	≤ 90	
073	J06246+234	232	Ross 64	M4.0	8.66	0.15	-11,482			< 2	> 4.4		
074	J06318+414	3396	LP 205-044	M5.0	9.68	0.13	-12,340	0.30	New16a	58.4 ± 26.1	0.14 ± 0.06	90 ± 40	-3.46
075	J06371+175	239	HD 260655	M0.0	6.67	0.51	-58,325			< 2	> 12.0		
076	J06396-210		LP 780-032	M4.0	8.51	0.25	-28,122			< 2	> 6.5		
077	J06421+035	3404A	G 108-021	M3.5	8.17	0.42	96,591			< 2	> 9.9		
078	J06548+332	251	Wolf 294	M3.0	6.10	0.39	22,806			< 2	> 9.2		
079	J06574+740		2M J065726	M4.0	8.93	0.25	15,184			27.1 ± 2.7	0.47 ± 0.05		-3.63
080	J06594+193	1093	GJ 1093	M5.0	9.16	0.12	-29,475			< 2	> 3.7		-4.70
081	J07001-190		2M J070006	M5.0	9.03	0.15	12,878			3.8 ± 1.5	2.4 ± 1.0		-3.70
082	J07033+346	3423	LP 255-011	M4.0	8.77	0.27	2,179			< 2	> 6.8		-3.90
083	J07044+682	258	GJ 258	M3.0	8.17	0.42	-50,635			< 2	> 9.8		
084	J07274+052	273	Luytens St	M3.5	5.71	0.32	18,096			< 2	> 7.6		
085	J07287-032	1097	GJ 1097	M3.0	7.54	0.45	1,303			< 2	> 10.5		
086	J07319+362N	277C	BL Lyn	M3.5	7.57	0.42	-0.885			< 2	> 9.9		-3.90

Table B.1. continued.

No.	ID	GJ	Name	SpT	J	M	v_{rad}	P	Ref.	$v \sin i$	$P_v \sin i / \sin i$	i	$\log L_{\text{H}\alpha} / L_{\text{bol}}$
					(mag)	(M $_{\odot}$)	(km s $^{-1}$)	(d)		(km s $^{-1}$)	(d)	deg	
087	J07353+548	3452	GJ 3452	M2.0	7.77	0.41	-15.080	<2	Kira12	3.1 ± 1.5	9.5 ± 4.6	90 ± 43	-4.28
088	J07361-031	282C	BD-02 2198	M1.0	6.79	0.62	-17.112	12.16		<2	>7.7		
089	J07386-212	3459	LP 763-001	M3.0	7.85	0.32	-29.069	<2		<2	>15.3		
090	J07393+021	281	BD+02 1729	M0.0	6.77	0.65	19.944	<2		<2	>3.1		
091	J07403-174	283B	LP 783-002	M6.0	10.15	0.10	-34.329	2.78	Chu74	4.0 ± 1.5	4.0 ± 1.5	43 ± 16	-3.61
092	J07446+035	285	YZ CMi	M4.5	6.58	0.34	26.350	40.870		10.1 ± 1.5	1.3 ± 0.2	>6.6	-3.80
093	J07472+503	2M.J074713		M4.0	8.86	0.25	-40.870	1.11 ± 0.02	Irw11	12.1 ± 1.5	1.0 ± 0.1	90 ± 11	-3.76
094	J07558+833	1101	GJ 1101	M4.5	8.74	0.24	-5.204			<2	>4.1		
095	J07582+413	1105	GJ 1105	M3.5	7.73	0.26	-21.127			<2	>5.2		
096	J08119+087	299	Ross 619	M4.5	8.42	0.14	40.126			<2	>11.8		
097	J08126-215	300	GJ 300	M4.0	7.60	0.19	-13.889			<2	>11.0		
098	J08161+013	2066	GJ 2066	M2.0	6.62	0.50	62.072			<2	>5.9	0.59 ± 0.09	-4.33
099	J08293+039	2M.J082921		M2.5	7.93	0.47	23.832			<2	>9.4		
100	J08298+267	1111	DX Cnc	M6.5	8.23	0.10	10.301	0.46	New16a	10.5 ± 1.5	0.44 ± 0.05	90 ± 9	
101	J08315+730	LP 035-219		M4.0	8.78	0.22	-82.069			<2	>7.3		
102	J08358+680	3506	G 234-037	M2.5	7.86	0.40	1.261			<2	>3.6		
103	J08402+314	LSPM J0840		M3.5	8.12	0.29	92.998			<2	>6.4		
104	J08413+594	3512	LP 090-018	M5.5	9.62	0.12	6.203			<2	>12.2		
105	J08526+283	324B	rho Cnc B	M4.5	8.56	0.25	29.001			<2	>10.9		
106	J08536-034	3517	LP 666-009	M9.0	11.21	0.08	8.111	0.44	New16a	9.3 ± 2.8	0.5 ± 0.2	90 ± 9	-4.66
107	J09003+218	LP 368-128	M6.5	9.44	0.10	8.604			<2	>5.4			
108	J09005+465	1119	GJ 1119	M4.5	8.60	0.20	2.163			<2	>6.3		
109	J09028+680	3526	LP 060-179	M4.0	8.45	0.24	-44.052			<2	>12.4 ± 8.1		
110	J09033+056	NLTTR 20861		M7.0	10.77	0.12	-52.223			9.7 ± 1.5	0.8 ± 0.1		
111	J09133+688	G 234-057		M2.5	7.78	0.46	26.672			<2	>13.3		
112	J09140+196	LP 427-016		M3.0	8.42	0.40	26.209			<2	>7.7		
113	J09144+526	338B	HD 79211	M0.0	4.78	0.60	12.263			2.3 ± 1.5	10.4 ± 1.5		
114	J09161+018	RX J0916.1		M4.0	8.77	0.25	-41.586			<2	>12.2		
115	J09163-186	3543	LP 787-052	M1.5	7.35	0.56	-0.263			<2	>10.0		
116	J09307+003	1125	GJ 1125	M3.5	7.70	0.32	51.676			<2	>13.2		
117	J09360-216	357	GJ 357	M2.5	7.34	0.36	-58.758	74.30 ± 1.70	SM15	<2	>11.5		
118	J09411+132	361	Ross 85	M1.5	6.97	0.52	11.389			<2	>9.6		
119	J09423+559	363	GJ 363	M3.5	8.37	0.42	15.204	72.80 ± 7.30	Irw11	<2	>7.3		
120	J09425+700	360	GJ 360	M2.0	6.92	0.56	6.896			<2	>12.2		
121	J09428+700	362	GJ 362	M3.0	7.33	0.49	6.492			<2	>13.4		
122	J09439+269	3564	Ross 93	M3.5	8.04	0.41	55.830			<2	>13.8		
123	J09447-182	1129	GJ 1129	M4.0	8.12	0.30	26.764			<2	>15.1		
124	J09449-123	G 161-071		M5.0	8.50	0.31	16.584			31.2 ± 3.1	0.48 ± 0.05		
125	J09468+760	366	BD+76 3952	M1.5	7.44	0.57	-27.897			<2	>14.2		
126	J09511-123	369	BD-11 2741	M0.5	6.99	0.58	62.248			<2	>13.6		
127	J09561+627	373	BD+63 869	M0.0	6.03	0.64	15.323			<2	>14.2		
128	J10023+480	378	BD+48 1829	M1.0	6.95	0.60	-9.814			<2	>13.6		
129	J10122-037	382	AN Sex	M1.5	5.89	0.57	7.791	21.56	Kira12	<2	>9.0		

Table B.1. continued.

No.	ID	GJ	Name	SpT	<i>J</i>	<i>M</i>	v_{rad} (km s $^{-1}$)	P (d)	Ref.	$v \sin i$ (km s $^{-1}$)	$P_v \sin i / \sin i$ (d)	i deg	$\log L_{\text{H}\alpha} / L_{\text{bol}}$
130	J10125+570		LP 092-048	M3.5	7.76	0.32	-3.592	<2		>7.8			
131	J10167-119	386	GJ 386	M3.0	7.32	0.53	-10.700	<2		>12.6			
132	J10251-102	390	BD-09 3070	M1.0	6.89	0.57	21.430	<2		>13.4			
133	J10289+008	393	BD+01 2447	M2.0	6.18	0.48	8.238	<2		>11.4			
134	J10350-094		LP 670-017	M3.0	8.28	0.40	31.304	<2		>9.4			-3.67
135	J10360+051	398	RY Sex	M3.5	8.46	0.34	-4.634	2.9 ± 1.6		5.6 ± 3.0			
136	J10396-069	399	GJ 399	M2.5	7.66	0.54	20.182	<2		>12.8			
137	J10416+376	1134	GJ 1134	M4.5	8.49	0.21	-9.022	<2		>5.7			
138	J10482-113	3622	LP 731-058	M6.5	8.86	0.10	1.764	2.1 ± 1.5		2.8 ± 1.9			-4.63
139	J10504+331	3626	G 119-037	M4.0	8.90	0.46	-4.5834	<2		>10.7			
140	J10508+068	402	EE Leo	M4.0	7.32	0.28	-1.161	<2		>7.0			
141	J10564+070	406	CN Leo	M6.0	7.08	0.11	19.413	<2		>3.4			-3.97
142	J10584-107		LP 731-076	M5.0	9.51	0.15	-14.817	3.2 ± 1.5		2.8 ± 1.3			-3.84
143	J11000+228	408	Ross 104	M2.5	6.31	0.42	3.016	<2		>9.9			
144	J11026+219	410	DS Leo	M2.0	6.52	0.60	-14.059	15.71 ± 0.18	FH00	11.0 ± 6.4	90 ± 52		
145	J11033+359	411	Lalande 21	M1.5	4.20	0.45	-84.835	48.00	KS07	<2	$<10.6 \leq 90$		
146	J11054+435	412A	BD+44 2051	M1.0	5.54	0.43	68.760	<2		>10.1			
147	J11055+435	412B	WX UMa	M5.5	8.74	0.10	69.372	<2		0.8 ± 0.3			
148	J11110+304	414B	HD 97101 B	M2.0	6.59	0.60	-15.346	<2		>14.1			-3.65
149	J11126+189	3649	SKM 1-928	M1.5	7.45	0.56	31.543	<2		>13.3			
150	J11201-104		LP 733-099	M2.0	7.81	0.52	26.345	<2		6.7 ± 2.8			-3.96
151	J11289+101	3666	Wolf 398	M3.5	8.48	0.36	32.990	<2		>8.6			
152	J11302+076		K2-18	M2.5	9.76	0.37	0.328	<2		>8.8			
153	J11306-080		LP 672-042	M3.5	8.03	0.39	28.010	<2		>9.2			
154	J11417+427	1148	Ross 1003	M4.0	7.61	0.38	-9.139	73.50	Har11	<2	>9.0	≤ 90	
155	J11421+267	436	Ross 905	M2.5	6.90	0.48	9.482	<2		>11.4			
156	J11467-140	443	GJ 443	M3.0	7.96	0.57	6.276	<2		>13.4			
157	J11474+667		1RXS J1147	M5.0	9.68	0.15	-9.543	<2		2.7 ± 1.5	3.3 ± 1.8		-3.64
158	J11476+002	3685A	LP 613-049	M4.0	8.99	0.38	17.486	11.60	Kira12	2.4 ± 1.5	7.4 ± 4.5	90 ± 55	-3.72
159	J11476+786	445	GJ 445	M3.5	6.72	0.26	-111.804	<2		>6.6			
160	J11477+008	447	Fl Vir	M4.0	6.50	0.17	-31.195	165.10 ± 0.80	SM16	<2	>4.9	≤ 90	-4.42
161	J11509+483	1151	GJ 1151	M4.5	8.49	0.17	-35.422	132.00 ± 39.60	Irw11	<2	>4.8	≤ 90	-4.75
162	J11511+352	450	BD+36 2219	M1.5	6.42	0.51	0.295	<2		>11.9			
163	J12054+695	3704	Ross 689	M4.0	8.74	0.29	5.433	96.20 ± 9.60	Irw11	<2	>7.2	≤ 90	
164	J12100-150	3707	LP 734-032	M3.5	7.77	0.43	80.384	<2		>10.2			
165	J12111-199	3708A	LTT 4562	M3.0	7.89	0.39	2.860	<2		>9.2			
166	J12123+544 S	458A	HD 238090	M0.0	6.88	0.64	-17.279	<2		>14.9			
167	J12156+526		StKM 2-809	M4.0	8.59	0.25	-10.224	35.3 ± 3.5	0.36 ± 0.04	0.52 ± 0.05	71 ± 7		-3.63
168	J12189+111	1156	GL Vir	M5.0	8.53	0.14	6.251	0.49 ± 0.01	Irw11	15.5 ± 1.6	0.52 ± 0.05		-3.77
169	J12230+640	463	Ross 690	M3.0	7.94	0.53	8.988	<2		>12.5			
170	J12248-182	465	Ross 695	M2.0	7.73	0.27	56.650	<2		>6.8			
171	J12312+086	471	BD+09 2636	M0.5	6.78	0.61	18.972	<2		>14.4			
172	J12350+098	476	GJ 476	M2.5	8.00	0.52	33.126	<2		>12.3			

Table B.1. continued.

No.	ID	GJ	Name	SpT	J	M	v_{rad}	P	Ref.	$v \sin i$	$P_v \sin i / \sin i$	i	$\log L_{\text{H}\alpha} / L_{\text{bol}}$
				(mag)	(M $_{\odot}$)	(M $_{\odot}$)	(km s $^{-1}$)	(d)		(km s $^{-1}$)	(d)	deg	
173	J12373-208	LP 795-038	M4.0	8.97	0.26	21.231	<2	>6.6					
174	J12388+116	480	Wolf 433	M3.0	7.58	0.51	-4.350	<2	>12.1				-3.99
175	J12428+418		G 123-055	M4.0	8.12	0.29	-4.515	<2	>7.2				
176	J12479+097	486	Wolf 437	M3.5	7.20	0.35	18.970	<2	>8.4				-4.03
177	J13005+056	493.1	FN Vir	M4.5	8.55	0.17	-25.066	0.60 ± 0.02	Irw11	16.4 ± 1.6	0.59 ± 0.06	90 ± 9	-3.74
178	J13102+477		G 177-025	M5.0	9.58	0.17	-12.358	29.12	West15	<2	>4.7	≤ 90	
179	J13196+333	507.1	Ross 1007	M1.5	7.27	0.61	-11.841			<2	>14.3		
180	J13209+342	508.2	BD+35 2439	M1.0	7.40	0.58	-35.567			<2	>13.6		
181	J13229+244	3779	Ross 1020	M4.0	8.73	0.26	-19.361			<2	>6.7		
182	J13283-023W	512A	Ross 486A	M3.0	7.51	0.51	-39.606			<2	>12.1		
183	J13293+114	513	GJ 513	M3.5	8.37	0.39	28.164			<2	>9.3		
184	J13299+102	514	BD+11 2576	M0.5	5.90	0.56	14.386	28.00 ± 2.90	SM15	<2	>13.3	≤ 90	
185	J13427+332	3801	Ross 1015	M3.5	7.79	0.28	6.640			<2	>7.1		
186	J13450+176	525	BD+18 2776	M1.0	7.00	0.57	20.695			2.3 ± 1.5	11.7 ± 7.6		
187	J13457+148	526	HD 119850	M1.5	5.18	0.54	15.685	52.30 ± 1.70	SM15	<2	>12.7	≤ 90	
188	J13458-179	3804	LP 798-034	M3.5	7.75	0.33	-6.379			<2	>8.0		
189	J13536+776		RX J1353.6	M4.0	8.63	0.24	-5.959	1.23	West15	8.9 ± 1.5	1.4 ± 0.2	59 ± 10	-3.79
190	J13582+125	3817	Ross 837	M3.0	8.27	0.28	-10.012			<2	>7.0		
191	J13591-198	3820	LP 799-007	M4.0	8.33	0.26	-23.940			3.2 ± 1.5	4.1 ± 1.9		-3.92
192	J14010-026	536	HD 122303	M1.0	6.52	0.55	-25.951	43.30 ± 0.10	SM16	<2	>13.0	≤ 90	
193	J14082+805	540	BD+81 465	M1.0	7.18	0.62	7.222			<2	>14.6		
194	J14152+450	3836	Ross 992	M3.0	8.01	0.46	14.022			<2	>10.9		
195	J14173+454		RX J1417.3	M5.0	9.47	0.26	3.089			15.9 ± 1.6	0.84 ± 0.08		-3.93
196	J14251+518	549B	tet Boo B	M2.5	7.88	0.45	-10.250			<2	>10.5		
197	J14257+236E	548B	BD+24 2733	M0.5	6.89	0.65	8.341			<2	>15.3		
198	J14257+236W	548A	BD+24 2733	M0.0	6.77	0.68	9.247			<2	>15.9		
199	J14294+155	552	Ross 130	M2.0	7.23	0.56	7.710			<2	>13.1		
200	J14307-086	553	BD-07 3856	M0.5	6.62	0.74	-22.184			2.4 ± 1.5	14.4 ± 9.1		
201	J14310-122	553.1	Wolf 1478	M3.5	7.80	0.34	-1.887			<2	>8.2		
202	J14321+081		LP 560-035	M6.0	10.11	0.10	-22.116			6.3 ± 1.5	1.0 ± 0.2		-4.10
203	J14342-125	555	HN Lib	M4.0	6.84	0.30	-1.572			<2	>7.4		
204	J14524+123	3871	G 066-037	M2.0	7.97	0.52	5.596			<2	>12.2		
205	J14544+355	3873	Ross 1041	M3.5	8.24	0.47	-40.877			<2	>11.1		
206	J15013+055	3885	G 015-002	M3.0	8.33	0.40	-6.146			<2	>9.4		
207	J15095+031	3892	Ross 1047	M3.0	7.72	0.48	-32.650			<2	>11.3		
208	J15194-077	581	HO Lib	M3.0	6.71	0.33	-9.530	132.50 ± 6.30	SM15	<2	>7.9	≤ 90	
209	J15218+209	9520	OT Ser	M1.5	6.61	0.58	6.771	3.38	Nor07	4.3 ± 1.5	6.5 ± 2.3	31 ± 11	-3.76
210	J15305+094		NLT T 40406	M5.5	9.57	0.11	2.024			16.3 ± 1.6	0.42 ± 0.04		-3.95
211	J15369-141	592	Ross 802	M4.0	8.43	0.32	2.287			<2	>7.7		
212	J15499+796		LP 022-420	M5.0	9.72	0.14	-15.672			26.9 ± 2.7	0.31 ± 0.03		-3.82
213	J15598-082	606	BD-07 4156	M1.0	7.18	0.56	-17.279			<2	>13.2		
214	J16028+205	609	GJ 609	M4.0	8.13	0.25	6.362			<2	>6.4		
215	J16092+093		G 137-084	M3.0	7.97	0.39	-4.5015			<2	>9.2		

Table B.1. continued.

No.	ID	GJ	Name	SpT	<i>J</i>	<i>M</i>	v_{rad} (km s $^{-1}$)	<i>P</i> (d)	Ref.	$v \sin i$ (km s $^{-1}$)	$P_v \sin i / \sin i$ (d)	<i>i</i> deg	$\log L_{\text{H}\alpha} / L_{\text{bol}}$
216	J16102-193	K2-33		M3.0	11.10	0.32	-6.086			7.3 ± 1.5	2.1 ± 0.4		-3.99
217	J16167+672N	617B	EW Dra	M3.0	6.91	0.51	-18.646			< 2	> 12.0		
218	J16167+672S	617A	HD 147379	M0.0	5.78	0.70	-19.036			2.7 ± 1.5	11.9 ± 6.5		
219	J16254+543	625	GJ 625	M1.5	6.61	0.35	-13.203			< 2	> 8.3		
220	J16303-126	628	V2306 Oph	M3.5	5.95	0.32	-21.360	119.30 ± 0.50	SM16	< 2	> 7.8	≤ 90	
221	J16313+408	3959	G 180-060	M5.0	9.46	0.16	-22.858	0.51	Hari1	7.1 ± 1.5	1.3 ± 0.3	22 ± 4	-3.66
222	J16327+126	1203	GJ 1203	M3.0	8.43	0.39	-32.963			< 2	> 9.2		
223	J16462+164	3972	LP 446-006	M2.5	7.95	0.48	18.730			< 2	> 11.4		
224	J16554-083N	643	GJ 643	M3.5	7.55	0.20	15.699			< 2	> 5.4		
225	J16555-083	644C	vB 8	M7.0	9.78	0.09	14.392			5.4 ± 1.5	1.0 ± 0.3		-4.40
226	J16570-043	1207	LP 686-027	M3.5	7.97	0.27	-3.886	1.21	Kira12	10.1 ± 1.5	1.4 ± 0.2	63 ± 9	-3.70
227	J16581+257	649	BD+25 3173	M1.0	6.45	0.57	4.178			< 2	> 13.5		
228	J17033+514	3988	G 203-042	M4.5	8.77	0.17	37.396			< 2	> 4.9		
229	J17052-050	654	Wolf 636	M1.5	6.78	0.53	34.682			< 2	> 12.4		
230	J17071+215	655	Ross 863	M3.0	7.88	0.42	-50.945			< 2	> 9.8		
231	J17115+384	3992	Wolf 654	M3.5	7.63	0.42	-44.582			< 2	> 9.8		
232	J17166+080	2128	GJ 2128	M2.0	7.93	0.45	-30.739			< 2	> 10.5		
233	J17198+417	671	GJ 671	M2.5	7.71	0.41	-19.661			< 2	> 9.6		
234	J17303+055	678.1 A	BD+05 3409	M0.0	6.24	0.59	-12.637			< 2	> 13.9		
235	J17338+169	1RXS J1733	M5.5	8.89	0.21	-22.484	0.27	No07	41.5 ± 7.7	0.27 ± 0.05	80 ± 14	-3.50	
236	J17355+616	685	BD+61 1678	M0.5	6.88	0.61	-15.057	19.20	Ba83	< 2	> 14.3	≤ 90	
237	J17378+185	686	BD+18 3421	M1.0	6.36	0.49	-9.675			< 2	> 11.5		
238	J17542+073	1222	GJ 1222	M4.0	8.77	0.29	-28.415			< 2	> 7.2		
239	J17578+046	699	Barnards S	M3.5	5.24	0.15	-110.579	130.00	KS07	< 2	> 4.5	≤ 90	
240	J17578+465	4040	G 204-039	M2.5	7.85	0.45	-31.499	31.64	Hari1	< 2	> 10.5	≤ 90	
241	J18022+642	LP 071-082	M5.0	8.54	0.17	-1.429	0.28	New1a	11.3 ± 1.5	0.9 ± 0.1	18 ± 2	-3.82	
242	J18027+375	1223	GJ 1223	M5.0	9.72	0.14	3.715	123.80	New1a	< 2	> 4.1	≤ 90	
243	J18051-030	701	HD 165222	M1.0	6.16	0.52	32.524	127.80 ± 3.20	SM15	< 2	> 12.3	≤ 90	
244	J18075-159	1224	GJ 1224	M4.5	8.64	0.15	-33.005			2.2 ± 1.5	4.0 ± 2.8	-3.89	
245	J18131+260	4044	LP 390-016	M4.0	8.90	0.34	-8.516	2.28	Hari1	5.9 ± 1.5	2.7 ± 0.7	56 ± 14	-3.61
246	J18165+048	G 140-051	M5.0	9.80	0.15	-53.460			< 2	> 4.4			
247	J18174+483	TYC 3529-1	M2.0	7.77	0.51	-24.051			< 2	> 12.0	-4.03		
248	J18180+387E	4048A	G 204-058	M3.0	8.04	0.29	0.363			< 2	> 7.3	-4.07	
249	J18189+661	4053	LP 071-165	M4.5	8.74	0.13	5.580			15.3 ± 1.5	0.50 ± 0.05		
250	J18221+063	7112	Ross 136	M4.0	8.67	0.26	-43.805			< 2	> 6.6		
251	J18224+620	1227	GJ 1227	M4.0	8.64	0.16	-13.774			< 2	> 4.6		
252	J18319+406	4062	G 205-028	M3.5	8.06	0.33	-19.128			< 2	> 7.8		
253	J18346+401	4063	LP 229-017	M3.5	7.18	0.19	12.390			< 2	> 5.3		
254	J18353+457	720A	BD+45 2743	M0.5	6.88	0.63	-31.678			< 2	> 14.9		
255	J18356+329	LSR J1835+	M8.5	10.27	0.07	3.188			49.2 ± 4.9	0.09 ± 0.01	-5.05		
256	J18363+136	4065	Ross 149	M4.0	8.19	0.27	-4.5146			< 2	> 6.7	-4.41	
257	J18409-133	724	BD-13 5069	M1.0	7.40	0.58	-33.124			< 2	> 13.8		
258	J18419+318	4070	Ross 145	M3.0	7.52	0.41	-31.900			< 2	> 9.7		

Table B.1. continued.

No.	ID	GJ	Name	SpT	<i>J</i>	<i>M</i>	v_{rad} (km s $^{-1}$)	<i>P</i> (d)	Ref.	$v \sin i$ (km s $^{-1}$)	$P_v \sin i / \sin i$ (d)	i deg	$\log L_{\text{H}\alpha} / L_{\text{bol}}$
259	J18480-145	4077	G 155-042	M2.5	8.38	0.45	-4.651	<2	New16a	2.4 ± 1.5	> 10.6	-3.99	
260	J18482+076	G 141-036	M5.0	8.85	0.13	-34.413	2.76	KS07	3.0 ± 1.5	3.2 ± 2.0	58 ± 36	-3.99	
261	J18498-238	729	V1216Sgr	M3.5	6.22	0.28	-10.631	2.87		4.7 ± 2.3	37 ± 18	-3.99	
262	J18580+059	740	BD+05 3993	M0.5	6.24	0.62	10.245	<2		> 14.6			
263	J19070+208	745A	Ross 730	M2.0	7.29	0.33	32.247	<2		<2	> 7.9		
264	J19072+208	745B	HD 349726	M2.0	7.28	0.33	31.969	<2		<2	> 8.0		
265	J19084+322	4098	G 207-019	M3.0	7.91	0.39	-1.851	<2		<2	> 9.2		
266	J19098+176	1232	GJ 1232	M4.5	8.82	0.19	-14.094	<2		<2	> 5.3		
267	J19169+051N	752A	V1428 Aql	M2.5	5.58	0.53	35.678	46.00 ± 0.20	SM16	<2	> 12.4	≤ 90	-4.49
268	J19169+051S	752B	V1298 Aql	M8.0	9.91	0.08	35.698			2.7 ± 2.2	1.9 ± 1.6		
269	J19216+208	1235	GJ 1235	M4.5	8.80	0.19	4.683	<2		<2	> 5.2		
270	J19251+283	4109	Ross 164	M3.0	8.44	0.40	-40.638	<2		<2	> 9.4		
271	J19255+096	LSPM J1925	M8.0	11.21	0.11	-23.323	34.7 ± 3.5		0.19 ± 0.02			-4.96	
272	J19346+045	763	BD+04 4157	M0.0	6.71	0.63	-58.414	3.9 ± 1.5		7.6 ± 2.9			
273	J19422-207	2M J194212	M5.1	9.60	0.20	-2.061	6.2 ± 1.5		1.8 ± 0.4			-3.75	
274	J19511+464	1243	G 208-042	M4.0	8.59	0.25	-13.445	<2		22.5 ± 2.3	0.56 ± 0.06	90 ± 9	
275	J20093-012	2M J200918	M5.0	9.40	0.14	-53.963	4.3 ± 1.5		2.0 ± 0.7			-3.73	
276	J20260+585	1253	Wolf 1069	M5.0	9.03	0.15	-59.992	<2		<2	> 4.5		-3.80
277	J20305+654	793	GJ 793	M2.5	6.74	0.41	10.457	<2		<2	> 9.8		-4.61
278	J20336+617	1254	GJ 1254	M4.0	8.29	0.42	-21.003	<2		<2	> 9.9		
279	J20405+154	1256	GJ 1256	M4.5	8.64	0.19	-59.595	104.60	New16a	<2	> 5.2	≤ 90	-4.73
280	J20450+444	806	BD+44 3567	M1.5	7.33	0.48	-24.846	<2		<2	> 11.3		
281	J20525-169	LP 816-060	M4.0	7.09	0.24	16.164	67.60 ± 0.10	SM16	<2	> 6.3	≤ 90		
282	J20533+621	809A	BD+61 2068	M0.5	5.43	0.60	-17.320	<2		<2	> 14.1		
283	J20567-104	811.1	Wolf 896	M2.5	7.77	0.50	35.096	<2		<2	> 11.8		
284	J21019-063	816	Wolf 906	M2.5	7.56	0.51	-15.098	<2		<2	> 12.1		
285	J21152+257	4184	LP 397-041	M3.0	8.40	0.40	-16.162	<2		<2	> 11.6		
286	J21164+025	LSPM J2116	M3.0	8.22	0.40	-22.177	<2		<2	> 9.5			
287	J21221+229	GSC 02187-	M1.0	7.40	0.59	5.503	<2		<2	> 13.9			
288	J21348+515	4205	Wolf 926	M3.0	8.04	0.49	-13.992	<2		<2	> 11.6		
289	J21463+382	LSPM J2146	M4.0	7.95	0.17	-82.846	<2		<2	> 4.8			
290	J21466+668	G 264-012	M4.0	8.84	0.26	-9.606	<2		<2	> 6.6			
291	J21466-001	1263A	Wolf 940	M4.0	8.36	0.29	-28.369	<2		<2	> 14.1		
292	J22012+283	4247	V374 Peg	M4.0	7.63	0.30	-4.339	0.45	Kor10	35.4 ± 3.5	0.42 ± 0.04	90 ± 9	-3.56
293	J22020-194	843	LP 819-017	M3.5	8.05	0.36	-23.401	<2		<2	> 8.6		
294	J22021+014	846	BD+00 4810	M0.5	6.20	0.60	18.189	<2		<2	> 14.1		
295	J22057+656	4258	G 264-018	M1.5	8.42	0.31	-46.708	<2		<2	> 7.6		
296	J22096-046	849	BD-05 5715	M3.5	6.51	0.53	-15.315	39.20 ± 6.30	SM15	<2	> 12.5	≤ 90	
297	J22114+409	IRXS J2211	M5.5	9.72	0.12	-16.836	<2		<2	> 3.7			
298	J22115+184	851	Ross 271	M2.0	6.72	0.58	-51.510	<2		<2	> 13.7		-3.88
299	J22125+085	9773	Wolf 1014	M3.0	8.28	0.38	8.584	<2		<2	> 9.0		
300	J22137-176	1265	LP 819-052	M4.5	8.96	0.17	-24.297	<2		<2	> 4.9		
301	J22231-176	4274	LP 820-012	M4.5	8.24	0.17	-1.789	<2		<2	> 4.9		-3.88

Table B.1. continued.

No.	ID	GJ	Name	SpT	<i>J</i>	<i>M</i>	v_{rad} (km s $^{-1}$)	P (d)	Ref.	$v \sin i$ (km s $^{-1}$)	$P_v \sin i / \sin i$ (d)	i deg	$\log L_{\text{H}\alpha} / L_{\text{bol}}$
302	J22252+594	4276	G 232-070	M4.0	8.74	0.39	4.034	<2	>9.1				
303	J22298+414	1270	G 215-050	M4.0	8.85	0.25	2.291	<2	>6.5				
304	J22330+093	863	BD+08 4887	M1.0	7.21	0.53	-6.640	<2	>12.4				
305	J22468+443	873	EV Lac	M3.5	6.11	0.35	0.192	4.38	Tes04	3.5 ± 1.5	4.8 ± 2.0	66 ± 28	-3.62
306	J22503-070	875	BD-07 5871	M0.5	6.93	0.60	-5.769	<2	>14.1				
307	J22518+317	875.1	GT Peg	M3.0	7.70	0.48	-2.202	1.64	Nor07	13.4 ± 1.5	1.7 ± 0.2	75 ± 8	-3.56
308	J22532-142	876	IL Aqr	M4.0	5.93	0.37	-1.683	87.30 ± 5.70	SM15	<2	>8.8	≤ 90	
309	J22559+178	4306	StKM 1-206	M1.0	7.32	0.60	-32.059	<2	>14.1				
310	J22565+165	880	HD 216899	M1.5	5.36	0.60	-27.490	37.50 ± 0.10	SM15	<2	>14.2	≤ 90	
311	J23064-050		2MUCD 1217	M8.0	11.35	0.09	-53.362	<2	>2.7				
312	J23113+085		NLT T 56083	M3.5	8.47	0.33	-10.873	<2	>7.9				
313	J23216+172	4333	LP 462-027	M4.0	7.39	0.44	-6.591	<2	>10.3				
314	J23245+578	895	BD+57 2735	M1.0	6.79	0.61	-33.336	<2	>14.3				
315	J23340+001	899	GJ 899	M2.5	7.66	0.48	-4.704	<2	>11.2				
316	J23351-023	1286	GJ 1286	M5.5	9.15	0.12	-41.013	<2	>3.6				
317	J23381-162	4352	G 273-093	M2.0	7.81	0.51	20.657	<2	>12.0				
318	J23419+441	905	HH And	M5.0	6.88	0.14	-78.032	<2	>4.2				
319	J23431+365	1289	GJ 1289	M4.0	8.11	0.21	-2.797	<2	>5.6				
320	J23492+024	908	BR Psc	M1.0	5.83	0.47	-71.296	<2	>10.9				
321	J23505-095	4367	LP 763-012	M4.0	8.94	0.30	-21.685	<2	>7.4				
322	J23548+385		RX J2354.8	M4.0	8.94	0.29	5.522	4.76	KS13	3.6 ± 1.5	4.0 ± 1.7	90 ± 37	-3.67
323	J23556-061	912	GJ 912	M2.5	7.60	0.60	17.444	<2	>14.1				
324	J23585+076	4383	Wolf 1051	M3.0	7.91	0.51	-13.070	<2	>11.9				

Period References: Irw11: Irwin et al. (2011); New16a: Newton et al. (2016); SM16a: Suárez Mascareño et al. (2016); Kir12: Kiraga (2012); KS07: Kiraga & Stepien (2007); HM15: Houdebine & Mullan (2015); Chu74: Chugainov (1974); FH00: Fekel & Henry (2000); Har11: Hartman et al. (2011); WF11: Wang & Ford (2011); West15: West et al. (2015); SM15: Suárez Mascareño et al. (2015); Nor07: Norton et al. (2007); Nor04: Norton et al. (2004); Tes04: Testa et al. (2004); Tes04: Testa et al. (2010); Kor10: Korhonen et al. (1983); Ba83: Baliunas et al. (1983); Kiraga & Stepien (2013)